Crystalline silicon surface passivation using aluminum oxide: Fundamental understanding and application to solar cells

Von der Fakultät für Mathematik und Physik
der Gottfried Wilhelm Leibniz Universität Hannover

zur Erlangung des Grades
Doktor der Naturwissenschaften
Dr. rer. nat.

genehmigte Dissertation

von

Dipl.-Phys. Boris Adrian Veith-Wolf
geboren am 08.12.1983 in Hannover

Erscheinungsjahr 2018

Referent:	Prof. Dr J. Schmidt
Korreferent:	Prof. Dr. C. Tegenkamp
Tag der Promotion:	09.02.2018

Kurzzusammenfassung

In der vorliegenden Arbeit wurden verschiedene Aspekte der Siliziumoberflächenpassivierung mittels Aluminiumoxid (Al_2O_3) untersucht; vom grundlegenden Verständnis der Oberflächenpassivierung insbesondere auf n-Typ Siliziumwafern bis hin zur Implementierung in "Passivated Emitter and Rear Cell" (PERC)-Solarzellen.

Für die Abscheidung von Al_2O_3 wurden drei verschiedene Abscheidetechniken untersucht: (i) die plasmaunterstützte Atomlagenabscheidung (PA-ALD), (ii) die räumliche Atomlagenabscheidung (S-ALD) und (iii) erstmals die induktiv gekoppelte plasmaunterstützte chemische Gasphasenabscheidung (ICP-PECVD). Es konnte unabhängig von der verwendeten Abscheidetechnik gezeigt werden, dass alle Al_2O_3-Schichten eine exzellente Oberflächenpassivierung, sowohl nach Niedertemperaturtempern als auch nach einem schnellen Hochtemperaturfeuerschritt, liefern können.

Für PA-ALD-Al_2O_3-passivierte n-Typ Siliziumwafer konnte gezeigt werden, dass die Abnahme der Oberflächenpassivierung hin zu niedrigeren Injektionsdichten verursacht wird durch die Leitung von Löchern durch die Inversionsschicht und von Elektronen durch die Basis vom Messbereich hin zu Bereichen hoher Rekombination. Durch das Vermeiden von Bereichen mit reduzierter Oberflächenpassivierung und der Verwendung von großen Proben (12.5×12.5 cm^2) konnte erstmals gezeigt werden, dass die Volumenlebensdauer des untersuchten 1.2-1.4 Ωcm n-Typ kristallinem Siliziums (c-Si) signifikant höher ist als die bisherige Parametrisierung der intrinsischen Lebensdauer von c-Si es voraussagt. In dieser Arbeit konnte daher erstmals gezeigt werden, dass die intrinsische Lebensdauer in c-Si deutlich über der bislang vermuteten liegt. Dieses hat unmittelbare Auswirkungen auf den maximal erreichbaren Wirkungsgrad einer c-Si Solarzelle.

Alternative Al_2O_3-Deckschichten auf der Basis von flüssigen Siloxanlösungen, abgeschieden mittels Flüssigphasenabscheidung (LPD), wurden in PERC-Solarzellen implementiert. Es konnte gezeigt werden, dass Al_2O_3/LPD-Stapel nur dann eine gute Oberflächenpassivierung nach dem Feuern ermöglichen, wenn während des Feuerns keine Metallpaste vorhanden ist. Dünne LPD-Schichten ($<$ 130 nm) bildeten keine wirksamen Barrieren gegen die Al-Paste, ein Stapel aus PA-ALD-Al_2O_3-, LPD-SiO_x- und LPD-SiO_xTiO_y-Schichten sorgte jedoch auch nach dem Bedrucken und Feuern mit Al-Paste für eine gute Oberflächenpassivierung. Dies wurde zusätzlich an großflächigen (15.6×15.6 cm^2) PERC-Solarzellen mit Wirkungsgraden von bis zu 19.8% nachgewiesen.

Die gefeuerten S-ALD-Al_2O_3-Schichten erwiesen sich unter UV-Beleuchtung als sehr stabil, egal ob als Einzelschicht oder Al_2O_3/SiN_x-Stapel. Besonders der Al_2O_3/ SiN_x-Stapel zeigte eine stabile p^+-Emitterpassivierung mit einer Sättigungsstromdichte $J_{0\mathrm{E}}$ von nur 18 fA/cm^2. Bei gefeuerten Al_2O_3-Einzelschichten wurde eine starke Erhöhung der festen negativen Ladungsdichte Q_f bis zu einem Wert von $-(11.8\pm1)\times10^{12}$ cm^2 beobachtet.

Schlagwörter: Silizium; Aluminiumoxid; Oberflächenpassivierung

Abstract

In the present thesis, different aspects of the silicon surface passivation provided by aluminum oxide (Al_2O_3) were investigated; from the fundamental understanding of the surface passivation especially on *n*-type silicon wafers to the implementation into "Passivated Emitter and Rear Cell" (PERC) solar cells.

For the deposition of Al_2O_3, three different deposition techniques were evaluated: (i) plasma-assisted atomic layer deposition (PA-ALD), (ii) spatial atomic layer deposition (S-ALD) and, (iii) for the first time inductively coupled plasma-enhanced chemical vapor deposition (ICP-PECVD). It was shown that, regardless of the deposition technique used, all Al_2O_3 layers can provide an excellent level of surface passivation after low-temperature-annealing as well as after high-temperature fast-firing.

For *n*-type silicon wafers passivated using PA-ALD Al_2O_3 it was shown that the decrease of the surface passivation quality towards lower injection densities is caused by the conductance of the holes through the inversion layer and simultaneously of the electrons through the base, from the measurement area to areas of high recombination. By avoiding areas of reduced surface passivation quality on the sample and using large-area wafers (12.5×12.5 cm^2), it was shown for the first time that the bulk lifetime of the examined 1.2-1.4 Ωcm *n*-type crystalline silicon (c-Si) is significantly higher than predicted by the state-of-the-art parameterization of the intrinsic lifetime of c-Si. Hence, in this work, it was shown for the first time that the intrinsic lifetime in c-Si is significantly higher than previously assumed. This has an immediate effect on the maximal achievable efficiency of a c-Si solar cell.

Alternative Al_2O_3 capping layers based on liquid siloxane solutions deposited by liquid phase deposition (LPD) were implemented into PERC solar cells. It was shown that Al_2O_3/LPD stacks provide a good surface passivation after firing only if no metal paste is present during the firing. Thin LPD layers ($<$ 130 nm) were no effective barriers against the Al paste, however, a stack consisting of PA-ALD Al_2O_3, LPD-SiO_x and LPD-SiO_xTiO_y layers provided a good surface passivation even after Al-paste printing and firing. This was additionally demonstrated on large-area (15.6×15.6 cm^2) PERC solar cells with efficiencies up to 19.8%.

Fired S-ALD Al_2O_3 layers were shown to be very stable under UV illumination, regardless if used as single layer or in Al_2O_3/SiN_x stacks. Especially the Al_2O_3/SiN_x stack showed a stable p^+-emitter passivation with a saturation current density J_{0E} as low as 18 fA/cm^2. For fired single Al_2O_3 layers, a strong increase of the negative fixed charge density Q_f, up to a value of $-(11.8\pm1)\times10^{12}$ cm^{-2}, was observed.

Keywords: silicon; aluminum oxide; surface passivation

Contents

Chapter 1

Introduction

The generation of electricity with photovoltaic (PV) modules has become one of the key technologies for the future of power generation. In the past, the increased share of PV over the total power generation was largely achieved by government programs or special laws pushing the installation of PV modules. One important governmental assistance are special feed-in tariffs, as first introduced in Germany called "Erneuerbare-Energien-Gesetz" (EEG) and later also in other countries, such as Italy, Japan and Israel. Still a lot of electricity is generated through conventional power sources, e.g., coal, nuclear, or gas power plants. In order to further increase the amount of electricity generated by PV, the cost has to be decreased and reliability has to be increased further. One road to bring down the costs is to increase the efficiency of the PV modules. This can be achieved by new solar cell concepts, high-purity silicon materials and/or advanced production processes. One important new solar cell concept for the industrial production has become the so-called "Passivated Emitter and Rear Cell" (PERC). This solar cell concept was first introduced in 1989 by Blakers et al. [1]. For the implementation into production, however, the development of several new materials was necessary, one being aluminum oxide (Al_2O_3) for the rear surface passivation of the solar cell. The idea to use Al_2O_3 as material for the surface passivation of silicon was already introduced by Hezel and Jäger in 1989 [2]. At the same time, Hezel and Jäger were also working on silicon nitride (SiN_x) as surface passivation scheme. The SiN_x provided a better surface passivation and, in addition, excellent anti-reflection properties [2], therefore, further research was focused on SiN_x. Al_2O_3 was not investigated until in 2006 when Agostinelli et al. [3] and Hoex et al. [4] demonstrated the excellent silicon surface passivation with Al_2O_3 deposited using atomic layer deposition (ALD). In 2008, Schmidt et al. [5] published the first solar cells results exceeding 20% and Al_2O_3 is since then in the focus of PV research.

It was shown that the surface passivation of Al_2O_3 provides the best dielectric passivation of silicon surfaces so far. Thus, allowing a new and more precise determination of the bulk lifetime of the silicon material. Just at the beginning of the present PhD work, Richter et al. [6] published an improved intrinsic lifetime limit for crystalline silicon. However, the surface passivation of Al_2O_3 was considered to be mainly advantageous for p-type silicon, since on n-type silicon the surface passivation seemed to be reduced under low illumination intensities [7]. During the coursework of this thesis, another explanation was developed [8] for the reduced lifetimes measured on n-type silicon wafers passivated with Al_2O_3. The recombination at the edges is coupled to the measurement area via the inversion layer, induced by the negative fixed charge density within the Al_2O_3 layer. This approach is investigated in detail in Chapter 5. The results are used to diminish the influence of this effect and, therefore, approaching the true intrinsic lifetime of n-type silicon closer than in any previous study.

Due to the remarkable surface passivation of p-type silicon, Al_2O_3 is excellently suited as rear surface passivation layer for the application in industrial PERC solar cells. Until this was possible, however, some obstacles had to be overcome. One concerns the deposition technique used. The ALD process applied in the initial state is very slow and not competitive concerning throughput in the modern PV industry. Therefore, the search for alternative deposition methods was one of the major challenges during the time of the beginning of this thesis. At that time, the first results using a fast ALD process, called spatial ALD (S-ALD) [9, 10], using plasma-enhanced chemical vapor deposition (PECVD) [11], and atmospheric pressure chemical vapor deposition (APCVD) [12] had been published. In this thesis, the spatial ALD is subject of further investigations and the inductively coupled plasma (ICP)-PECVD deposition method is investigated for the first time in Chapter 4. In this thesis, the deposition methods are mostly investigated based on lifetime samples, however, in Chapter 6 the implementation of ICP-PECVD-deposited Al_2O_3 into PERC solar cells is examined as well.

Besides the slow deposition by the ALD process, another drawback of the Al_2O_3 surface passivation is the need of another dielectric layer as capping layer on top of the Al_2O_3 to protect the Al_2O_3 in the cell process. As such a capping layer the well-established SiN_x is routinely used today, however, this is deposited by PECVD and therefore an additional cost factor. In Chapter 6, new capping layers, all based on liquid siloxane solutions deposited by liquid phase deposition (LPD), are evaluated.

The best-suited LPD capping layers are implemented into PERC solar cells for the first time.

As not only the production costs are important, but also the reliability, another focus in this thesis is the long-term stability of the surface passivation quality under illumination, especially UV illumination. This is investigated in Chapter 7 for the case of S-ALD Al_2O_3.

Chapter 2

Recombination in crystalline silicon

In this Chapter, we will briefly describe the main recombination mechanisms in crystalline silicon (c-Si). First, an overview of the recombination processes in the c-Si bulk will be given, followed by a discussion of the recombination at the c-Si surface.

All recombination processes are described by a net recombination rate U_i that is defined as the number of recombining electron-hole pairs per second and volume subtracted by the thermal generation rate. This net recombination rate is a monotonically increasing function of the excess carrier concentration $\Delta n = \Delta p$, therefore, it is convenient to define an excess carrier lifetime τ_i for each individual recombination process:

$$\frac{1}{\tau_i(\Delta n)} = \frac{U_i(\Delta n)}{\Delta n}. \tag{2.1}$$

All recombination processes are independent of each other and the total recombination rate is the sum of all individual recombination rates. This allows the definition of a total excess carrier lifetime τ_{tot}:

$$\frac{1}{\tau_{\mathrm{tot}}} = \sum_i \frac{1}{\tau_i}. \tag{2.2}$$

2.1 Recombination in the c-Si bulk

The recombination in the c-Si bulk can be separated into intrinsic and extrinsic recombination processes. Extrinsic recombination is induced by defects such as impurities, whereas the unavoidable intrinsic recombination can be subdivided into radiative and Auger recombination.

2.1.1 Radiative recombination

Radiative recombination is the inverse process to the photon absorption. The radiative lifetime τ_{rad} is calculated using [13]

$$\tau_{\mathrm{rad}} = \frac{\Delta n}{(np - n_{\mathrm{i,eff}}^2) B_{\mathrm{rel}} B_{\mathrm{low}}}, \tag{2.3}$$

with n being the electron concentration, p the hole concentration, $n_{\mathrm{i,eff}}$ the effective intrinsic carrier concentration [14], $B_{\mathrm{low}} = 4.73\times10^{-15}$ cm^3/s at 300 K the coefficient of the radiative recombination as measured by Trupke et al. [15] and B_{rel} the relative radiative recombination coefficient. B_{rel} is dependent on the doping concentration, the injection level, and the intrinsic carrier concentration n_{i}, 9.7×10^9 cm^{-3} at 300 K [16]. The parameterization for B_{rel} used in this work stems from Altermatt et al. [13]. The effective intrinsic carrier concentration $n_{\mathrm{i,eff}}$ is calculated using [14]

$$n_{\mathrm{i,eff}} = n_{\mathrm{i}} \exp\left(\frac{\Delta E_{\mathrm{g}}}{2kT}\right), \tag{2.4}$$

with k being the Boltzmann constant, T the temperature, and ΔE_{g} the energy band-gap narrowing calculated using the random-phase approximation model by Schenk [17].

2.1.2 Auger recombination

The Auger recombination is a non-radiative recombination process where three charge carriers are involved, an electron-hole pair and a hole or electron, respectively. The electron-hole pair recombines and the energy set free is transfered to the third particle. The third particle relaxes this energy thermally. The general description of the Auger lifetime τ_{Aug} is

$$\tau_{\mathrm{Aug}} = \frac{\Delta n}{C_n(n^2 p - n_{\mathrm{i}}^2 n_0) + C_p(np^2 - n_{\mathrm{i}}^2 p_0)}, \tag{2.5}$$

with n_0 being the thermal equilibrium electron concentration, p_0 the thermal equilibrium hole concentration, and C_n and C_p the Auger recombination coefficients for the electron-electron-hole (eeh) and for the electron-hole-hole (ehh) process, respectively. In highly doped silicon ($N_{\mathrm{A,D}} \gg n_{\mathrm{i}}$) are $C_n = 2.8\times10^{-31}$ cm^{6}s^{-1} and $C_p = 9.9\times10^{-32}$ cm^{6}s^{-1} [18]. For lowly doped and/or highly injected ($\Delta n > N_{\mathrm{A,D}}$) silicon Eq. (2.5) is not valid any more. For highly injected silicon the Auger recombination lifetime should be $\sim 1/(C_n + C_p)\Delta n^2$, however, the coefficient $C_n + C_p \equiv C_a$, called the ambipolar Auger coefficient, is measured to be about three times larger than the sum of C_n and C_p, i.e., $C_a = 1.66\times10^{-30}$ cm^{6}s^{-1} as measured by Sinton and Swanson [19]. This leads to an increased Auger recombination rate under high injection. For lowly doped silicon the Auger recombination is also enhanced, the reason is that excitons formed by Coulomb interaction increase the probability of the Auger recombination. This Coulomb interaction can be described by applying quantum-mechanical theory to lowly doped silicon [20]. However, the Coulomb interaction is not the only enhancement of the Auger recombination, other involve phonon interaction [21, 22] or impurities [23]. These considerations lead to a more general description of the Auger recombination [24]

$$\tau_{\text{Aug}} = \frac{\Delta n}{(np - n_{\text{i}}^2)(g_{eeh} C_n n_0 + g_{ehh} C_p p_0 + g_{\Delta n} C_a \Delta n)}, \tag{2.6}$$

with g_{eeh}, g_{ehh}, and $g_{\Delta n}$ being the so-called Auger enhancement factors. These enhancement factors have to be determined experimentally. Therefore, and because the Auger recombination cannot be measured directly without measuring all the other recombination processes in the silicon bulk, the Auger recombination is up to now a topic of scientific discussion. The most widely used parameterization was published by Kerr et al. [24]. However, with the later improvements in the surface passivation quality, especially the introduction of the excellent Al_2O_3 passivation, a new parameterization was developed by Richter et al. [6]. This parameterization is based on lifetime measurement on n- and p-type silicon samples passivated with Al_2O_3. This parameterization is nowadays the most widespread used Auger parameterization ($\tau_{\text{Aug.Richter}}$ in seconds and concentrations in cm^{-3}):

$$\tau_{\text{Aug.Richter}} = \frac{\Delta n}{(np - n_{\text{i,eff}}^2)(2.5\times10^{-31} g_{\text{eeh}} n_0 + 8.5\times10^{-32} g_{\text{ehh}} p_0 + 3\times10^{-29} \Delta n^{0.92})}, \tag{2.7}$$

where g_{eeh} and g_{ehh} are the enhancement factors which can be described by the following set of equations (concentrations in cm^{-3}) [6]:

$$g_{\text{eeh}} = 1 + 13 \left\{ 1 - \tanh\left[\left(\frac{n_0}{3.3\times10^{17}} \right)^{0.66} \right] \right\}, \tag{2.8}$$

$$g_{\text{ehh}} = 1 + 7.5 \left\{ 1 - \tanh\left[\left(\frac{p_0}{7\times10^{17}} \right)^{0.63} \right] \right\}. \tag{2.9}$$

The radiative lifetime τ_{rad} and the Auger lifetime $\tau_{\text{Aug.Richter}}$ combined gives us the intrinsic lifetime according to Richter et al. [6] ($\tau_{\text{intr.Richter}}$ in seconds and concentrations in cm^{-3}):

$$\tau_{\text{intr.Richter}} = \frac{\Delta n}{(np - n_{\text{i,eff}}^2)(2.5\times10^{-31} g_{\text{eeh}} n_0 + 8.5\times10^{-32} g_{\text{ehh}} p_0 + 3\times10^{-29} \Delta n^{0.92} + B_{\text{rel}} B_{\text{low}})}. \tag{2.10}$$

2.1.3 Recombination through defects

The extrinsic recombination process through defects was first described in 1952 by Shockley, Read, and Hall [25, 26]. Therefore, this process is often called the Shockley-Read-Hall (SRH) recombination. In this recombination process, an electron-hole pair recombines trough a defect with an energy level E_{t} within the forbidden bandgap of the semiconductor. In the case of monocrystalline silicon, as examined in this work, the defects are frequently impurity atoms in the bulk and at the surface, as well as dangling bonds. For a single defect the recombination rate is described by [25, 26]

$$U_{\text{SRH}} = \frac{(np - n_{\text{i}}^2) v_{\text{th}} N_{\text{t}}}{\sigma_p^{-1}(n + n_1) + \sigma_n^{-1}(p + p_1)}, \tag{2.11}$$

where σ_n and σ_p are the capture cross sections for electrons and holes, respectively, N_{t} is the defect density, v_{th} is the thermal velocity, and n_1 and p_1 are the so-called "SRH densities" defined as

$$n_1 = N_{\text{c}} e^{\left(\frac{E_{\text{t}} - E_{\text{c}}}{kT}\right)}, \quad p_1 = N_{\text{v}} e^{\left(\frac{E_{\text{v}} - E_{\text{t}}}{kT}\right)}. \tag{2.12}$$

N_{c} and N_{v} are the effective density of states in the conduction and valence bands, respectively.

2.2 Recombination at the c-Si surface

Inside the silicon bulk the atoms are periodically arranged in a diamond cubic crystal structure. This periodicity is abruptly terminated at the silicon surface. Depending on the orientation of the surface, the surface atoms lack one [(111)-orientated surfaces] or two binding partners [(100)-orientated surfaces]. In this work, only samples with a (100)-orientated surface are examined. The unsaturated "open" bonds are also called "dangling bonds" and lead to energy states in the bandgap. This energy states are not located at one single energy level E_{t} but are quasi-continuously distributed over the entire bandgap. In order to describe this type of defect, the energy-dependent interface state density $D_{\mathrm{it}}(E)$ is used. The surface recombination rate due to the interface states U_{it} is than given by the equation [27]:

$$U_{\mathrm{it}} = (n_{\mathrm{s}}p_{\mathrm{s}} - n_{\mathrm{i}}^2) \int\limits_{E_{\mathrm{v}}}^{E_{\mathrm{c}}} \frac{\upsilon_{\mathrm{th}} D_{\mathrm{it}}(E) dE}{\sigma_p^{-1}(E)(n_{\mathrm{s}} + n_1(E)) + \sigma_n^{-1}(E)(p_{\mathrm{s}} + p_1(E))}, \tag{2.13}$$

$$n_{\mathrm{s}} = n e^{\beta \Psi_{\mathrm{s}}}, \tag{2.14}$$

$$p_{\mathrm{s}} = p e^{-\beta \Psi_{\mathrm{s}}}, \tag{2.15}$$

with n_{s} and p_{s} being the electron and hole concentrations at the silicon surface, Ψ_{s} being the surface potential, and β the inverse thermal voltage. The thermal voltage is calculated by $\beta = q/kT$, with q being the elementary charge.

The surface recombination rate due to the interface states U_{it} contributes to the total surface recombination rate U_{s}. But also the recombination rate within the space-charge region U_{sc} [28] can contribute to the total surface recombination rate U_{s}, if a band bending occurs towards the surface. Both contributions are additive, i.e., $U_{\mathrm{s}} = U_{\mathrm{it}} + U_{\mathrm{sc}}$. Recombination at the surface, in contrast to the other recombination paths, is a localized process, thus the influence of U_{s} on the total lifetime τ_{tot} depends on the amount of electron-hole pairs reaching the surface. To account for this fact commonly an effective surface recombination velocity (SRV) S_{eff} is defined as

$$S_{\mathrm{eff}} \equiv \frac{U_{\mathrm{s}}}{\Delta n_{\mathrm{sc}}} = \frac{U_{\mathrm{it}} + U_{\mathrm{sc}}}{\Delta n_{\mathrm{sc}}} = S_{\mathrm{it}} + S_{\mathrm{sc}}, \tag{2.16}$$

with Δn_{sc} being the excess carrier concentration at the edge of the space-charge region, S_{it} the surface recombination directly at the surface, and S_{sc} the surface recombination within the space charge region.

2.2.1 Calculation of S_{it}

In order to calculate S_{it}, knowledge of the concentration of the electrons and holes directly at the silicon surface is needed. Hence, the surface potential Ψ_{s} is required to calculated n_{s} and p_{s}. The surface potential Ψ_{s} cannot be calculated directly but the charge induced by the band bending in the silicon close to the surface $Q_{\mathrm{s}}(\Psi_{\mathrm{s}})$ and the charge stored in the interface traps $Q_{\mathrm{it}}(\Psi_{\mathrm{s}})$ are both dependent on the surface potential [29].

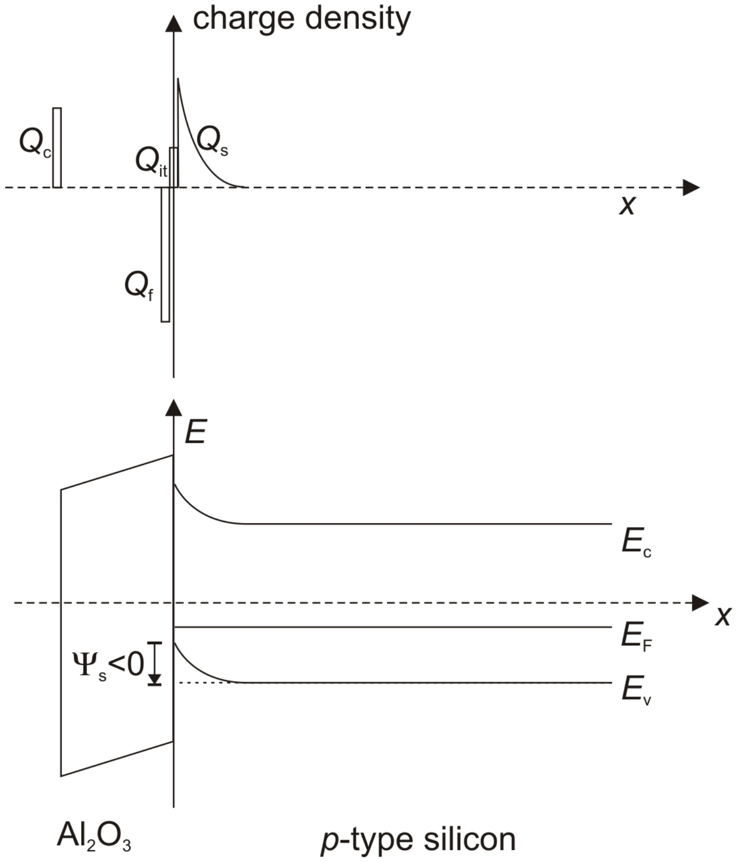

Figure 2.1: Charge distribution (top) and energy diagram (bottom) at the Al_2O_3/silicon interface, shown exemplary for *p*-type Si. The various symbols are defined in the text, the arrow pointing down denotes a negative surface potential Ψ_s.

$Q_s(\Psi_s)$ and $Q_{it}(\Psi_s)$ are not the only charges at the interface, depending on the dielectric layer also a fixed charge in the dielectric layer Q_f may be present and also supplementary charges Q_c, e.g., due to Corona charging, can be present. Due to charge neutrality, the sum of all these charges at the interface has to be zero. In order to calculate the interface charges Q_s and Q_{it}, all other involved charges have to be known and since Q_s and Q_{it} both depend on Ψ_s, an iterative numerical procedure has to be applied. The procedure used in this work was introduced by Girisch et al. [29] and is based on minimizing the deviation δ from charge neutrality:

$$Q_s(\Psi_s) + Q_{it}(\Psi_s) + Q_f + Q_c = \delta. \tag{2.17}$$

The arbitrary starting value of Ψ_s is changed until the neutrality condition $\delta < 1$ cm^{-2} is reached. $Q_s(\Psi_s)$ is calculated using the following equation [29, 30]:

$$Q_\mathrm{s}(\Psi_\mathrm{s}) = -\mathrm{sgn}(\Psi_\mathrm{s})\sqrt{\frac{2\epsilon_\mathrm{Si}}{q\beta}\left[p\left(e^{-\beta\Psi}-1\right)+n\left(e^{\beta\Psi}-1\right)+\beta\Psi(n_0+p_0)\right]}, \tag{2.18}$$

where $\epsilon_\mathrm{Si} = 11.7\epsilon_0$ is the dielectric permittivity of silicon. $Q_\mathrm{it}(\Psi_\mathrm{s})$ is calculated using the following equation [29]:

$$Q_\mathrm{it}(\Psi_\mathrm{s}) = \int_{E_\mathrm{v}}^{E_\mathrm{c}} [D_\mathrm{it,d}(E)f_\mathrm{d}(E,\Psi_\mathrm{s}) - D_\mathrm{it,a}(E)f_\mathrm{a}(E,\Psi_\mathrm{s})]dE, \tag{2.19}$$

with $D_\mathrm{it,a}(E)$ and $D_\mathrm{it,d}(E)$ being the acceptor and donor interface state densities, respectively. Under steady-state conditions, the electron occupancy function f_a and the hole occupancy function f_d are given by the expression [25, 29]:

$$f_\mathrm{a}(E,\Psi_\mathrm{s}) = \frac{\sigma_n n_\mathrm{s} + \sigma_p p_1}{\sigma_n(n_\mathrm{s}+n_1)+\sigma_p(p_\mathrm{s}+p_1)}, \tag{2.20}$$

$$f_\mathrm{d}(E,\Psi_\mathrm{s}) = \frac{\sigma_n n_1 + \sigma_p p_\mathrm{s}}{\sigma_n(n_\mathrm{s}+n_1)+\sigma_p(p_\mathrm{s}+p_1)}. \tag{2.21}$$

Since the separation of $D_\mathrm{it,a}(E)$ and $D_\mathrm{it,d}(E)$ is not possible with most characterization methods, we use the commonly made assumption that half of the interface states are donor and half are acceptor states:

$$D_\mathrm{it,a}(E) = D_\mathrm{it,b}(E) = \frac{D_\mathrm{it}(E)}{2}. \tag{2.22}$$

As long as the donor and acceptor interface states are equally distributed, this leads only to a small error, however, for distributions where one of the two kinds exceeds the other, the assumption (Eq. (2.22)) would lead to a major error in the calculation of Q_it. Still, this would have, in most cases discussed in the thesis, no major influence, as if only one type of interface state exists, the maximum Q_it would be $E_\mathrm{g}D_\mathrm{it}$ and, therefore, below 10^{11} cm^{-2}, whereas for Al_2O_3 the $|Q_\mathrm{f}|$ is in the range of 10^{12} to 10^{13} cm^{-2}. With the knowledge of Ψ_s, the surface concentration of the electrons and holes can be calculated using Eq. (2.14) and (2.15) and S_it can be calculated using Eq. (2.16).

2.2.2 Surface passivation

One major effort in the quest to increase the energy conversion efficiency of silicon solar

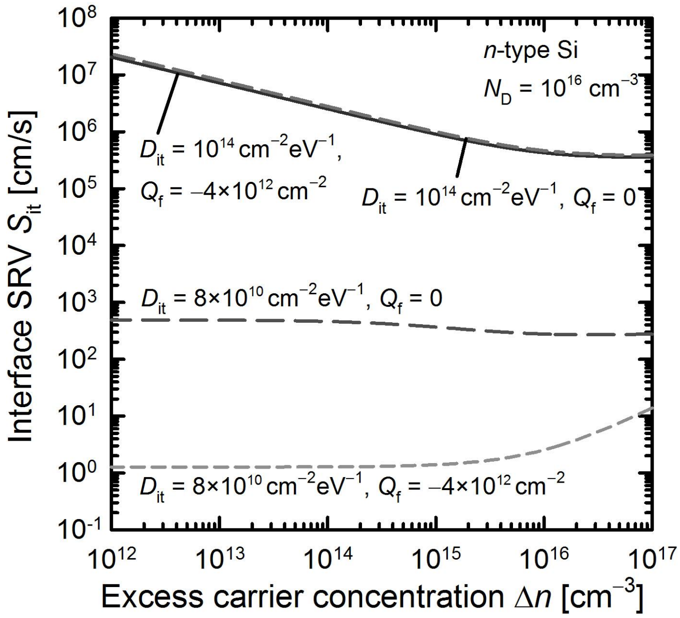

Figure 2.2: Interface SRV $S_{\mathrm{it}}(\Delta n)$ as a function of excess carrier concentration Δn for n-type silicon with $N_{\mathrm{D}} = 10^{16}$ cm^{-3}. The values for D_{it} and Q_{f} are varied and for the capture cross sections $\sigma_p = 4\times10^{-16}$ cm^2 and $\sigma_n = 7\times10^{-15}$ cm^2, as defined by Werner for the Al_2O_3 passivation [32].

cells of the last decades is to reduce the surface recombination losses. In general, there are two pathways to reduce the recombination at the surfaces.

The first is to reduce the number of dangling bonds. This is, e.g., realized by the deposition of a dielectric layer on top of the silicon surface and is sometimes called "chemical passivation". It is important to note that the saturation of the dangling bonds is not only due to bindings between the silicon and the dielectric layer, but also some of the dangling bonds are saturated by bindings with hydrogen atoms present within the dielectric layer. This chemical passivation can reduce the defect density $D_{\mathrm{it}}(E)$ by several orders of magnitude, leading to values around 10^{11} cm^{-2}eV^{-1} in the case of Al_2O_3 [31, 32]. This typical D_{it} value achieved by a dielectric layer, however, is not sufficient for an excellent surface passivation.

The second surface passivation mechanism is to deplete the surface of the silicon from either the electrons or the holes. This is often accomplished by using dielectric layers on top of the silicon that have a fixed charge density Q_{f}. In the case of Al_2O_3 this value is typically in the range of -3×10^{12} to -8×10^{12} cm^{-2} [31–34]. The depletion of one type of charge carrier can also be done by doping of the silicon near the surface, e.g., the in-diffusion of phosphorus doping atoms. This approach is often referred to as "field-effect" passivation. Although the nomination is misleading as not the electric field but the depletion of one type of charge carriers is the reason for the surface passivation.

For most passivation schemes, both mechanisms are important. In Fig. 2.2, $S_{\mathrm{it}}(\Delta n)$ is calculated using Eq. (2.16) shown for a n-type silicon sample with a donor concentration of $N_{\mathrm{D}} = 10^{16}$ cm^{-3}. Shown are computations of $S_{\mathrm{it}}(\Delta n)$ for a sample with $D_{\mathrm{it}} = 10^{14}$ cm^{-2}eV^{-1} as unpassivated reference and with $D_{\mathrm{it}} = 8\times10^{10}$ cm^{-2}eV^{-1} and $Q_{\mathrm{f}} = -4\times10^{12}$ cm^{-2} as a representational sample with Al_2O_3 passivation. Also shown are the results for negligible field-effect passivation ($Q_{\mathrm{f}} = 0$) and field-effect passivation without chemical passivation ($D_{\mathrm{it}} = 10^{14}$ cm^{-2}eV^{-1}). It can be seen that Q_{f} has no visible impact on the passivation if D_{it} is too large. In other words, to obtain a good field-effect passivation a descent chemical passivation is required.

2.2.3 Surface recombination including an inversion layer

Measurements of the passivation of n-type silicon surface by Al_2O_3 have shown a pronounced injection dependence of the SRV [7]. This injection dependence cannot be explained by the surface recombination contribution S_{it}. This can be seen in Fig. 2.3, where the calculated $S_{\mathrm{it}}(\Delta n)$ and the measured $S_{\mathrm{eff}}(\Delta n)$ of an Al_2O_3-passivated n-type silicon sample are shown. The measured $S_{\mathrm{eff}}(\Delta n)$ is extracted from the $\tau_{\mathrm{eff}}(\Delta n)$ measurement using Eq. (2.31). Hence, another recombination process connected with the passivation layer is needed to explain the pronounced measured injection dependence of $S_{\mathrm{eff}}(\Delta n)$. In the past, an increased recombination close to the surface caused by a damaged zone inside the space charge region was proposed to explain the injection dependence [35]. $S_{\mathrm{sc}}(\Delta n)$ can then be calculated using an extended Girisch formalism [28]. However, no direct experimental evidence supporting the theory of such a damaged zone was found so far. Another hypothesis includes asymmetric capture cross sections in the bulk, however, the experimental results are in disagreement with this assumption [36]. Kessler et al. [37] gave a different explanation for injection-dependent lifetimes of n-type Si samples with boron-diffused p^+-emitters. They showed that the injection dependence of $S_{\mathrm{eff}}(\Delta n)$ measured on these samples resulted partly from recombination at the sample edges coupled to the center wafer regions by the p^+-emitter, and is therefore dependent on the sample size. In the following, we will evaluate if a similar effect might explain the pronounced $S_{\mathrm{eff}}(\Delta n)$ dependence measured on Al_2O_3-passivated n-type silicon samples, where a hole-conducting inversion layer due to the high negative fixed charge density in the Al_2O_3 is present instead of a diffused p^+-emitter.

In Chapter 5, this novel hypothesis will be evaluated using Sentaurus Device simulations [38]. In the following, we give a brief overview of an analytical model presented

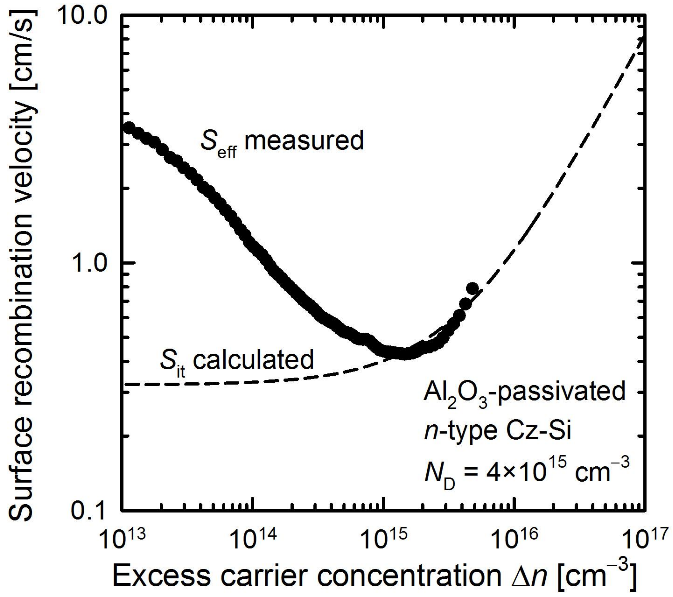

Figure 2.3: Calculated S_{it} and measured S_{eff} as a function of Δn for n-type silicon with $N_{\mathrm{D}} = 4\times10^{15}$ cm^{-3} passivated with $\mathrm{Al_2O_3}$. For the calculation a D_{it} of 4×10^{10} cm^{-2}eV^{-1} and a Q_{f} of -4×10^{12} cm^{-2} were used and for the capture cross sections $\sigma_p = 4\times10^{-16}$ cm^2 and $\sigma_n = 7\times10^{-15}$ cm^2, as defined by Werner for the $\mathrm{Al_2O_3}$ passivation [32].

by Black [39] for $\mathrm{Al_2O_3}$-passivated n-type silicon samples with localized areas of high surface recombination and adapt it to homogeneously passivated samples.

Black [39] describes the total surface recombination as a current flowing through a resistive network. The parts of the resistive network are (i) the surface recombination resistance $R_{\mathrm{rec,s}}$ and in parallel (ii) the transport resistance for the holes $R_{\mathrm{t,h}}$ and electrons $R_{\mathrm{t,e}}$ and the recombination resistance for the edge, or a localized high-recombination region, $R_{\mathrm{rec,ed}}$, see Fig. 2.4. All resistances are in units of Ωcm^2.

The surface recombination resistance $R_{\mathrm{rec,s}}$ is calculated using

$$R_{\mathrm{rec,s}} = \frac{kT}{q^2 S_{\mathrm{it}} \Delta n}. \tag{2.23}$$

The transport resistance for the electrons is given by the resistivity of the bulk and an area factor A_l:

$$R_{\mathrm{t,e}} = \frac{2A_l}{q\mu_{\mathrm{n,bulk}} W (N_D + \Delta n)}, \tag{2.24}$$

with W being the sample thickness and $\mu_{\mathrm{n,bulk}}$ the mobility of the electrons in the silicon bulk. According to Black [39] the area factor A_l depends on the distribution of the areas of high surface recombination, however, he does not show how this factor can be obtained other than by fitting the measured data. He further states that in the case

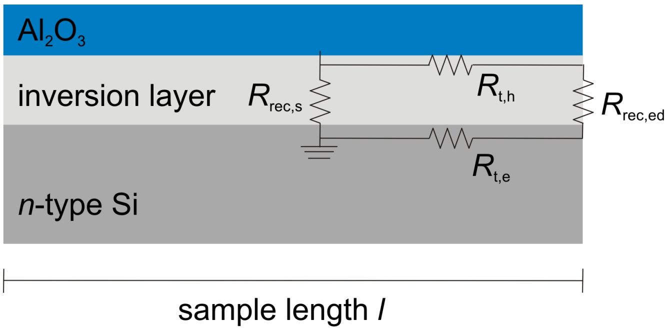

Figure 2.4: Schematic of the first few µm of an n-type silicon sample passivated with Al_2O_3. In the schematic, the inversion layer is shown and the lumped circuit model as proposed by Black [39].

of a homogeneous passivation where only the edges contribute to the recombination the factor is in "the order of the sample area" [39].

The transport resistance for the holes is given by the sheet resistance R_{sheet} of the inversion layer:

$$R_{\text{t,h}} = A_l R_{\text{sheet}} = \frac{A_l}{|Q_{\text{s}}| q \mu_{\text{p,inv}}}, \tag{2.25}$$

with $\mu_{\text{p,inv}}$ being the average mobility of the holes in the inversion layer. The total resistance is given by

$$\frac{1}{R_{\text{rec,tot}}} = \frac{1}{R_{\text{rec,s}}} + \frac{1}{R_{\text{t,h}} + R_{\text{t,e}} + R_{\text{rec,ed}}}. \tag{2.26}$$

This total resistance is related to S_{eff} by

$$S_{\text{eff}} = \frac{kT}{q^2 R_{\text{rec,tot}} \Delta n}. \tag{2.27}$$

The second summand on the right-hand side of Eq. (2.26) can be identified with the surface recombination induced by the edge S_{edge}

$$S_{\text{edge}} = \left[\frac{q^2 \Delta n (R_{\text{t,h}} + R_{\text{t,e}})}{kT} + \frac{1}{S_{\text{it,ed}}} \right]^{-1}. \tag{2.28}$$

Using Black's analytical model we are now able to calculate S_{eff} including the edge recombination. In Fig. 2.5, this is done for the n-type silicon sample of Fig. 2.3. The sample is 4×4 cm^2 large and is passivated with Al_2O_3. For the area factor A_l the value 0.16 cm^2 was used. The $S_{\text{eff}}(\Delta n)$ dependence is described very well with this semi-empirical model, especially since $\tau_{\text{eff}}(\Delta n)$ is measured using the photoconductance decay (PCD) method. The PCD method measures the average lifetime over an area

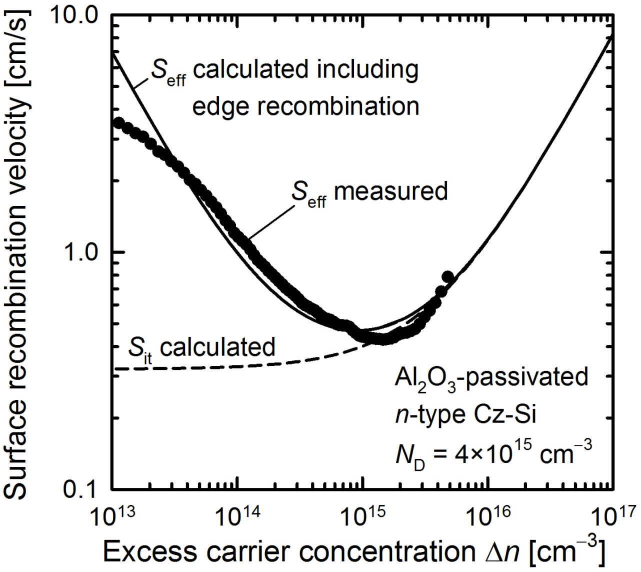

Figure 2.5: Calculated S_{it} and S_{eff} and measured S_{eff} as a function of Δn for n-type silicon with $N_{\text{D}} = 4\times10^{15}$ cm^{-3} passivated with Al_2O_3, the interface parameter are the same as in Fig. 2.3. The sample is 4×4 cm^2 large. For the calculation of the edge recombination a sheet resistance of 15 kΩ of the inversion layer, an A_l of 0.16 cm^2, and as parameters for the edge no surface charge and an D_{it} of 10^{12} cm^{-2}eV^{-1} were used.

of several cm^2 and the model only calculates the S_{eff} in the center of the sample. In Chapter 5, we apply numerical Sentaurus Device simulations and solve the full coupled semiconductor equations to model the $S_{\text{eff}}(\Delta n)$ dependence. We will demonstrate that excellent agreement with the measurements is obtained using this approach.

2.3 Effective carrier lifetime

With knowledge of the surface recombination and the recombination in the bulk, we are now able to calculate the effective lifetime of the excess carriers in the silicon. This is done by using Eq. (2.2):

$$\frac{1}{\tau_{\text{eff}}} = \frac{1}{\tau_{\text{b}}} + \frac{2S_{\text{eff}}}{W}. \tag{2.29}$$

This equation, however, is only valid for a homogeneous distribution of the excess carriers over the sample thickness and sufficiently high carrier mobilities in the bulk. In addition, it is only a good approximation for surface recombination velocities $S_{\text{eff}} \ll D/W$ [40], with D being the minority carrier diffusion coefficient. A more general equation is [40, 41]:

$$\frac{1}{\tau_{\text{eff}}} = \frac{1}{\tau_{\text{b}}} + \frac{2S_{\text{eff}}}{W}\left(\frac{\alpha D}{\alpha D + 2S_{\text{eff}}W}\right). \tag{2.30}$$

In this equation, $\alpha = \pi^2$ for the PCD measurements [40] and $\alpha = 12$ for the quasi-steady-state photoconductance (QSSPC) measurements [41]. For a description of the two measurement methods see Section 3.2.1. In most cases S_{eff} has to be extracted from the measured τ_{eff} and, therefore, Eq. (2.30) is transformed into an equation for S_{eff}:

$$S_{\text{eff}} = \frac{W}{2}\left[\left(\frac{1}{\tau_{\text{eff}}} - \frac{1}{\tau_{\text{b}}}\right)^{-1} - \frac{W^2}{\alpha D}\right]^{-1} . \tag{2.31}$$

Equation (2.31) is used throughout this work for the extraction of S_{eff} values from τ_{eff} measurements.

Chapter 3

Experimental details

In this Chapter, the methods used for the Al_2O_3 deposition and for the characterization of the samples are described. First, we take a closer look at the atomic layer deposition (ALD). In this work two different ALD processes are used, the sequential ALD process, abbreviated "ALD" throughout this thesis, and the spatial ALD process, abbreviated with "S-ALD". The third deposition method is the plasma-enhanced chemical vapor deposition (PECVD) using an inductively coupled plasma (ICP).

In the second part of this Chapter, we will discuss the main characterization methods used in this work, starting with the photoconductance decay (PCD) and the quasi-steady-state photoconductance (QSSPC) techniques. For the measurement of the spatial distribution of the carrier lifetime two methods are used, (i) the photoconductance-calibrated photoluminescence imaging (PC-PLI) and (ii) the infrared lifetime imaging (ILM) methods. For the measurement of negative fixed charge density Q_{f}, the so-called Corona-lifetime method is used. This methods also allows to extract the surface recombination velocity parameter S_0. The interface state density D_{it} is measured using the capacitance–voltage (C–V) analysis.

3.1 Deposition methods

The interface quality between the silicon sample and the dielectric layer Al_2O_3, and hence, the passivation quality, depends strongly on the deposition method applied. Therefore, it is important to compare different deposition methods. In the past, the plasma-assisted (PA)-ALD has already proven to provide an excellent surface passivation quality, with S_{eff} values below 1 cm/s on p-type and n-type silicon [6, 7, 42]. However, the relatively low deposition rate of this method is not suitable for industrial

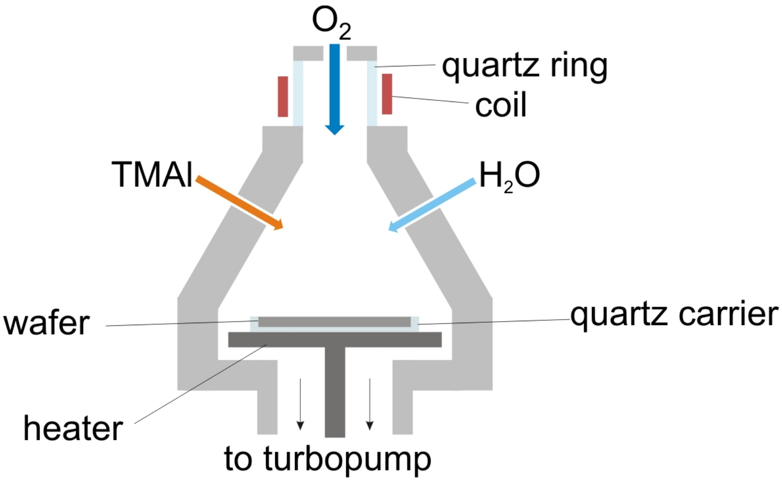

Figure 3.1: Schematic of the sequential ALD reactor FlexAL® (Oxford Instruments) used throughout this work.

application and, therefore, alternatives are needed. In recent years, several methods of Al_2O_3 deposition for the silicon surface passivation were investigated, namely atmospheric pressure chemical vapor deposition (APCVD) [43], reactive sputtering [44] and PECVD [11]. In this work, the S-ALD technique and, for the first time, the ICP-PECVD are investigated for the deposition of Al_2O_3 layers. Since PA-ALD Al_2O_3 layers provide the best surface passivation reported so far [6], this method is used as a reference.

3.1.1 Atomic layer deposition (ALD)

The principle idea of the ALD process is to use a series of self-limiting partial reactions. By alternating the partial reactions, the desired material is grown atomic layer by layer. In the case of Al_2O_3, two self-limiting half-reactions are used [45].

Sequential ALD

The sequential ALD process for the deposition of Al_2O_3 consists of four steps that are repeated several times, typically between 80 and 160 times, in order to grow a thin layer (10-20 nm) of Al_2O_3. In the following, the process is briefly described.

The process starts with a silicon sample that receives a chemical cleaning. In this work, the so-called RCA cleaning sequence is applied [46], in order to remove any metallic and organic contaminations from the wafer surfaces. Subsequent to the cleaning, the samples are transfered on a quartz carrier into the deposition chamber of a FlexAL® (Oxford Instruments) tool. For a schematic of the deposition chamber see Fig. 3.1. The sample is positioned on a heating stage that is heated to 200 °C for PA-ALD and 260 °C for thermal ALD. First, the chamber is pumped down to a pressure below 10^{-7} bar for 1 minute. Than a flow of 60 sccm O_2 is injected into the chamber and the pressure is increased to 1.3×10^{-4} bar for 1 minute, which helps to improve the thermal coupling between the sample and the heating stage and, therefore, increases the heating rate. A flow of 60 sccm O_2 is maintained during the entire process. After the 1 minute heating the pressure is reduced to 2×10^{-5} bar and the ALD deposition starts:

1. The valve of the delivery line of the precursor gas trimethylaluminium (TMAl) is opened for 20 ms and the TMAl is introduced into the deposition chamber. The TMAl reacts with the native oxide on top of the silicon surface and the first mono-layer of Al_2O_3 is formed and methylaluminium groups remain on the surface.

2. The remaining TMAl molecules cannot react with the Al atoms at the Al_2O_3 surface and are purged with O_2 out of the deposition chamber. This step is 1.5 s long.

3. The second precursor gas is introduced into the chamber, which is water (H_2O) in the case of thermal ALD, or an oxygen plasma in the case of PA-ALD. Depending on the gas, this step is between 60 ms (H_2O) or 2 s (oxygen plasma). The oxygen plasma is generated using an ICP setup and a power of 400 W. As shown in Fig. 3.1, the coil is positioned above the sample and, therefore, this plasma is a remote plasma. The oxygen reacts with the methylaluminium groups by replacing the methyl. After this step the surface atoms of the Al_2O_3 are oxygen or hydrogen again.

4. The remaining precursor gas and methyl groups are purged out of the deposition chamber using O_2. The length of this step also depends on the used precursor gas, for H_2O it is 4 s and for the oxygen plasma only 0.4 s.

The described cycle of the deposition has to be repeated several times, in order to grow a film of several nm thickness. Since the sequential ALD consists of cycles it is common to not state a deposition rate, but a growth per cycle (GPC) value in nm/cycle. In the case of the thermal ALD the GPC is 0.08 nm/cycle and in the case of PA-ALD 0.12 nm/cycle. Taking the length of one cycle, as described above, into account it is possible to calculate the effective deposition rate per unit of time. This is

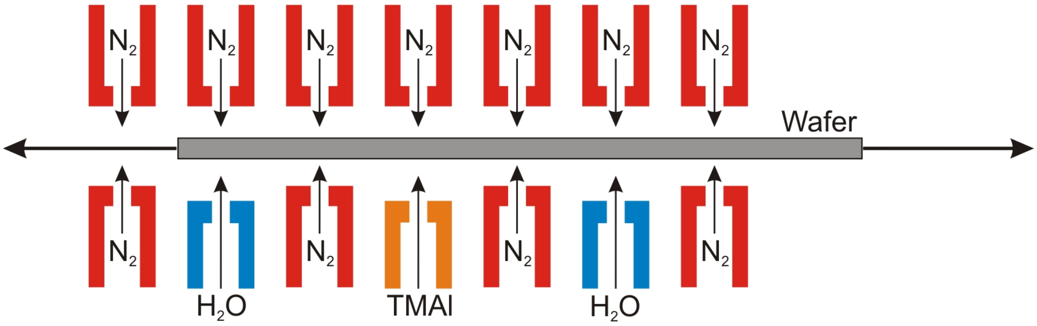

Figure 3.2: Schematic of the spatial ALD reactor of the InPassion LAB (SoLayTec) used throughout this work.

0.86 nm/min for the thermal ALD and 1.85 nm/min for PA-ALD. It has to be noted that the oxidizing step is not a true self-limiting reaction. Depending on the step length, it is possible to incorporate more oxygen or even H_2O, depending on the oxygen precursor used, into the Al_2O_3 layer than found in stoichiometric Al_2O_3. For a longer purging step, however, even a desorption of the O_2 is possible. This is especially relevant in the case of H_2O, where a long purging step is required after the H_2O dose. These might be an additional reason for the different GPC values for PA-ALD and thermal ALD.

Spatial ALD

The main difference between spatial ALD and sequential ALD is the separation of the two half-reactions. In the case of sequential ALD, the separation is in time, whereas in the case of spatial ALD the separation is in space. The separation in space is especially beneficial for thermal ALD, since the purge time for thermal ALD (5.5 s) is the main reason for the low deposition rate.

The spatial ALD tool used throughout this work is the commercially available InPassion LAB (SoLayTec). In this tool, the wafers are transported on an N_2 cushion into and through the deposition chamber. Due to this transport technology, the size and shape of the samples is crucial for a reliable transportation. Normally, only wafer with an edge length of 156 mm can be used. For our experiments this poses an issue, since high-purity wafers are frequently available with an edge length of only 125 mm. Inside the deposition chamber, the samples are moved by N_2 blasts periodically over the injector head with a frequency of ~1.2 Hz. A schematic of the injector head can be seen in Fig. 3.2. The H_2O injector and the TMAl injector are spatially separated by N_2 injectors, which produce N_2 curtains that separate the two precursor gases and form separated deposition chambers. Since the wafer is periodically moved from one side

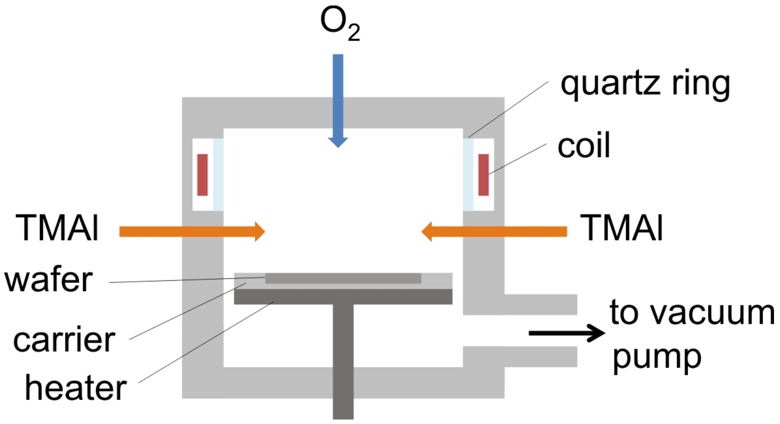

Figure 3.3: Schematic of the ICP-PECVD reactor (Von Ardenne CS 400 P) used in this work.

of the reactor head to the other, in this configuration two H_2O injectors are placed to allow the deposition of two cycles per period. This setup allows high deposition rates of over 10 nm/min. Another difference between the sequential ALD and the spatial ALD is the delivery of the precursor gases. In the case of the sequential ALD used in this work, the H_2O and TMAl are liquid and are evaporated due to the vapor pressure. In the case of the InPassion LAB, the liquid precursors are injected into a stream of N_2 gas and, therefore, vaporized. The amount of vaporized precursor is held fix to a value of 3 g/h for TMAl and 15 g/h for H_2O, thus, allowing a better control of the amount of TMAl and H_2O consumed. During the deposition, the wafers are not heated directly, but the run-in, the reactor and the gases are heated to 200 °C and, therefore, the wafer is at a temperature of $\sim$200 °C.

3.1.2 Plasma-enhanced chemical vapor deposition (PECVD)

Another method for the deposition of aluminum oxide applied in this thesis is the ICP-PECVD technique. This technique does usually not deposit perfectly stoichiometric aluminum oxide and, therefore, the aluminum oxide deposited by ICP-PECVD is abbreviated with AlO_x throughout this work. In this thesis, this process is realized in a laboratory-type Cluster System (Von Ardenne CS 400 P), consisting of a load-lock chamber, a transfer chamber, and several PECVD deposition chambers including the ICP-PECVD chamber. Figure 3.3 displays a schematic of the ICP-PECVD chamber. The silicon wafer is transfered on an aluminum carrier into the deposition chamber on a heating stage. This stage is heated to 400 °C, however, the wafer temperature is only at $\sim$120 °C during the deposition. A coil outside the vacuum chamber inductively excites the O_2 into a plasma using a high-frequency generator at 13.56 MHz. The other process gas used is TMAl, as also used for the ALD processes. Depending on the process parameters, deposition rates of up to 5 nm/s can be achieved.

3.2 Characterization techniques

In the following, we will give a brief overview of the measurement techniques applied throughout this thesis.

3.2.1 Photoconductance-based lifetime measurements

Photoconductance-based lifetime measurements are one of the standard measurement techniques for the determination of the effective carrier lifetime of silicon samples. In this thesis, mostly the WCT-120 (Sinton Instruments) was used. In Fig. 3.4, a schematic of the WCT-120 setup is shown. The WCT-120 uses the eddy-current method. During the measurement, the sample is placed above a coil trough which an alternating current flows, generated by a RF generator. This setup allows to measure contactless the conductivity σ of the silicon sample. In order to extract the conductivity from the measurement, the setup is calibrated by measuring samples of different known conductivity.

The conductivity σ of the silicon sample depends on the electron n_0 and hole p_0 concentrations within the silicon [47]:

$$\sigma_{\text{Si}} = qW(n_0\mu_n + p_0\mu_p), \tag{3.1}$$

with $\mu_{n/p}$ being the electron/hole mobility. Please note that the carrier mobilities depend on the carrier concentrations as well [48]. After placing the sample on the measurement stage, the flash lamp is triggered. The light generates excess carrier in the silicon and the excess carriers change the conductivity into [47]

$$\sigma_{\text{light}} = qW\left[(n_0 + \Delta n)\mu_n + (p_0 + \Delta n)\mu_p\right] = \sigma_{\text{Si}} + \Delta\sigma. \tag{3.2}$$

and

$$\Delta\sigma = qW\Delta n(\mu_n + \mu_p). \tag{3.3}$$

With the measurement of the time-resolved change of the conductivity, the carrier lifetime can be extracted. The setup allows to apply two different measurement methods.

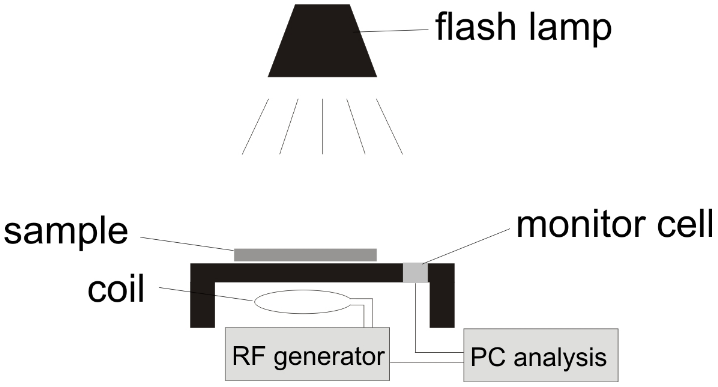

Figure 3.4: Schematic of the photoconductance measurement setup (WCT-120, Sinton Instruments).

The first is the photoconductance decay (PCD) and the second the quasi-steady-state photoconductance (QSSPC) method. In the following, these two methods will be described in more detail.

Photoconductance decay (PCD)

In a transient PCD measurement, ideally an infinitely short light pulse is used. In the setup of the WCT-120, this is realized by a flash that is only ~30 µs long. After the end of the flash there are still excess carriers present in the silicon, if their lifetime is much larger than the flash time constant, which is usually the case for surface-passivated silicon samples. The decay of the excess carriers is monitored by recording the change in the conductivity, see Fig. 3.5(a), and hence, the decay of the excess carrier concentration [47]

$$\Delta n(t) = \frac{\Delta\sigma(t)}{qW(\mu_n + \mu_p)}, \tag{3.4}$$

using a realistic mobility model [48]. From the recorded $\Delta n(t)$ decay, the effective lifetime is calculated using the equation [49, 50]

$$\tau_{\text{eff}} = -\frac{\Delta n(t)}{\frac{\partial \Delta n(t)}{\partial t}}. \tag{3.5}$$

For the determination of Δn the sample thickness needs to be known. Since the thickness can be determined using a dial indicator, this method is widely used and for lifetimes above 200 µs has a measurement error below 20% [6]. However, there are some limitation to the method. In particular, the effective lifetime of the examined silicon wafer has to be much larger than the time constant of the flash. Hence, in this thesis,

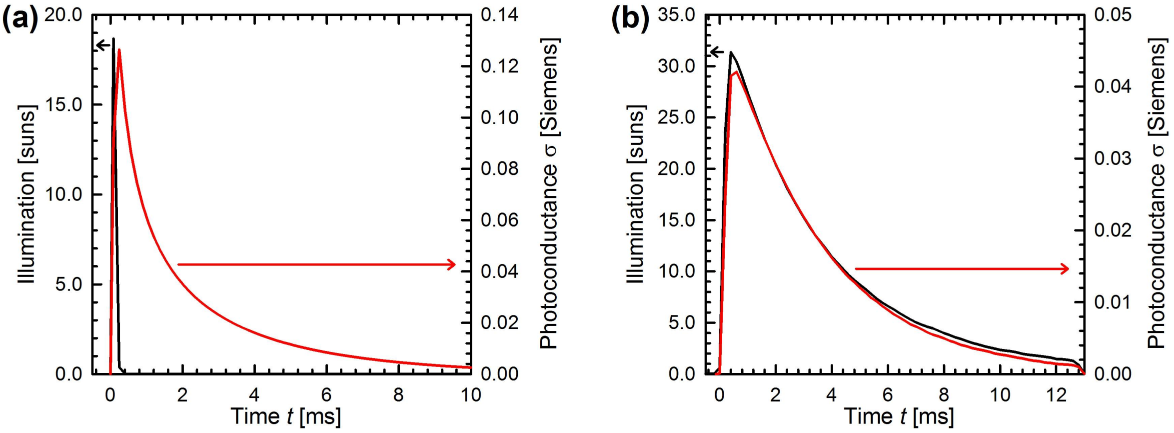

Figure 3.5: Exemplarily photoconductance measurements using the WCT-120, in (a) using the short flash pulse and in (b) using the long flash pulse.

the PCD technique is only used for samples with an effective lifetime above 100 µs.

Quasi-steady-state photoconductance (QSSPC)

In contrast to the PCD method, the QSSPC uses a long flash pulse with a decay time constant of ∼2.1 ms. This flash pulse has a high intensity at the beginning which exponentially decays over time, see Fig. 3.5(b) for an exemplarily measurement. For a steady-state generation rate G, the lifetime would be just the fraction of the excess carrier concentration and the generation rate [50, 51]:

$$\tau_{\text{eff}} = \frac{\Delta n}{G}. \tag{3.6}$$

Since the generation is not truely steady-state but depends on the time ($G(t)$), the effective lifetime has to be calculated using the generalized equation [50]:

$$\tau_{\text{eff}} = \frac{\Delta n(t)}{G(t) - \frac{\partial \Delta n(t)}{\partial t}}. \tag{3.7}$$

In order to determine the generation rate G, the WCT-120 has a calibrated monitor cell that shows a linear response to the illumination intensity. With this cell the photon flux is calculated. In contrast to the PCD method, the lifetime measured using the QSSPC is based on two different calibration procedures, the calibration of the conductivity and of the monitor cell and, depending on the quality of the calibration, prone to a higher uncertainty. In this work the the QSSPC measurement is used for lifetimes below 100 µs.

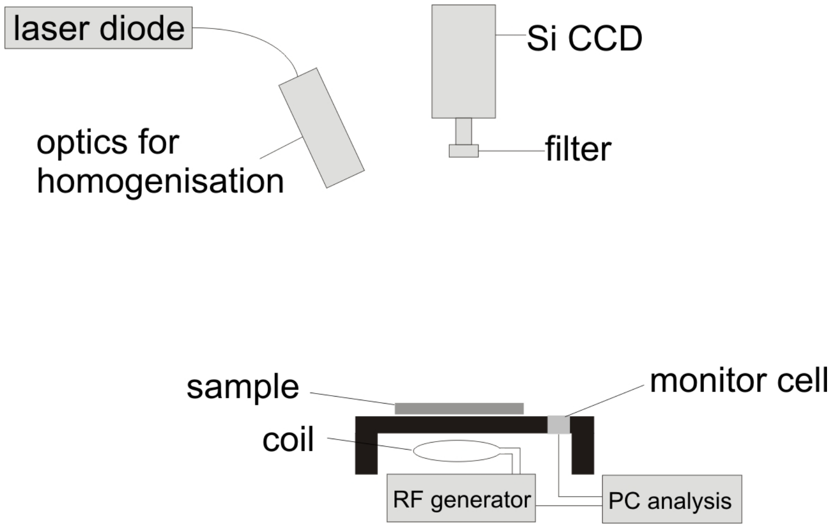

Figure 3.6: Schematic of the PC-PLI setup developed at ISFH [52].

3.2.2 Photoconductance-calibrated photoluminescence imaging (PC-PLI)

The photoconductance-calibrated photoluminescence imaging (PC-PLI) is carried out in an in-house developed setup [52], as shown in Fig. 3.6. The basic idea of the PC-PLI is to exploit the correlation between the photoluminescence intensity I_{PL} and the excess carrier concentration Δn, which is given by [52]

$$I_{\mathrm{PL}} \propto U_{\mathrm{rad}} = B_{\mathrm{low}} B_{\mathrm{rel}} np \approx B_{\mathrm{low}} B_{\mathrm{rel}} \Delta n (\Delta n + N_{\mathrm{A}}). \tag{3.8}$$

In the PC-PLI setup the sample is exited using a laser diode in continuous wave (cw) mode and, therefore, Eq. (3.6) is valid. The wavelength λ of the laser is 808 nm and the laser beam is homogeneously widened to illuminate an area of $\sim 20\times 20$ cm^2. The photoluminescence signal is detected using a Si CCD camera with a set of long-pass filters mounted on the objective, which prevents the detection of any reflected laser light. The detection of the PL signal alone does not allow the calculation of the lifetime. To do so the proportionality factor needs to be known. This factor depends on the optical parameters and the doping concentration of the wafer and, therefore, has to be determined for each sample. For the determination of the calibration factor, the photoconductance is measured based on the eddy-current method using a WCT-100 (Sinton Instruments).

Besides the measurement of the spatial distribution of the lifetime, one main benefit of the PC-PLI method is the lack of the depletion region modulation (DRM) [53]

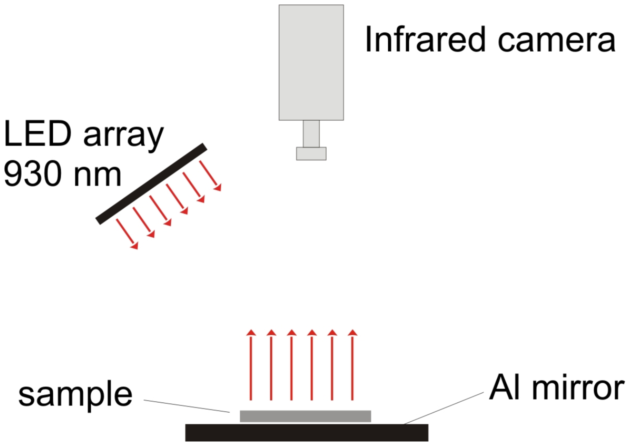

Figure 3.7: Schematic of the dynamic ILM setup developed at ISFH [55].

and the minority-carrier trapping effects [54]. The DRM is a measurement artifact for samples with an inversion layer, e.g., Al_2O_3 on n-type Si. Due to the presence of the inversion layer, the conductivity in low injection is not any more only dependent on the excess carrier concentration but also on the change of the depleted region close to the surface. Since the PC-PLI does not measure the conductivity, but the radiative recombination, the DRM does not effect the PC-PLI measurement. However, the photoconductance measurement used for the calibration is affected by the DRM and, therefore, the calibration has to be carried out at high excess carrier concentrations.

3.2.3 Dynamic infrared lifetime mapping (dynamic ILM)

The dynamic infrared lifetime mapping (dynamic ILM) technique [55] is another method to measure the spatial distribution of the effective lifetime. In contrast to the PC-PLI method, the dynamic ILM is based on the proportionality of the free carrier emission and the excess carrier concentration.

Figure 3.7 shows a schematic of the in-house developed setup [55]. The sample is placed on an aluminum mirror and is heated to 70 °C. Due to the elevated temperature, the free carrier emission is increased and, therefore, also the signal-to-noise ratio. However, the increased wafer temperature can lead to a different lifetime than when the sample is measured at 25 °C. The sample is illuminated using LED arrays that emit photons with a wavelength λ of 930 nm. An infrared camera placed above the sample detects light in the wavelength range from 4 to 5 µm emitted by the free carriers. Using a lock-in technique, the time dependence of the free carrier emission is measured, and hence, the time dependence of the excess carrier concentration and from this the effective lifetime is evaluated [55].

The main advantages of the dynamic ILM is a fast measurement within only a few seconds and that no calibration is needed. A drawback is the elevated measurement temperature and the fact that the setup does not allow the measurement at very low excess carrier concentrations.

3.2.4 Corona-lifetime measurements

The Corona-lifetime methodology [56] is a technique for the determination of the fixed charge density within a dielectric passivation layer.

The determination of the fixed charge density is performed by repeating the following sequence: First, the effective lifetime is measured. Subsequently, a known Corona charge density Q_c is deposited on the sample surfaces and the lifetime is measured again. The charge is deposited using a Corona chamber, see Fig. 3.8(a). Inside the Corona chamber, the sample is placed on a grounded metal plate. Above this plate a metal needle is mounted. Between the needle and the metal plate a high voltage, typically between 7 and 8 kV, is applied. Due to the high electric field strength close to the tip of the needle, the air molecules are ionized. The negative or positive ionized air molecules, depending on the polarity of the applied voltage, are accelerated towards the metal plate. Since the sample is placed on top of the metal plate, the Corona charges are deposited on the sample surface. Depending on the polarity of the applied voltage, the deposited charge is either positive or negative.

The amount of deposited Corona charges is measured using a Kelvin-probe [57] (TREK 320C, Trek Inc.), see Fig. 3.8(b). The Kelvin-probe does not measure the Corona charge directly, but the surface voltage V_s of the sample. This is done by placing a sample under the vibrating electrode of the Kelvin-probe in a distance of about 1-2 mm. The probe housing serves as reference surface and has in general a different surface voltage than the sample. Due to the electrostatic field between the sample and reference surface, an ac signal is induced in the vibrating electrode. This ac signal is fed into a feed-back circuit that drives the reference surface towards the same potential as the sample. Hence, the electrostatic field becomes zero and the induced ac signal vanishes. The Kelvin-probe does not measure the surface voltage of the sample directly, but the difference of the surface voltages between the reference and the sample surface. Therefore, typically the surface prior to the deposition is used as zero and only the change in surface potential is measured. With the change in surface voltage ΔV_s,

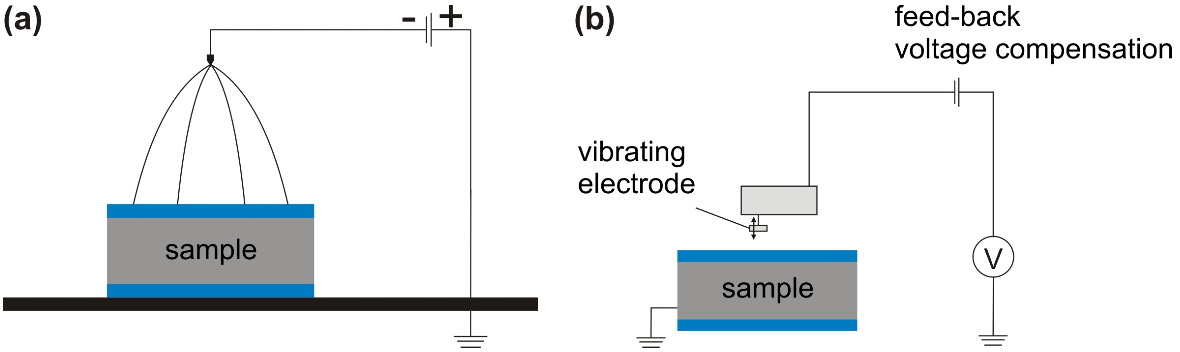

Figure 3.8: Schematic of (a) the Corona chamber and (b) the Kelvin-probe.

the amount of deposited Corona charge Q_c can be calculated using

$$\Delta V_\mathrm{s} = \frac{qQ_\mathrm{c}}{C_\mathrm{di}} + \Delta\Psi_\mathrm{s}(Q_\mathrm{c}), \tag{3.9}$$

with C_di being the dielectric capacity calculated using

$$C_\mathrm{di} = \frac{\epsilon_\mathrm{di}}{d_\mathrm{di}}, \tag{3.10}$$

with ϵ_di being the dielectric permittivity of the dielectric investigated and d_di the thickness. For the calculation of Q_c using Eq. (3.9), the knowledge of the dependency of the surface potential Ψ_s from the Corona charge is necessary. The change in Ψ_s can only be neglected for thick oxides, where Q_c has the same polarity as Q_f or $|Q_\mathrm{c}| \ll |Q_\mathrm{f}|$ and Eq. (3.9) is simplified to

$$\Delta V_\mathrm{s} = \frac{qQ_\mathrm{c}}{C_\mathrm{di}}. \tag{3.11}$$

In the case of very thin Al_2O_3 layers examined in this thesis, Eq. (3.11) leads to a measurement error of around 5%. Therefore, ΔQ_c was measured using a reference sample with a thick oxide.

Since the deposited Corona charge changes Ψ_s, the surface recombination rate is also changed, as can be seen from Eq. (2.13). This change in surface passivation is monitored by measuring τ_eff of the sample. The highest surface recombination velocity, denoted S_0, is in good approximation reached when the deposited Corona charge density Q_c equals $-Q_\mathrm{f}$. Figure 3.9 shows a measurement of a 0.9-Ωcm Ga-doped p-type Czochralski-grown (Cz)-Si sample passivated with a 5 nm thick S-ALD Al_2O_3 layer annealed for 20 min at 350 °C. The S_0 is measured for a Q_c of 3.6×10^{12} cm^{-2}, hence, the Q_f of the Al_2O_3 layer is -3.6×10^{12} cm^{-2}. The measured S_0 value can be used as quality factor

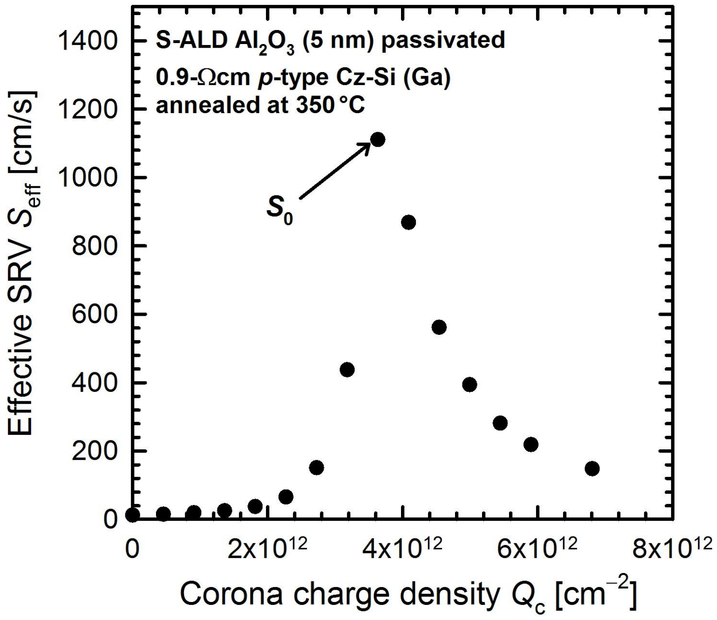

Figure 3.9: Effective SRV S_{eff} vs Corona charge density Q_{c} for an Al_2O_3 passivated 0.9-Ωcm Ga-doped p-type Cz-Si sample. The Al_2O_3 layer is deposited using S-ALD and has a thickness of 5 nm. The sample was annealed for 20 min at 350 °C.

for the chemical surface passivation.

This method for the measurement of Q_{f} has some measurement uncertainties. The S_0 value is reached for $n_{\mathrm{s}}\sigma_n = p_{\mathrm{s}}\sigma_p$ [56], for a strong asymmetry between σ_n and σ_p the S_0 is not measured for $Q_{\mathrm{c}} = -Q_{\mathrm{f}}$, instead, if σ_n exceeds σ_p, S_0 is shifted to lower Q_{c} values [56]. Calculations using the Girisch formalism introduced in Chapter 2 reveal that for asymmetric capture cross sections the shift of S_0 depends strongly on D_{it} and is maximal $\sim Q_{\mathrm{it}}$. For an annealed Al_2O_3 layer, this is only in the order of $10^{10} - 10^{11}$ cm^{-2} and can, therefore, be neglected. However, for samples with a high D_{it} this can have a significant influence. Another measurement uncertainty is the discrete step size of the Corona charging. In the used setup, the minimal step size is 4.54×10^{11} cm^{-2}. Another uncertainty is the spatial fluctuation of the fixed charge density in the dielectric layer and of the deposited Corona charge over the wafer area, see Werner [32] for more details. Besides the uncertainty of the measured Q_{f}, this all leads also to a high uncertainty of the measured S_0 value. Therefore, the measured S_0 has to be taken with caution when the interface quality of different passivation layers is compared with each other.

3.2.5 Capacitance–voltage (C–V) analysis

A detailed discussion of the capacitance–voltage (C–V) analysis can be found in literature [32, 39, 58]. Hence, in the following only a brief discussion of the measurement principle will be given, following the argumentation of Ref. 58, p. 94, pp. 323–332, and pp. 465–466 from which we take the succeeding equations (3.12)–(3.16). The C–V analysis is performed at metal-insulator-silicon (MIS) capacitors, in this work Al/Al_2O_3/Si, and is a combined measurement of the MIS capacity with the applied gate voltage V_g being superposed by a slowly varying and a fast varying small signal. The high-frequency capacitance is acquired from 1MHz small signal variation whereas the low-frequency capacitance is obtained from the transient MIS response upon change of gate voltage V_g. The main contribution to the capacitance of the MIS capacitor are the capacitance of the silicon C_s and in series the capacitance of the insulator C_{in}, however, during the low-frequency C–V measurement also the interface traps contribute to the measured capacitance resulting in an interface capacitance C_{it} in parallel to C_s. This C_{it} is due to the capture or release of an electron of the interface traps. The low-frequency capacitance C_{lf} is, therefore, given by:

$$C_{lf} = \left[\frac{1}{C_{in}} + \frac{1}{C_s + C_{it}}\right]^{-1}. \tag{3.12}$$

During the high-frequency C–V measurement, however, the response of the interface traps is to slow, and hence, they do not contribute to the high-frequency capacitance C_{hf} and the high-frequency capacitance C_{hf} is given by:

$$C_{hf} = \left[\frac{1}{C_{in}} + \frac{1}{C_s}\right]^{-1}. \tag{3.13}$$

With the measured C_{lf} and C_{hf} we are now able to calculate the D_{it} using the following equation

$$qD_{it} = C_{it} = \left[\frac{1}{C_{lf}} - \frac{1}{C_{in}}\right]^{-1} - \left[\frac{1}{C_{hf}} - \frac{1}{C_{in}}\right]^{-1}. \tag{3.14}$$

The influence of the applied gate voltage V_g on the surface potential Ψ_s is calculated using

$$\Psi_s(V_g) = \int_{V_{fb}}^{V_g} \left[1 - \frac{C_{lf}(V)}{C_{in}}\right] \mathrm{d}V. \tag{3.15}$$

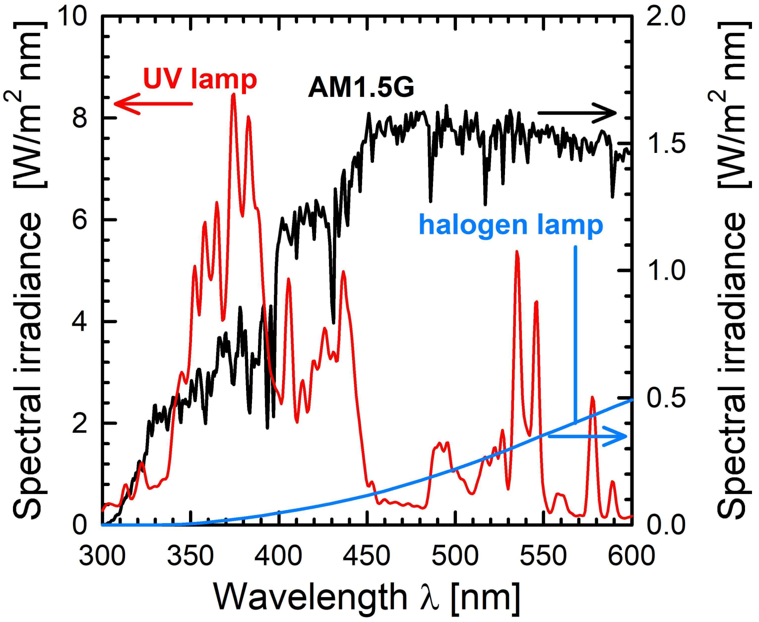

Figure 3.10: Measured spectral irradiance vs wavelength λ of the used UV and halogen lamps in comparison to the AM1.5G spectrum.

V_{fb} is defined as the flat-band voltage, and hence, $\Psi_{\mathrm{s}}(V_{\mathrm{fb}}) = 0$. V_{fb} can be calculated using the following equation

$$V_{\mathrm{fb}} = -\frac{Q_{\mathrm{f}}}{C_{\mathrm{in}}} - \frac{Q_{\mathrm{it(0)}}}{C_{\mathrm{in}}} + \phi_{\mathrm{ms}}, \tag{3.16}$$

with ϕ_{ms} being the work-function difference between the metal gate and the silicon bulk.

3.3 UV chamber

In order to investigate the stability of the surface passivation under UV irradiation ($\lambda \leq 400$ nm), a UV chamber is used. This UV chamber is build in house at the ISFH using UV lamps (UVASPOT by Höhnle) that emit mainly photons in the wavelength range between 300 and 600 nm, with 1% of the power emitted between 290 and 315 nm and 46% between 315 and 400 nm, see Fig. 3.10 for a comparison between the UV lamp, a halogen lamp, and the AM1.5G spectrum. For a better comparison, an equivalent illumination time with the AM1.5G is calculated. The AM1.5G has a power density of 46.3 W/m^2 in the UV ($\lambda \leq 400$ nm) and, therefore, a UV dose of 46.3 Wh/m^2 is equivalent to one hour of illumination with the AM1.5G spectrum. Since the illumination intensity of the UV lamps decreases over time, the intensity in the UV is monitored manually during the period of the experiment. The UV illumination intensity is in the range of 260 to 340 W/m^2.

Chapter 4

Impact of deposition technique and annealing on the passivation quality of Al_2O_3-passivated c-Si surfaces

In this Chapter, we examine the annealing behavior at moderate temperature for various types of passivation layers, followed by a detailed analysis of the different deposition methods, such as the PA-ALD, S-ALD and ICP-PECVD deposition, with the main focus on the behavior of the surface passivation under firing conditions. For the analysis of the surface passivation effective lifetime τ_{eff} and D_{it} is measured. Photoconductance decay (PCD) measurements are applied for the measurement of τ_{eff}. From the τ_{eff} measurements the S_{eff} is calculated using Eq. (2.31) and assuming only intrinsic recombination, calculated using $\tau_{\text{intr.Richter}}$ (2.10). The D_{it} is extracted from C–V measurements.

4.1 Surface passivation quality of low-temperature-annealed Al_2O_3

The initial effective lifetimes measured directly after Al_2O_3 deposition is low for all used deposition methods ($\sim$3 µs for PA-ALD and S-ALD and 20-100 µs for ICP-PECVD on 1.4-Ωcm p-type float-zone (FZ)-Si). After deposition of a SiN_x layer, a higher effective lifetime ($\geq$ 500 µs) is measured, which indicates that the deposition of SiN_x at a deposition temperature of $\sim$400 °C for several minutes has an effect similar to a short anneal.

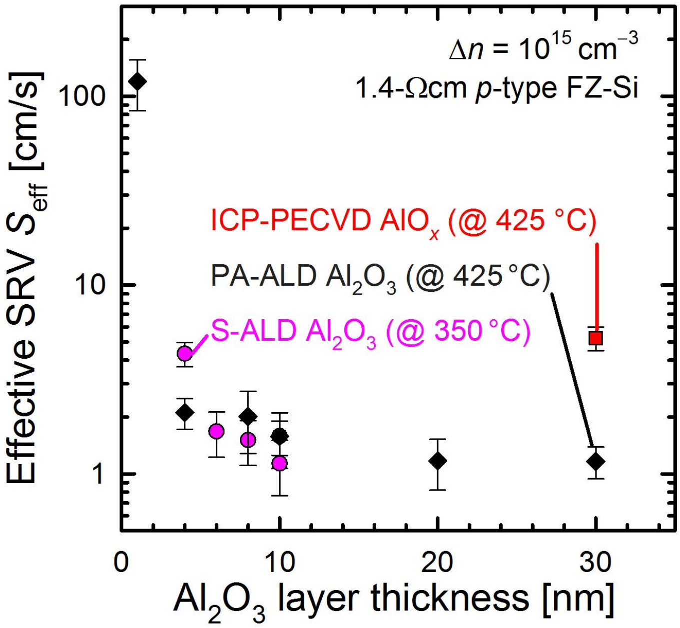

Figure 4.1: Effective SRV S_{eff} as a function of Al_2O_3 layer thickness for different deposition techniques. For the PA-ALD and S-ALD Al_2O_3 layers, the values are obtained measuring the lifetime of large (12.5×12.5 cm^2) samples at 9 location, the value for the ICP-AlO_x layer is the average of 3 small (2.5×2.5 cm^2) samples.

Figure 4.1 shows S_{eff} values extracted from PCD measurements as a function of the Al_2O_3 layer thickness deposited on 1.4-Ωcm p-type FZ-Si, using the PA-ALD and S-ALD deposition techniques. Also included is the result for a 30 nm thick ICP-AlO_x layer on 1.4-Ωcm p-type FZ-Si. Al_2O_3 layers deposited by PA-ALD and S-ALD provide a passivation quality that is almost independent on the layer thickness. Only for very thin layers, below 4 nm in the case of PA-ALD and 6 nm in the case of S-ALD, a decreased passivation quality is observable. Above this thicknesses the passivation quality is the same for both deposition techniques, with S_{eff}-values between 1 and 2 cm/s. The 30 nm thick ICP-AlO_x layer does not provide such an excellent passivation quality, with S_{eff} laying between 5 and 6 cm/s. This is mainly due to the smaller sample size of the ICP-AlO_x-passivated samples, 2.5×2.5 cm^2 instead of 12.5×12.5 cm^2. Small samples passivated with PA-ALD Al_2O_3 show an increased S_{eff} between 3 and 4 cm/s. The impact of sample size on lifetime will be discussed in more detail in Chapter 5. Therefore, the difference in passivation quality can be regarded as small. Also, the negative fixed charge density Q_{f} is found to be the same for all three deposition techniques $-(4\pm1)\times10^{12}$ cm^{-2}. For the surface passivation, however, also the interface defect density D_{it} is important, which will be evaluated in the next Section.

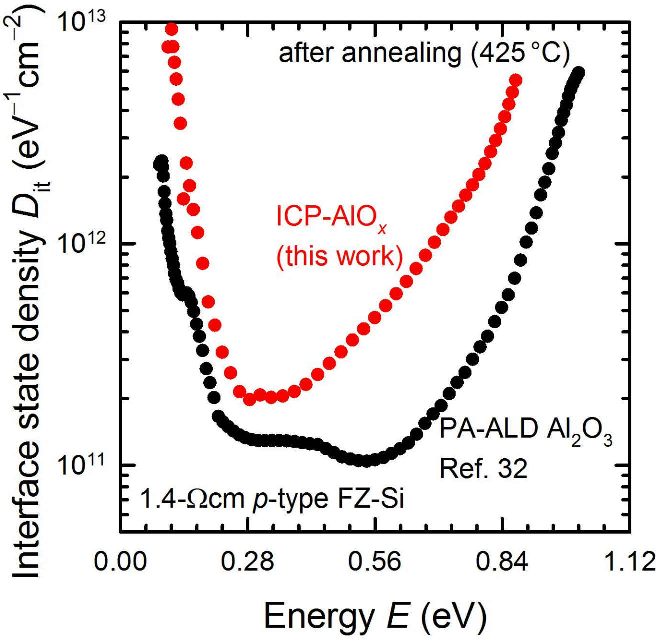

Figure 4.2: Interface state density D_{it} measured using C–V measurements as a function of energetic position $E = E_t - E_v$. Shown are the values for a 30 nm thick ICP-AlO$_x$ layer and a 30 nm thick PA-ALD Al_2O_3 layer after annealing at 425 °C. The data for the PA-ALD Al_2O_3 layer is taken from literature [32].

Interface state density D_{it}

For S-ALD and PA-ALD Al_2O_3 layers, the D_{it} was found to be very similar [32] whereas the D_{it} of the PA-ALD Al_2O_3 and ICP-AlO$_x$ layers on c-Si are different. In Fig. 4.2, the measured D_{it} values for an ICP-AlO$_x$ layer on p-type c-Si are shown. As reference also the D_{it} values for a PA-ALD Al_2O_3 layer, taken from the literature [32], are shown. Note that the PA-ALD and S-ALD Al_2O_3 layers as investigated by Werner [32] were deposited using the same tools as used in this work. It can be seen that the ICP-AlO$_x$ on c-Si shows a strong variation in D_{it} over the energetic position E with the minimum D_{it} value of $(2\pm0.5)\times10^{11}$ $eV^{-1}cm^{-2}$ around an energy of (0.33 ± 0.07) eV. Around midgap, D_{it} values of $(5\pm1)\times10^{11}$ $eV^{-1}cm^{-2}$ are recorded. The PA-ALD Al_2O_3 layer produces an approximately constant D_{it} of $(1\pm0.4)\times10^{11}$ $eV^{-1}cm^{-2}$ around midgap. Werner [32] analyzed the distribution of the D_{it} over the bandgap of PA-ALD Al_2O_3 on c-Si. Werner [32] proposed three different defects, with defect A being a continuously distributed defect throughout the bandgap, defect B having a Gaussian distribution centered around $E_0 = 0.85$ eV, and defect C having a Gaussian distribution around $E_0 = 0.50$ eV above the silicon valence band edge E_v. In order to model the $D_{it}(E)$ distribution of the ICP-AlO$_x$/c-Si interface, we assume that the same defect types are present. For defect B and C, the distribution is modeled using

$$D_{\mathrm{it}}(E) = D_{\max} \exp\left[-\frac{(E-E_0)^2}{2w}\right], \tag{4.1}$$

with w being the peak half width and $D_{\max}$ the peak height. According to Ref. 32, w is set at 0.015 eV^2. In Tab. 4.1, the resulting $D_{\max}$ values for our ICP-AlO_x layer in comparison with the results by Werner [32] for PA-ALD and S-ALD are shown. For the PA-ALD Al_2O_3, Werner [32] found that the C–V measurements induce a damage, and hence, $D_{\max}$ of defect B and defect C increases due to the C–V measurement. Therefore, in Tab. 4.1 both values are shown, called initial and degraded. The ICP-AlO_x/c-Si interface shows very similar $D_{\max}$ values as the degraded PA-ALD Al_2O_3/c-Si interface. In the case of the ICP-AlO_x layer, the damage could be a plasma-damage induced during the deposition process. The plasma used is a remote plasma, however, it is generated only some centimeters above the sample surface. In contrast to the PA-ALD Al_2O_3 layer, this damage, however, is not influenced by an annealing step. Measurements of Werner [32] show that defect B, with the highest $D_{\max}$ value, is not as recombination active as defect A due to a lower electron capture cross section σ_n [32]. Hence, the difference in surface passivation can be explained by an increased density of defect B, which is assumed to be related to a plasma damage during deposition.

4.2 PA-ALD Al_2O_3 layers

4.2.1 Firing of PA-ALD Al_2O_3 layers

In order to examine the behavior of the surface passivation quality provided by PA-ALD Al_2O_3 layers under firing conditions, experiments are performed in an industrial in-

Table 4.1: Defect density pre-factor $D_{\max}$ used to fit the D_{it} distribution. The values for PA-ALD and S-ALD are from literature [32].

Defect	ICP-PECVD	PA-ALD [32]		S-ALD [32]
		initial	degraded	
A $[\mathrm{eV}^{-1}\mathrm{cm}^{-2}]$	1.5×10^{11}	8×10^{10}	8×10^{10}	8×10^{10}
B $[\mathrm{eV}^{-1}\mathrm{cm}^{-2}]$	2×10^{12}	1.2×10^{11}	1.8×10^{12}	–
C $[\mathrm{eV}^{-1}\mathrm{cm}^{-2}]$	1.5×10^{11}	4×10^{10}	3×10^{11}	–

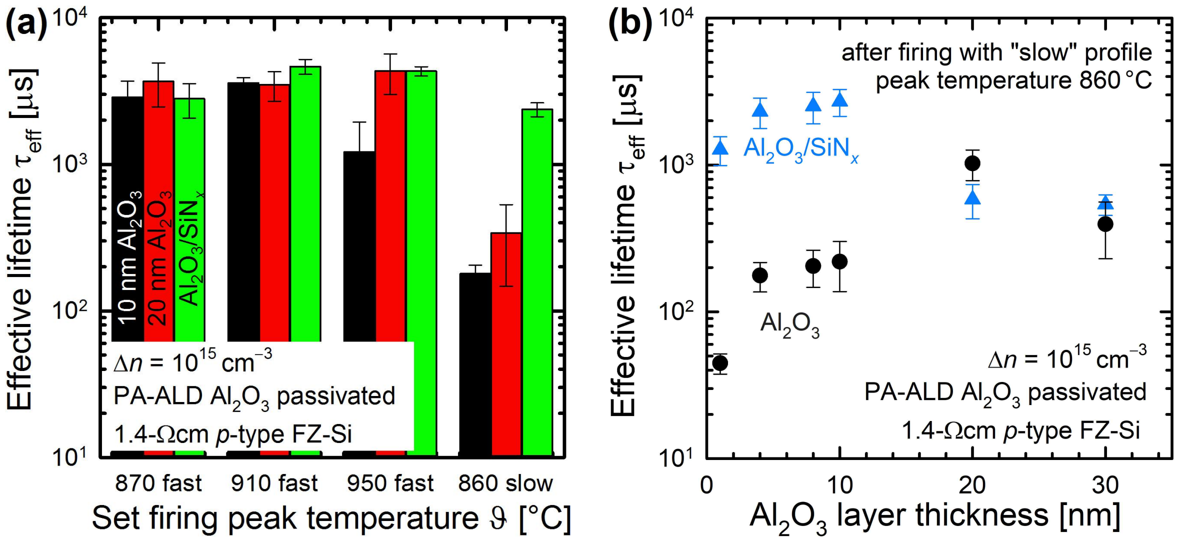

Figure 4.3: (a) Measured effective lifetime τ_{eff} as a function of firing profile and set-peak temperature. Shown are PA-ALD Al_2O_3 layers with 10 and 20 nm thickness and PA-ALD Al_2O_3/SiN_x stacks with 10 nm Al_2O_3 and 70 nm SiN_x. (b) Measured effective lifetime τ_{eff} as a function of PA-ALD Al_2O_3 layer thickness after firing using the slow firing profile with a set-peak temperature of 860 °C. Shown are the results for PA-ALD Al_2O_3 layers with and without a 70 nm SiN_x capping layer. The samples are measured at 9 locations on the samples using the PCD method and shown are the mean value and the standard deviation. All samples received no pre-firing anneal.

frared conveyor-belt furnace (Centrotherm Contact Firing Furnace DO-FF-8.600-300). For this experiment two different firing profiles are used, the first called "slow" firing profile consists of a belt speed of 3 m/min and a set-peak temperature of 860 °C. The second firing profile called "fast" consists of a belt speed of 5.9 m/min and a set-peak temperature between 870 and 950 °C. The fast firing profile represents typical firing conditions of the industrial production of screen-printed silicon solar cells.

When using the slow firing profile, the silicon is ~12 s above 600 °C compared to ~6 s for the fast firing profile with 910 °C set-peak temperature, whereas the peak temperature of the silicon is comparable (~810 °C for both profiles). Hence, the thermal budgets are the main difference between both profiles and not the peak temperatures.

Figure 4.3(a) shows the effective lifetime after firing using the slow firing profile with 860 °C and the fast firing profile with 870, 910, and 950 °C as set-peak temperatures. The effective lifetime is measured on 12.5×12.5 cm^2 1.4-Ωcm p-type FZ-Si samples passivated with 10 and 20 nm thick PA-ALD Al_2O_3 single-layers and PA-ALD Al_2O_3/SiN_x stacks (10 nm Al_2O_3 and 70 nm SiN_x). It can be seen that all layer systems provide a high lifetime after firing, using the fast firing profile. For the PA-ALD Al_2O_3 single-layers the highest lifetime of up to 6.3 ms is provided by the 20 nm thick PA-ALD

Al_2O_3 layer at the maximum set-peak temperature of 950 °C. The 10 nm single-layer in contrast provides at this set-peak temperature already a lower mean lifetime and also a strong gradient of the lifetime over the sample, with lifetimes of only 300 µs on one side and up to 2400 µs on the other side. A gradient in the lifetime is also observed for the 20 nm thick layer, however, not as pronounced with lifetimes ranging from 2.6 up to 6.3 ms. The reason for this gradient is the difference in the actual temperature over the sample surface during the firing step. For the samples fired at a set-peak temperature of 870 °C a gradient in the opposite direction is measured. The samples fired with a set-peak temperature of 910 °C show no gradient.

For the PA-ALD Al_2O_3/SiN_x stacks a peak temperature of 910 °C is optimal, resulting in lifetimes up to 5 ms, corresponding to S_{eff} values below 1 cm/s. When using the slow firing profile, the effective lifetime after firing decreases well below 1 ms for the PA-ALD Al_2O_3 single-layers, independently of the Al_2O_3 thickness. Hence, the slow firing profile is more detrimental to the PA-ALD Al_2O_3 single-layers compared to the PA-ALD Al_2O_3/SiN_x stacks, which still provide lifetimes > 2 ms, corresponding to S_{eff} values < 5 cm/s, after the slow firing. The results shown in Fig. 4.3(a) are obtained with samples that received no annealing step prior to the firing, however, samples that received an annealing step prior to the firing do not show any difference in lifetime. From this results it can be concluded that the slow firing profile is a very harsh thermal treatment for Al_2O_3 layers.

Figure 4.3(b) shows the effective lifetime after firing using the slow firing profile for different layer systems as a function of PA-ALD Al_2O_3 layer thickness. For PA-ALD Al_2O_3 single-layers ≤ 10 nm only lifetimes below 300 µs are measured, corresponding to S_{eff} values above 45 cm/s. In contrast, PA-ALD Al_2O_3/SiN_x stacks with thin PA-ALD Al_2O_3 layers ≤ 10 nm show effective lifetimes above 1 ms, corresponding to S_{eff} values below 15 cm/s and this even with an only 1 nm thick Al_2O_3 layer. For layers of thickness ≥ 20 nm, there is no significant difference between Al_2O_3 single-layers and Al_2O_3/SiN_x stacks. These samples show a strong blistering after the firing step, especially for the 30 nm thick Al_2O_3 layer. This blistering is mainly a detachment of the SiN_x layer, however, it also might be partly a detachment of the Al_2O_3 layer resulting in no passivation in the areas of the blisters. This results show that the use of a SiN_x capping layer in combination with an ultra-thin Al_2O_3 layer allows the use of higher peak-firing temperatures and even harsher firing profiles compared to the Al_2O_3 single-layer. Hence, a stack of thin Al_2O_3 and SiN_x is best suited for the application to high-efficiency screen-printed solar cells.

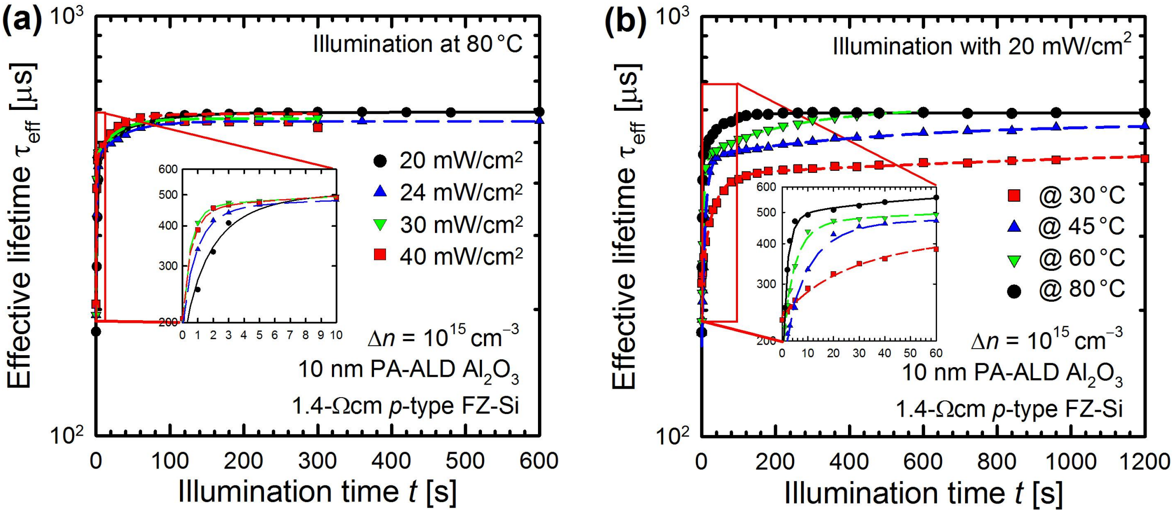

Figure 4.4: Measured effective lifetime τ_{eff} as a function of illumination time for lifetime samples with a 10 nm thick PA-ALD Al_2O_3 layer after firing using the slow firing profile. In (a) the illumination intensity is varied and the sample temperature is kept constant at 80 °C, in (b) the illumination intensity is kept constant at 20 mW/cm^2 and the sample temperature is varied. The lines are fits using Eq. (4.2).

4.2.2 Regeneration of the surface passivation quality

As shown above, the PA-ALD Al_2O_3 single-layers provide only a poor surface passivation quality after a harsh thermal treatment, e.g., our slow firing profile. This reduced passivation quality, however, can partly be recovered by applying an annealing step after the firing [59]. In the following, the impact of annealing and illumination on the degraded lifetime after firing using the slow firing profile is examined. For this investigation, samples with a 10 nm PA-ALD Al_2O_3 single-layer are used. Illumination is performed using a halogen lamp while the samples are placed on a hot-plate. Anneal is carried out on a hot-plate in the dark.

The post-firing anneal at 400 °C improves the effective lifetime for all investigated samples up to ~700 µs after 15 min annealing duration. This corresponds to the optimal annealing parameters for the post-deposition anneal, showing that the post-firing anneal has approximately the same time constant as the post-deposition anneal. During illumination at 30 °C using an intensity of 20 mW/cm^2, the effective lifetime increases for all investigated samples up to 880 µs after 1 hour of illumination. This "regeneration" is influenced by the illumination intensity and the sample temperature.

Figure 4.4(a) shows the measured effective lifetime as a function of illumination time for different illumination intensities at 80 °C. This temperature itself is not sufficient to improve the passivation, samples kept in the dark at 120 °C for 60 min as reference did not show any significant change in lifetime. All illuminated samples show a steep increase in effective lifetime already after 5 seconds of illumination. The measured data can be fitted with a double-exponential fit function:

$$\tau_{\text{eff}} = \tau_0 + \tau_1 \left(1 - e^{-R_1 t}\right) + \tau_2 \left(1 - e^{-R_2 t}\right), \tag{4.2}$$

with τ_0 being the initial lifetime, R_1 the regeneration rate constant of the fast component and R_2 the regeneration rate constant of the slow component. All extracted regeneration rates are summarized in Tab. 4.2.

The initial lifetime after firing is around 200 µs and after illumination for 10 min around 600 µs. The inset in Fig. 4.4(a) shows that the illumination intensity has only an influence during the first 5 seconds. This is attributed to an already high regeneration rate caused by the 80 °C substrate temperature. The inset in Fig. 4.4(a) suggests that the regeneration rate saturates with increasing illumination intensity, but this is probably due to a high measurement uncertainty of the illumination time when illuminating for only 1 second.

Figure 4.4(b) shows the effective lifetime as a function of illumination time for different sample temperatures during illumination. All samples are illuminated with 20 mW/cm^2. The lifetime of the sample at 80 °C saturates after ~10 min, whereas the sample at 30 °C saturates after ~40 min of illumination. The inset in Fig. 4.4(b)) shows that the regeneration rate constant R_1 strongly increases with increasing temperature.

In order to further reduce the illumination time intervals, a photoflash (Quantum

Table 4.2: Regeneration rate constants R_1 and R_2 for different temperatures and illumination intensity for samples with a 10 nm thick PA-ALD Al_2O_3 layer.

Temperature [°C]	Illumination intensity [mW/cm^2]	R_1 [s^{-1}]	R_2 [s^{-1}]
20	$\geq 1\times10^5$	1.081	0.0884
30	20	0.029	0.0005
45	20	0.083	0.0018
60	20	0.171	0.0038
80	20	0.397	0.0173
80	24	0.825	0.0273
80	30	1.556	0.0351
80	40	1.348	0.0386

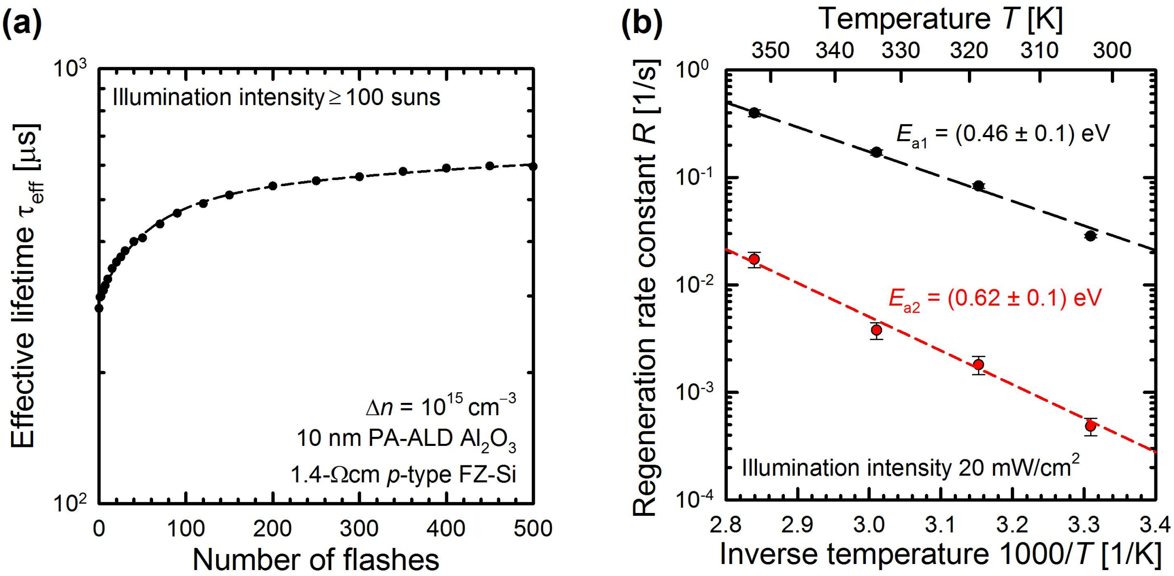

Figure 4.5: (a) Measured effective lifetime τ_{eff} as a function of the number of flashes for a 10 nm thick PA-ALD Al_2O_3 layer after firing using the slow firing profile. The line is a fit using Eq. (4.2). (b) Regeneration rate constants R_1 and R_2 as a function of inverse temperature for a 10 nm thick PA-ALD Al_2O_3 layer illuminated with 20 mW/cm^2.

Qflash X5d-R) was used for illumination. The sample is placed in a distance of 5 cm from the bulb. The total flash duration is 14 ms with an exponential decay in intensity, but the intensity remains above 100 suns during the entire 14 ms of the flash duration.

In Fig. 4.5(a) the measured effective lifetime is plotted as a function of the number of flashes for a sample with a 10 nm thick PA-ALD Al_2O_3 layer. Assuming a flash duration of 14 ms, it is possible to estimate the regeneration rate constants. Both regeneration rate constants are more than 40 times higher than for the sample illuminated at 30 °C with 20 mW/cm^2 and after 6.3 seconds (which corresponds to 450 flashes) of illumination a saturated lifetime of around 600 µs is reached. Therefore, it can be concluded that both regeneration processes can be strongly accelerated by increasing the illumination intensity.

In Fig. 4.5(b) the extracted regeneration rate constants R_1 and R_2 are shown as a function of inverse temperature. It is obvious that both regeneration rates follow an Arrhenius law, hence, the activation energies for both regeneration processes are extracted with $E_{a1} = (0.46\pm0.1)$ eV and $E_{a2} = (0.62\pm0.1)$ eV at an illumination intensity of 20 mW/cm^2.

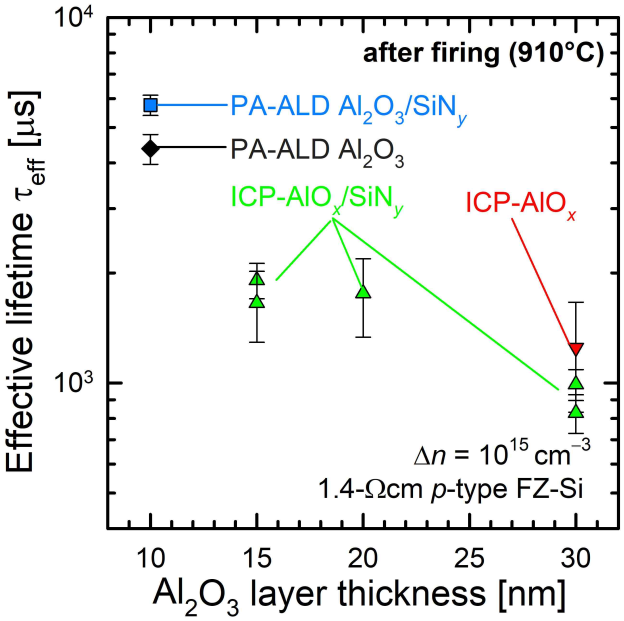

Figure 4.6: Effective lifetime τ_{eff} for 10 nm thick PA-ALD Al_2O_3 as single-layer (diamond) and in an Al_2O_3/SiN_y stack (square), also shown are ICP-AlO_x layers of various thicknesses in an Al_2O_3/SiN_y stack (triangle up) and a 30 nm ICP-AlO_x single-layer (triangle down) after firing using the fast firing profile. The samples are measured at 9 locations on the samples using the PCD method and shown are the mean value and the standard deviation.

4.3 ICP-PECVD AlO_x layers

4.3.1 Firing of ICP-PECVD AlO_x layers

In this Section, the behavior of the surface passivation provided by ICP-AlO_x layers is investigated using only the fast firing profile with a set-peak temperature of 910 °C. This firing profile represents best the firing conditions of industrial screen-printed solar cells. For the AlO_x/SiN_y stacks, a 100 nm thick SiN_y is used.

Figure 4.6 shows the effective lifetime τ_{eff} after firing for 12.5×12.5 cm^2 1.4-Ωcm p-type FZ-Si samples passivated with ICP-AlO_x in comparison with samples passivated with PA-ALD Al_2O_3. For the 30 nm thick ICP-AlO_x layer almost no difference between the samples with and without SiN_y capping layer is observed. Both layer systems provide an effective lifetime of ∼1 ms after firing, corresponding to an S_{eff} value below 18 cm/s. The ICP-AlO_x/SiN_y stacks with 15 and 20 nm AlO_x layers provide lifetimes between 1 and 2 ms, corresponding to an S_{eff} value below 10 cm/s. The ICP-AlO_x layers provide a very good surface passivation quality after firing, however, the PA-ALD Al_2O_3 layers provide S_{eff} values below 2 cm/s. This difference in passivation quality between the ICP-AlO_x/SiN_y stacks and the PA-ALD Al_2O_3/SiN_y stack is partly due to

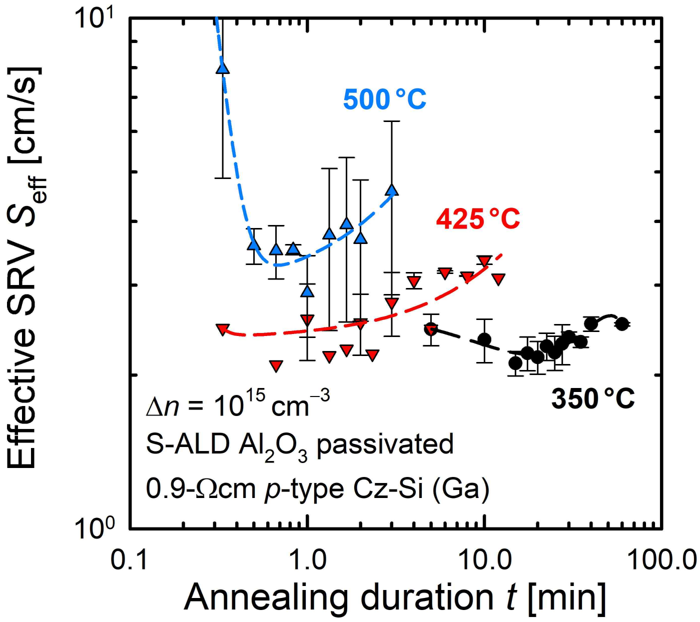

Figure 4.7: Effective SRV S_{eff} extracted from PCD measurements as a function of annealing duration for different annealing temperatures. The S-ALD Al_2O_3 layers are deposited on 0.9-Ωcm Ga-doped p-type Cz-Si. The lines are guides to the eye.

a slight blistering of the ICP-AlO_x/SiN_y stack during the firing process. This blistering is mainly observed at samples with a 30 nm thick ICP-AlO_x layer in an Al_2O_3/SiN_y stack, but for samples with a 15 or 20 nm thick ICP-AlO_x layer in an Al_2O_3/SiN_y stack also a few blister can be observed as well.

4.4 S-ALD Al_2O_3 layers

4.4.1 Impact of annealing temperature on passivation quality

Figure 4.7 shows S_{eff} values extracted from PCD measurements as a function of the annealing duration for different annealing temperatures for 0.9-Ωcm Ga-doped p-type Cz-Si samples passivated with 15 nm S-ALD Al_2O_3. It can be seen, that already an annealing temperature of 350 °C is sufficient to activate the excellent surface passivation. At higher temperature, the optimal time is reduced down to 1 minute for 500 °C, which correspondences to an S_{eff} below 3 cm/s. Annealing the samples further reduces the surface passivation quality, a behavior which is already known from PA-ALD Al_2O_3 layers, however, not as pronounced.

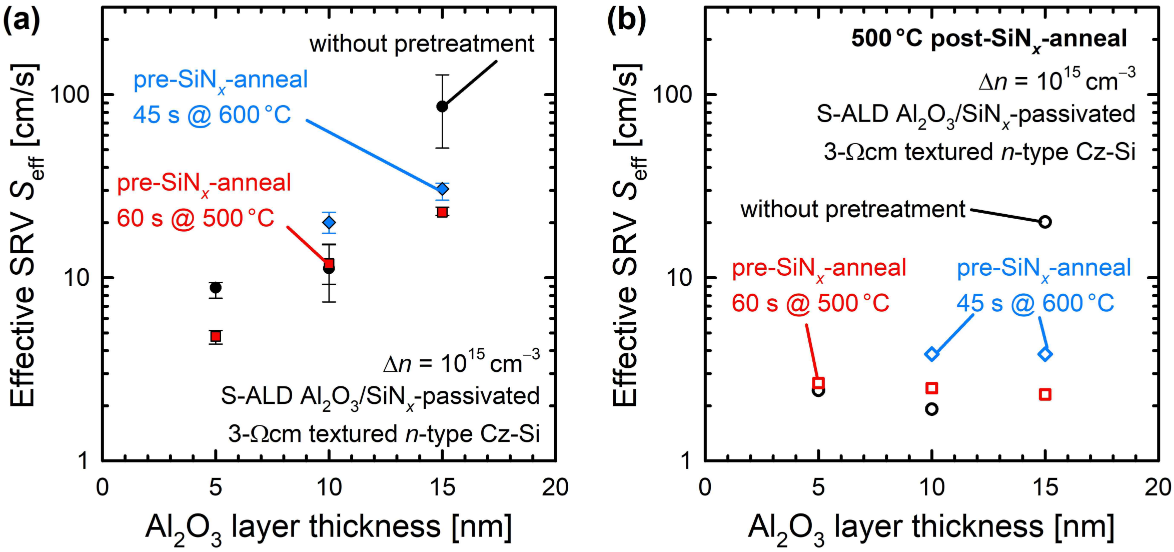

Figure 4.8: Effective SRV S_{eff} as a function of S-ALD Al_2O_3 layer thickness for 3-Ωcm textured n-type Cz-Si samples passivated with S-ALD Al_2O_3/SiN_x stacks. The samples received different thermal treatments prior to the SiN_x deposition. In (a) measured directly after the SiN_x deposition and in (b) measured after a post-SiN_x-deposition-anneal at 500 °C.

4.4.2 S-ALD Al_2O_3/SiN_x stacks

As noted above, the deposition of a SiN_x layer partly serves as an annealing step, however, the deposition time and temperature normally deviate from the optimal annealing temperature and duration. In the following, this will be exemplarily shown for S-ALD Al_2O_3 layers on 3-Ωcm textured n-type Cz-Si samples. This type of sample is especially relevant for high-efficiency interdigitated back contacted (IBC) solar cells. For this type of solar cell, most commonly n-type silicon is used as base material and an excellent passivation of the front side is very important to achieve high efficiencies.

For the surface passivation different Al_2O_3 layer thicknesses are used. Before the SiN_x deposition, the samples are split into three groups. Group (1) receives no thermal treatment, group (2) receives a pre-SiN_x-deposition-anneal at 500 °C for 60 s, and group (3) receives a pre-SiN_x-deposition-anneal at 600 °C for 45 s. Figure 4.8(a) shows the S_{eff} values after the SiN_x deposition. The lowest S_{eff} values are measured for the 5 nm thick S-ALD Al_2O_3 layer and the highest for the 15 nm thick S-ALD Al_2O_3 layer, in contrast to the single-layers, see Fig. 4.1. A pre-SiN_x-deposition-anneal has no major impact on this trend, however, the lowest S_{eff} of 5 cm/s is in fact reached with a 5 nm thick S-ALD Al_2O_3 layer and a 500 °C pre-SiN_x-deposition-anneal.

After the SiN_x deposition the samples are laser-cut into 4 pieces with the size of 7.8×7.8 cm^2. This size was chosen as trade-off between minimizing the influence of

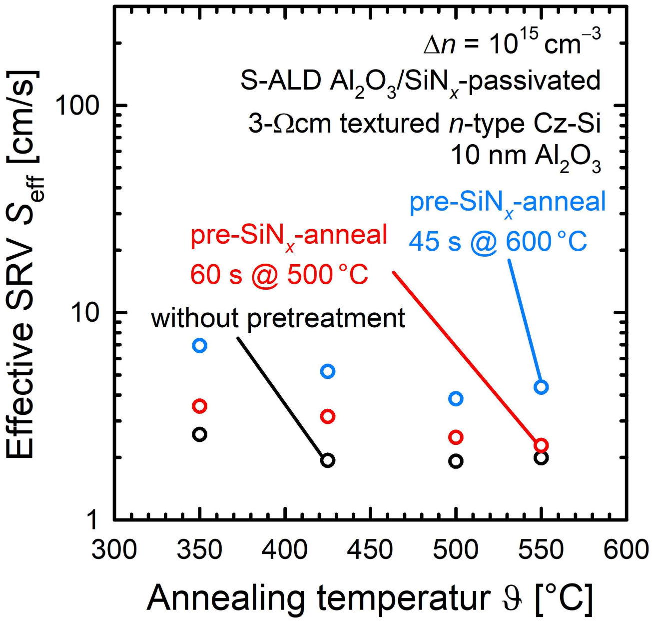

Figure 4.9: Effective SRV S_{eff} as a function of annealing temperature after SiN_x deposition for 3-Ωcm textured n-type Cz-Si samples passivated with S-ALD Al_2O_3/SiN_x stacks. The samples received different thermal treatments prior to the SiN_x deposition.

the edge and having several identical samples for further investigations. As can be seen in Chapter 5, the edge reduces the lifetime for this sample size below an excess carrier concentration of $\Delta n = 10^{14}$ cm^{-3}, however, any scratches on the sample surface will reduce the lifetime, and hence, the S_{eff} values in the following represent an upper limit. The samples receive a post-SiN_x-deposition-anneal at 350, 425, or 500 °C. The samples are successively annealed and measured. In Fig. 4.8(b) the best results for the 500 °C anneal are shown. For all samples an improvement is reached resulting in S_{eff} values below 3 cm/s. The annealing step prior to the SiN_x deposition, however, does not seem to have a major influence. Only the sample with a 15 nm thick S-ALD Al_2O_3 layer without a pre-SiN_x-deposition-anneal shows a poor passivation quality. The annealing temperature does not have a major impact on the surface passivation quality. In Fig. 4.9, this is exemplarily shown for samples passivated with a 10 nm thick S-ALD Al_2O_3 layer. The evolution of the surface passivation quality over the annealing duration is for all annealing temperatures similar, all samples show already after an annealing duration of 1 min a very good surface passivation quality. This very good surface passivation quality is stable, within the measurement uncertainty, for an annealing duration of several minutes. Most samples show after an annealing duration of more than 3 min a slight degradation of the surface passivation quality, however, this might be due to scratches induced by the repeated measurements.

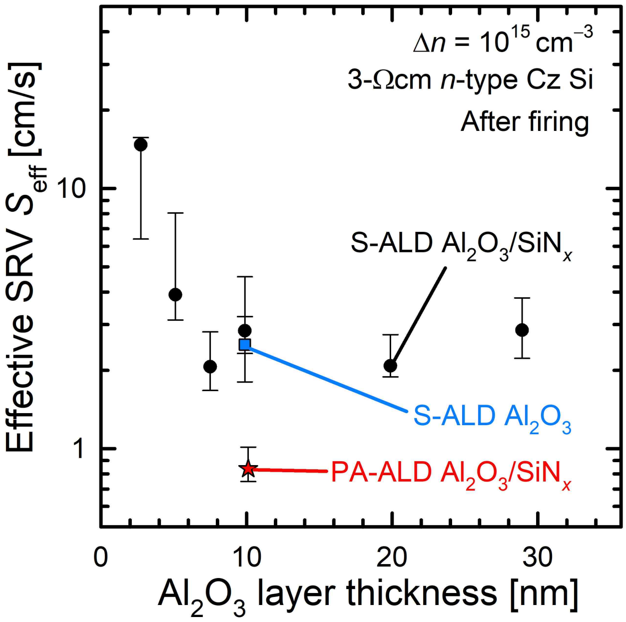

Figure 4.10: Effective SRV S_{eff} after firing using the fast firing profile as a function of Al_2O_3 layer thickness for 3-Ωcm planar n-type Cz-Si samples passivated with S-ALD Al_2O_3/SiN_x stacks. Also shown are the results for a sample passivated with a 10 nm thick S-ALD Al_2O_3 single-layer and PA-ALD Al_2O_3/SiN_x stack.

4.4.3 Firing of S-ALD Al_2O_3 layers

The surface passivation quality after firing provided by the S-ALD Al_2O_3 layers is almost as good as that of the PA-ALD Al_2O_3 layers. In Fig. 4.10, this can be seen for 3-Ωcm planar n-type Cz-Si samples passivated either with an S-ALD Al_2O_3 single-layer, S-ALD Al_2O_3/SiN_x stacks, or PA-ALD Al_2O_3/SiN_x stacks. For all stacks, a 100 nm thick SiN_x layer is used. All samples are fired using the fast firing profile and a set-peak temperature of 910 °C. For S-ALD Al_2O_3 layers with a thickness ≥ 8 nm the surface passivation quality is independent of the S-ALD Al_2O_3 layer thickness with S_{eff} values below 5 cm/s. However, as also observed for the ICP-AlO_x and also thick PA-ALD Al_2O_3 layers, the samples passivated with thick S-ALD Al_2O_3 layers show a strong blistering effect. This blistering is observed on all samples passivated with S-ALD Al_2O_3, however, the blister size and density increases with increasing S-ALD Al_2O_3 layer thickness. Starting with a few small blisters (diameter < 2 µm) for 2.5 nm thick S-ALD Al_2O_3 layer, see Fig. 4.11(a), to more and also larger blisters (diameter > 6 µm) for thick S-ALD Al_2O_3 layers > 20 nm, see Fig. 4.11(b). In general, the passivation is not affected by the blistering, however, when applying the passivation layers to solar cells, the blisters can have a negative influence. For the rear side of solar cells the blisters can lead to local contacts between the metal and the silicon without a

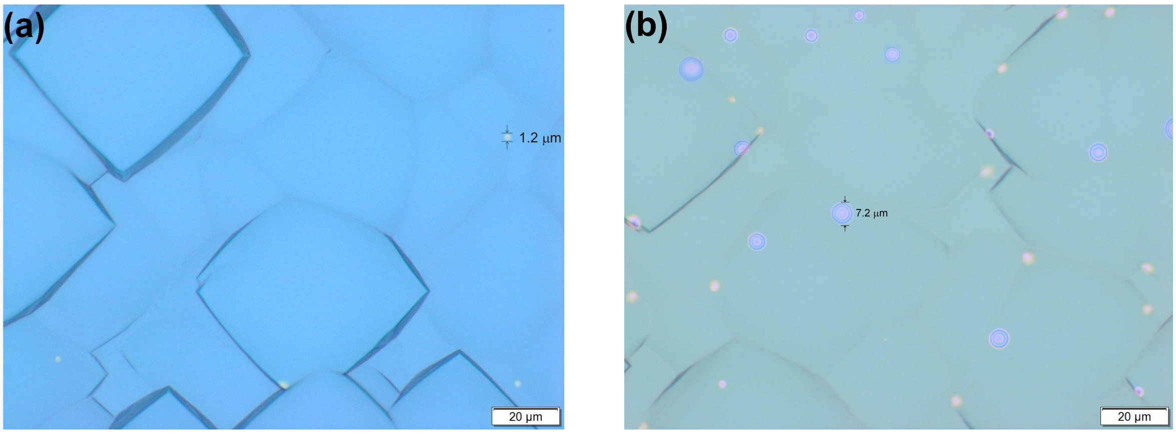

Figure 4.11: Light microscop images of silicon samples passivated with a S-ALD Al_2O_3/SiN_x stack after firing using the fast profile. In (a) with a 2.5 nm thick S-ALD Al_2O_3 layer and in (b) with a 20 nm thick S-ALD Al_2O_3 layer.

passivating back surface field and for the front side the optics are changed and might reduce the short-circuit current density J_{sc}. Therefore, it is important not only to account for the surface passivation, but also take blistering effects into account.

In the case of S-ALD Al_2O_3, the blistering can, to some extent, be reduced by reducing the water dose during the S-ALD Al_2O_3 deposition. Gay et al. [60] also reported that an annealing step prior to the SiN_x deposition can reduce the blistering strongly and that this annealing step can be included in the SiN_x deposition process. In the case of the two tools used for SiN_x deposition in this work, the samples are annealed inside the tools prior to the SiN_x deposition. Therefore, an additional annealing step prior to the SiN_x deposition is not beneficial. For samples that received such an extra annealing step, a reduced blistering was observed, but also the passivation was strongly reduced.

4.5 Chapter summary

In this Chapter it was shown that regardless of the deposition technique, low-temperature-annealed Al_2O_3 can provide an excellent surface passivation quality. S_{eff} values below 2 cm/s for PA-ALD and S-ALD Al_2O_3 and below 6 cm/s for ICP-AlO_x on 1.4-Ωcm p-type FZ-Si were achieved. The Q_{f} for all applied deposition techniques was found to be $-(4\pm1)\times10^{12}$ cm^{-2}, whereas a larger interface state density D_{it} was found for the ICP-AlO_x explaining the slightly higher S_{eff} values. With D_{it} values of $(5\pm1)\times10^{11}$ eV^{-1}cm^{-2} around midgap for a 30 nm thick ICP-AlO_x in comparison to a

D_{it} of $(1\pm0.4)\times10^{11}$ eV^{-1} for a 30 nm thick PA-ALD Al_2O_3 layer.

It was further shown that the Al_2O_3 layer subject to a firing step using the fast firing profile can also provide an excellent surface passivation quality, especially in conjunction with a SiN_x capping layer. For PA-ALD Al_2O_3/SiN_x stacks S_{eff} values of 1 cm/s were measured on 1.4-Ωcm *p*-type FZ-Si and 3-Ωcm *n*-type Cz-Si, whereas S-ALD Al_2O_3/SiN_x stacks provided a slightly lower surface passivation quality with S_{eff} values between 2 and 3 cm/s measured on 3-Ωcm *n*-type Cz-Si and the ICP-AlO_x/SiN_y stacks below 10 cm/s on 1.4-Ωcm *p*-type FZ-Si. The addition of a SiN_x layer as capping layer for the Al_2O_3 was found to have a strong impact on the surface passivation quality for very thin PA-ALD Al_2O_3 layers ($\leq$ 10 nm) that were subject to a harsh firing using the slow firing profil. The very thin PA-ALD Al_2O_3 layers show a reduced passivation quality after the harsh firing, whereas the PA-ALD Al_2O_3/SiN_x stacks still provide an excellent passivation quality. The reduced passivation quality of the PA-ALD Al_2O_3 single-layers, however, can partly be recovered by applying a post-firing anneal (425 °C for 15 min) or by illumination.

The surface passivation quality of low-temperature annealed S-ALD Al_2O_3/SiN_x stacks was optimized on textured 3-Ωcm *n*-type Cz-Si samples. An annealing step prior to the SiN_x deposition was found to have no major impact on the surface passivation quality, still the lowest S_{eff} value of 5 cm/s was measured for a 5 nm thick Al_2O_3 layer with a 500 °C pre-SiN_x-deposition-anneal. A post-SiN_x-deposition-anneal, in contrast, has a major impact. Samples that were subject to a 500 °C post-SiN_x-deposition-anneal showed an increase in the surface passivation quality to S_{eff} values below 3 cm/s. The surface passivation quality was almost independently on the thermal treatment prior to the SiN_x deposition as well as on the S-ALD Al_2O_3 layer thickness. Hence, in order to achieve an excellent surface passivation quality a supplementary post-SiN_x-deposition-anneal is necessary.

Chapter 5

N-type c-Si passivated with Al_2O_3

In Section 2.2.3, it was already mentioned that even if the passivation of n-type silicon with Al_2O_3 itself is very good, the effective lifetime shows a pronounced injection dependence at low excess carrier concentrations (typically at $\Delta n < 10^{14}$ cm^{-3}) [7]. As discussed in Section 2.2.3, different explanation have been proposed for this injection dependence. In this Chapter, we will focus on our proposed model which assigns the pronounced $S_{\mathrm{eff}}(\Delta n)$ dependence to recombination at the wafer edge. We perform experiments and two-dimensional simulations using Sentaurus Device [38] in order to verify our model.

5.1 Experimental details

All lifetime test samples in this Chapter are fabricated on p-type FZ-Si and n-type Cz-Si wafers with a resistivity between 1.2 and 1.4 Ωcm. The samples are laser-cut into 12.5×12.5 cm^2 pseudo-square, 6×6 cm^2, 4×4 cm^2, and 2.5×2.5 cm^2 full-square samples. Half of the 12.5×12.5 cm^2 pseudo-square and all small samples are KOH-etched in order to remove the laser damage and all samples are subsequently RCA-cleaned. On both sides of the samples, a 15 nm thick Al_2O_3 layer is deposited using PA-ALD. After Al_2O_3 deposition the samples are annealed at 425 °C for 15 min in order to activate the Al_2O_3 passivation. The samples are characterized using the PCD method, however, this method shows a measurement artifact under low excess carrier concentration due to the depletion region modulation (DRM) effect [53]. In order to exclude DRM and retrieve trustable information (including spatial information) about the low-injection lifetime, PC-PLI measurements were performed on selected samples. After measurement of the effective lifetime some of the 12.5×12.5 cm^2 pseudo-square samples are successively laser

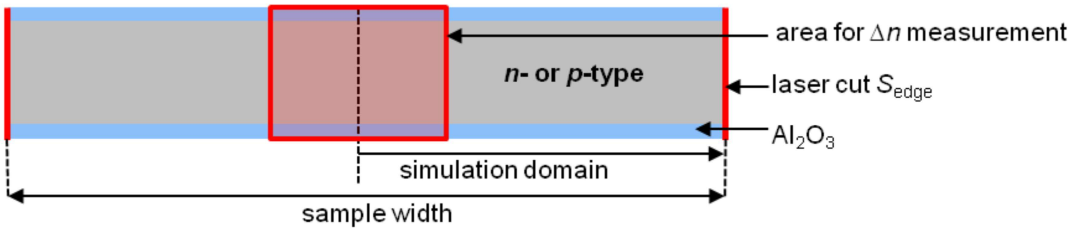

Figure 5.1: Sentauraus Device simulation domain for PC-PLI lifetime simulations. The red area in the middle of the sample represents the area for the extraction of the PC-PLI lifetime.

cut into circular samples with diameter of 12.5, 8, 6, and 4 cm and measured again using the PC-PLI method. In order to model the influence of the edge recombination, two-dimensional simulations of the PC-PLI measurements were performed with Sentaurus Device [38] using model parameters described by Altermatt [61]. A detailed description of the simulation environment can be found in Ref. 62. The simulation domain of the Sentaurus Device simulations is shown in Fig. 5.1. The excess carrier concentration Δn is determined in a 2 cm wide area in the middle of the sample, which represents the sensing area of the coil in the lifetime tester and the area used in the PC-PLI setup for averaging. For the Sentaurus Device simulations the energy-dependent interface state density $D_{\mathrm{it}}(E)$ is approximated by a single interface state density N_{it} at an energy level E_{t} located in the middle of the silicon bandgap. With this assumption Eq. (2.13) can be rewritten as

$$U_{\mathrm{it}} = \frac{n_{\mathrm{s}}p_{\mathrm{s}} - n_{\mathrm{i}}^2}{S_p^{-1}(n_{\mathrm{s}} + n_1(E_{\mathrm{t}})) + S_n^{-1}(p_{\mathrm{s}} + p_1(E_{\mathrm{t}}))}, \tag{5.1}$$

with the SRV parameters for holes S_p and electrons S_n which are given by

$$S_p = \sigma_p v_{\mathrm{th}} N_{\mathrm{it}}, \tag{5.2}$$

$$S_n = \sigma_n v_{\mathrm{th}} N_{\mathrm{it}}. \tag{5.3}$$

S_n and S_p are used as input parameters for the Sentaurus Device simulations.

5.2 Sample size dependence of the effective lifetime

Commonly, small samples (typically 2.5×2.5 cm^2) are used for the evaluation of the passivation quality. Therefore, it is of great importance to understand the influence of the sample size on the measured lifetime, especially for n-type silicon samples passivated with Al_2O_3.

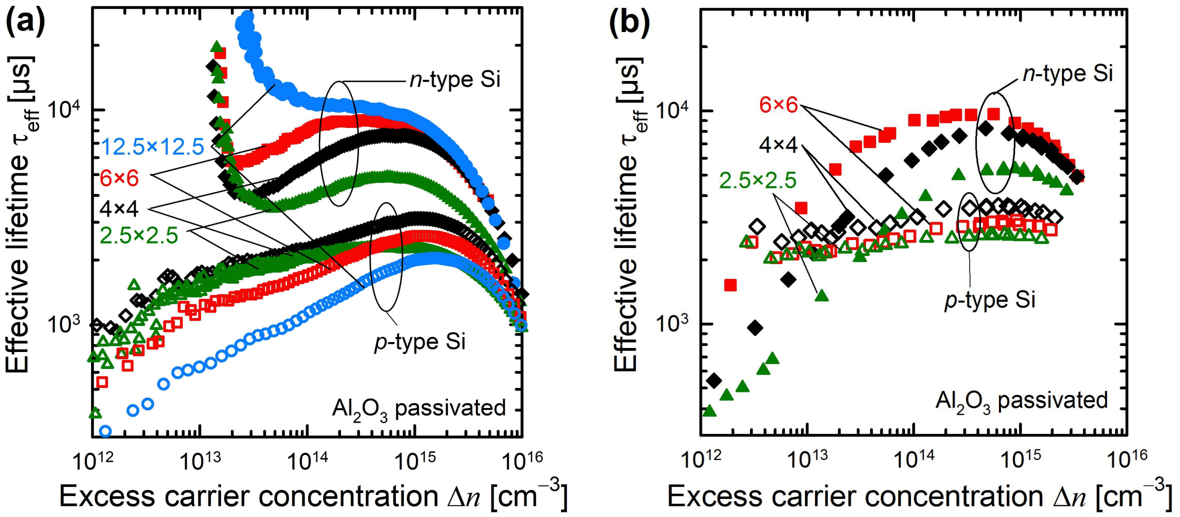

Figure 5.2: Effective lifetime τ_{eff} as a function of excess carrier concentration Δn of Al_2O_3-passivated 1.2-Ωcm n-type Cz-Si and 1.4-Ωcm p-type FZ-Si wafers of different sample sizes. All samples received a KOH-etch prior to the Al_2O_3 passivation. In (a) PCD measurements and in (b) PC-PLI measurements are shown.

Figure 5.2(a) shows the effective lifetime τ_{eff} measured using PCD as a function of the excess carrier concentration Δn. It can be seen that some of the Al_2O_3-passivated n-type Cz-Si samples show a pronounced injection dependence of effective lifetime. The 12.5×12.5 cm^2 sample shows only a negligible dependence on Δn, whereas the 4×4 cm^2 sample shows the most pronounced Δn dependence. More importantly, the smaller the sample the lower the effective lifetime at an excess carrier concentration of $\Delta n = 10^{14}$ cm^{-3}. For the 2.5×2.5 cm^2 sample even the overall lifetime is reduced, which can partly be attributed to a measurement artifact, as the sample might be smaller than the sensing area of the WCT-120. However, due to the DRM effect no information about the injection dependence can be extracted for injection densities below $\Delta n = 10^{14}$ cm^{-3}. The lifetimes of the p-type FZ-Si samples also show some injection dependence, however, no pronounced impact on the sample size is observed. To obtain more information on the spatial distribution of the effective lifetime and the behavior in the low-injection range, some of the samples were additionally measured using the PC-PLI method.

Figure 5.2(b) shows the effective lifetime τ_{eff} of the samples extracted from PC-PLI measurements as a function of excess carrier concentration Δn. Shown are area-averaged lifetimes, with the area size chosen to fit the approximate detection region of the PCD measurement in Fig. 5.2(a). The effective lifetime of the n-type samples is - with exception of the 2.5×2.5 cm^2 sample - the same as measured with PCD, except

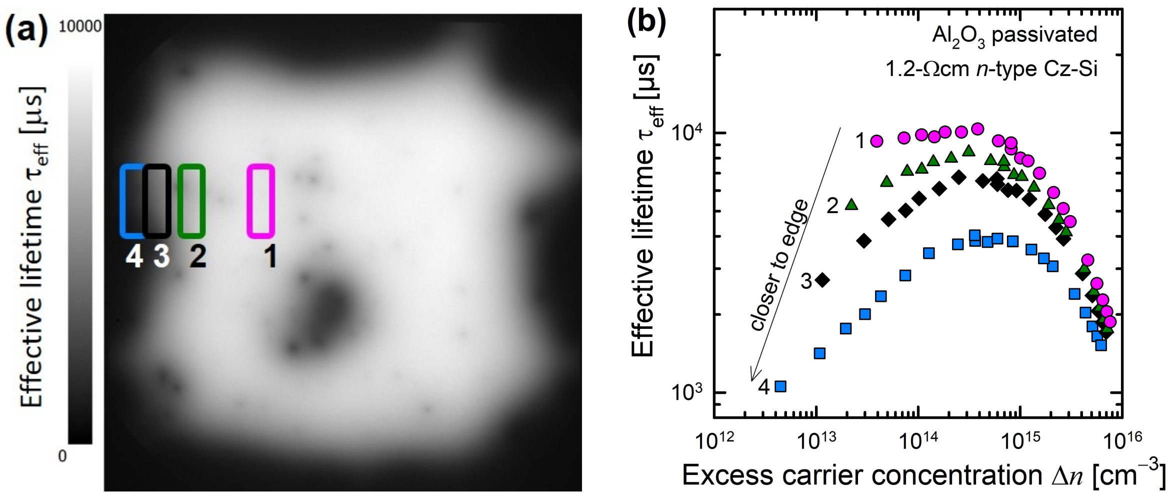

Figure 5.3: (a) PC-PL image of a 12.5×12.5 cm^2 Al_2O_3-passivated 1.2-Ωcm n-type Si sample. The sample received a KOH-etch prior to the passivation. The excess carrier concentration is between 2×10^{12} and 4×10^{13} cm^{-3}. (b) Extracted effective lifetime τ_{eff} as a function of excess carrier concentration. The lifetimes are averaged over the marked areas in (a).

that no DRM effect is observed. The PC-PLI measurements show a significant injection dependence for the 2.5×2.5 cm^2 sample, leading to a pronounced $\tau_{\text{eff}}(\Delta n)$ dependence for all three samples at an excess carrier concentration Δn below 3×10^{13} cm^{-3}. The effective lifetimes of the p-type samples show almost no injection dependence in the PC-PLI measurements. In conclusion, the PC-PLI data exhibit a strong difference between the injection dependence of p- and n-type samples. On p-type silicon, the lifetimes change only by a factor of 2 over a wide injection range, whereas the lifetimes of the n-type silicon samples change by one order of magnitude over the measured injection range. This injection dependence is almost independent on the sample size, but the measured effective lifetime below an excess carrier concentration of $\Delta n = 10^{14}$ cm^{-3} strongly depends on the sample size. This is especially interesting since all samples received a KOH-etch prior to the passivation. The applied KOH-etch, however, is apparently not sufficient for the removal of the damage induced by the laser during the cutting process.

Figure 5.3(a) shows a PC-PL image of a 12.5×12.5 cm^2 Al_2O_3-passivated n-type Cz-Si sample. In the center of the sample, the lifetime is around 10 ms, with the exception of a spot which probably results from a mechanical damage or contamination due to handling. Closer to the edge the lifetime strongly decreases. This can be seen quantitatively in Fig. 5.3(b), where the lifetimes as a function of excess carrier concentration for the marked regions in Fig. 5.3(a) are shown. The lifetime close to the

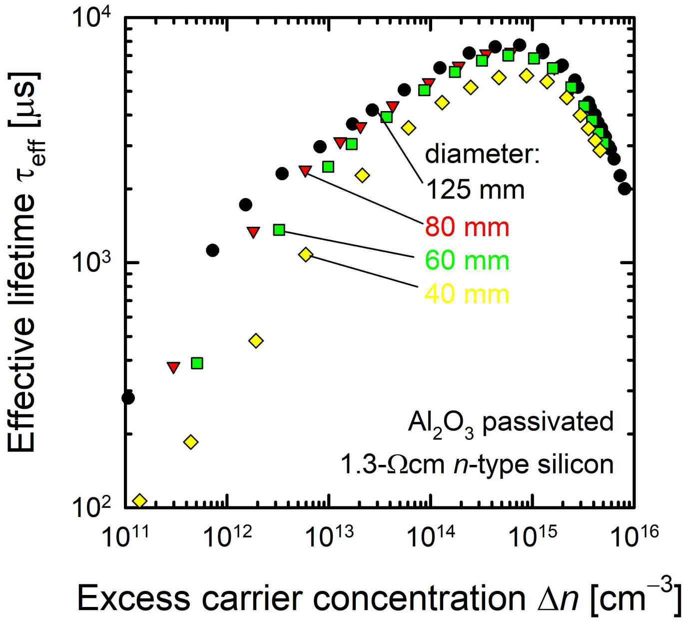

Figure 5.4: Area averaged effective lifetime τ_{eff} as a function of excess carrier concentration Δn measured using PC-PLI. Shown are the results for a 1.3-Ωcm n-type Cz-Si sample that is successively laser cut into smaller disks. The lifetime is extracted in the center of the sample on a disk with a diameter of 2 cm.

center of the wafer shows negligible injection dependence, whereas closer to the edge the lifetime decreases and becomes significantly more injection dependent.

Figure 5.4 shows the effective lifetime τ_{eff} of a 1.3-Ωcm n-type Cz-Si sample which has been successively laser-cut into smaller disks. The injection-dependent lifetime can be separated into two regions. (i) At moderate injection densities ($\Delta n \sim 10^{14}$ cm^{-3}), the injection dependence is for all sample sizes the same. The origin of this injection dependence will be discussed in more detail in Section 5.3.3. (ii) At low injection densities the lifetime strongly decreases. The beginning of this strong decrease, however, is shifted to higher injection densities for smaller samples. We attribute the origin of this strong decrease to the recombination at the sample edge.

Our experimental findings strongly suggest that the sample edge has a significant impact on the injection dependence of the effective lifetime. Importantly, the effective lifetime is not only reduced at the edge itself, but also up to several cm into the sample. This results not only in different injection dependences for samples of different sizes, but can also reduce the overall lifetime, as observed on the 2.5×2.5 cm^2 sample. Furthermore, regions of reduced lifetime on the wafer surface, e.g., the spot seen in Fig. 5.3(a), can reduce the overall effective lifetime as well.

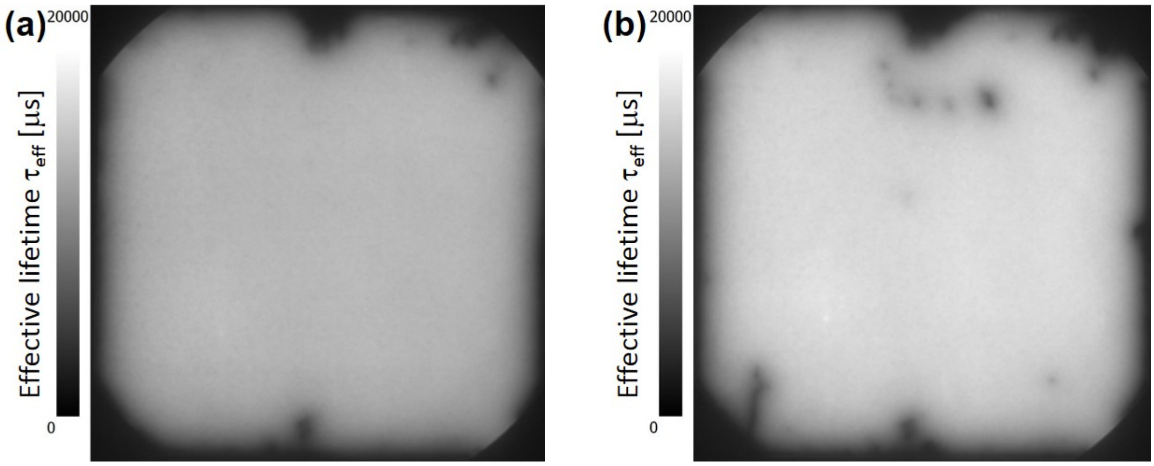

Figure 5.5: PC-PL images (a) after processing and (b) after a series of measurements, of the same $12.5{\times}12.5$ cm^2 Al_2O_3-passivated 1.4-Ωcm *n*-type Cz-Si sample. The sample received a KOH-etch prior to the passivation. The excess carrier concentrations in both images are between $6{\times}10^{14}$ cm^{-3} and $2{\times}10^{15}$ cm^{-3}.

5.3 Homogeneous surface passivation of large *n*-type c-Si samples

In the previous Section, the importance of the sample size for the effective lifetime measured on *n*-type silicon passivated with Al_2O_3 was shown. In this Section, the influence of a homogeneous passivation on the measured lifetime will be discussed. This is especially important for the measurement of the bulk lifetime of a sample. The importance of the homogeneous passivation is evaluated on large ($12.5{\times}12.5$ cm^2) *n*-type Cz-Si samples with a resistivity of 1.2-1.4 Ωcm and a thickness of 600 µm. These samples are thicker than the samples used in the previous Section, which leads for the same SRV to a higher effective lifetime, see Eq. (2.30). These samples are, therefore, better suited for bulk lifetime investigations.

5.3.1 Experimental results

The sample with the most homogeneous passivation and the highest lifetime is shown in Fig. 5.5(a). The sample is a 1.4-Ωcm *n*-type Cz-Si sample that received a KOH-etch. In general, all samples that received a KOH-etch prior to the RCA cleaning show less areas of reduced lifetime, all samples without the KOH-etch show four areas of reduced lifetimes, one in each corner (see the inset in Fig. 5.7(a)). During the laser cutting procedure the samples are placed on four pins and the positions of these pins

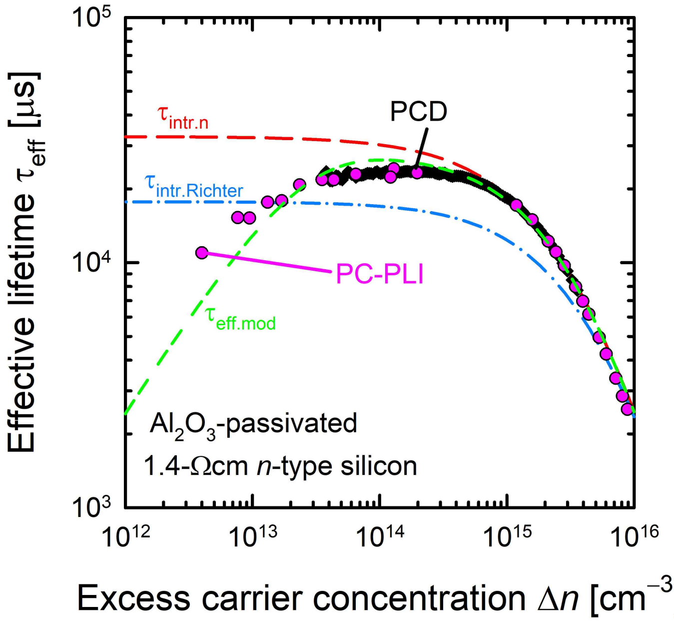

Figure 5.6: Effective lifetime τ_{eff} as a function of excess carrier concentration Δn for a 1.4-Ωcm n-type Cz-Si sample passivated with 15 nm Al_2O_3. Also shown is the intrinsic lifetime $\tau_{\mathrm{intr.Richter}}$ (Eq. (2.10)) [6] (dash-dotted line). The intrinsic lifetime $\tau_{\mathrm{intr.n}}$ using our new parameterization in Eq. (5.5) and the simulated lifetime using the new parameterization, are shown as single and double dashed lines, respectively.

correspond to the position of the areas of reduced lifetime. This underlines how carefully one has to be during processing, in order to avoid any areas of reduced lifetime. The RCA-clean is not sufficient to remove the damages introduced before, however, since the pins are placed at the corners the influence on the measurement in the center can be neglected. Not only any damages introduced before the passivation have a negative effect on the homogeneous passivation, but also any handling after the passivation can produce areas of reduced lifetime. Figure 5.5(b) shows the same sample as shown in Fig. 5.5(a) after a series of measurements. Extreme caution was given to the handling, but small scratches could not be avoided. A possible solution for this is the capping with SiN_x after the Al_2O_3 passivation, however, the deposition of SiN_x can also introduce surface damages due to flakes during deposition or handling.

All samples show a reduced lifetime for lower injection densities $\Delta n < 10^{14}$ cm^{-3} especially close to the edges. As discussed in the previous Section, this is related to edge recombination. The highest lifetime is measured on the 1.4-Ωcm n-type Cz-Si sample shown in Fig. 5.5(a). This sample shows a maximal lifetime of 24.1 ms (at $\Delta n = 1.3\times10^{14}$ cm^{-3}) measured using PC-PLI and 23.7 ms (at $\Delta n = 1.9\times10^{14}$ cm^{-3}) measured using PCD, see Fig. 5.6. This lifetime is to our knowledge hitherto the highest reported lifetime for crystalline n-type silicon with a resistivity of around 1 Ωcm and well above the commonly used intrinsic lifetime $\tau_{\text{intr.Richter}}$ (Eq. (2.10)) [6], which is 17 ms (at $\Delta n = 1\times10^{14}$ cm^{-3}). Therefore, an adapted parameterization of the intrinsic lifetime for n-type c-Si seems to be necessary. This is also supported by publications of Wan et al. [63] and Niewelt et al. [64] who measured lifetimes exceeding the intrinsic lifetime $\tau_{\text{intr.Richter}}$ by Richter et al. [6] on n-type FZ-Si.

5.3.2 New parameterization of the intrinsic lifetime of n-type c-Si

The parameterization of the Auger recombination has changed several times over the past decades, as already discussed in Section 2.1.2. Recently, the most widely used parameterization was developed by Richter et al. [6]. This parameterization is based on lifetime measurement on small-area n- and p-type samples passivated with Al_2O_3. Since for n-type silicon samples passivated with Al_2O_3, the sample size has a significant impact on the measured lifetime, as we have demonstrated in the previous Section, the parameterization of Richter et al. is not valid on 1-2 Ωcm n-type silicon, as can be concluded from our measurements presented in this thesis. Therefore, a new parameterization for 1-2 Ωcm n-type silicon will be derived in the following.

We start with Eq. (2.6), include the radiative recombination and set C_p to zero, since our new parameterization is only valid for n-type silicon:

$$\tau_{\text{intr.n}} = \frac{\Delta n}{(np - n_{\text{i}}^2)(g_{eeh}C_n n_0 + g_{\Delta n}C_a\Delta n + B_{\text{rel}}B_{\text{low}})}. \tag{5.4}$$

We further simplify the equation by neglecting n_{i}^2, since $np >> n_{\text{i}}^2$ in most practical cases. Following the approach of Kerr et al. [24], we further assume $B_{\text{rel}} = 1$. This can be done since all information about the change in the radiative recombination coefficient can also be included in the empirical enhancement factors g_{eeh} and $g_{\Delta n}$. The applicability of Richter's parameterization is assumed to be still valid for high doping concentrations ($N_{\text{dop}} > 10^{18}$ cm^{-3}) and also for high excess carrier concentrations ($\Delta n > 10^{16}$ cm^{-3}). This can be done because Richter et al. [6] used only for the parameterization at low doping concentration n-type silicon passivated with Al_2O_3, for the parametrization of the high doping concentrations they used literature data [18, 65, 66] that were not affected by edge recombination. For high excess carrier concentrations the lifetime is also not influenced by the recombination at the wafer edges. Therefore, our new parameterization is restricted to deviate in the high doping range less than

20% and for excess carrier concentrations Δn between 10^{16} and 10^{17} cm^{-3} less than 10% from the Richter lifetime $\tau_{\mathrm{intr.Richter}}$.

In order to approach the actual bulk lifetime as close as possible, the knowledge of the surface recombination velocity would be required. However, since the passivation of n-type silicon with Al_2O_3 leads to extremely low SRVs, which are very difficult to determine experimentally, we neglect the SRV and use instead the approximation that the bulk lifetime equals the measured effective lifetime. Simulations using Sentaurus Device with the model described above show that if assuming completely negligible surface recombination, the lifetime below $\Delta n = 10^{15}$ cm^{-3} is reduced due to the edge recombination effect. Therefore, only the measured lifetimes at $\Delta n > 10^{15}$ cm^{-3} are taken into account and after a least-square fit-to the measured data, the following parameterization is obtained ($\tau_{\mathrm{intr.n}}$ in seconds and concentrations in cm^{-3})

$$\tau_{\mathrm{intr.n}} = \frac{\Delta n}{np(2.1\times10^{-27}n_0^{0.79} + 7.7\times10^{-28}\Delta n^{0.84} + B_{\mathrm{low}})}. \tag{5.5}$$

Note that since we neglect the surface recombination, the true intrinsic lifetime must be even higher.

To verify this new parameterization, it is implemented into the Sentaurus Device model. A fixed charge density of $Q_{\mathrm{f}} = -4\times10^{12}$ cm^{-2} is assumed, the SRV parameters S_n and S_p are set at zero, and the recombination at the edge is set at $S_{\mathrm{n.edge}} = S_{\mathrm{p.edge}} = 10^7$ cm/s. The simulation results show that the new parameterization is in excellent agreement with our measured data, as can be seen in Fig. 5.6.

5.3.3 Influence of non-homogeneous passivation

Figure 5.7(a) shows the injection-dependent lifetimes of two 1.3-Ωcm n-type Cz-Si samples passivated with 15 nm Al_2O_3. Both samples have the same intrinsic bulk lifetime and passivation, however, the injection-dependent lifetime are quite different. This can be explained by the area of low lifetime close to the center, marked with an arrow. Sentaurus Device simulations are used to verify this hypotheses. In order to account for the area of reduced lifetime we implement on the front side a 1 µm wide area of reduced passivation with a Q_{f} of 0. The SRV parameter S_n of this region is varied, S_p is set equal S_n, and the position of the region is varied from the center to the edge (4, 8, 10, 15, 20, 30, and 62.5 mm away from the center). The best fit to the measurement data is obtained for $S_n = S_p = 10^5$ cm/s and a position 8 mm away from the center.

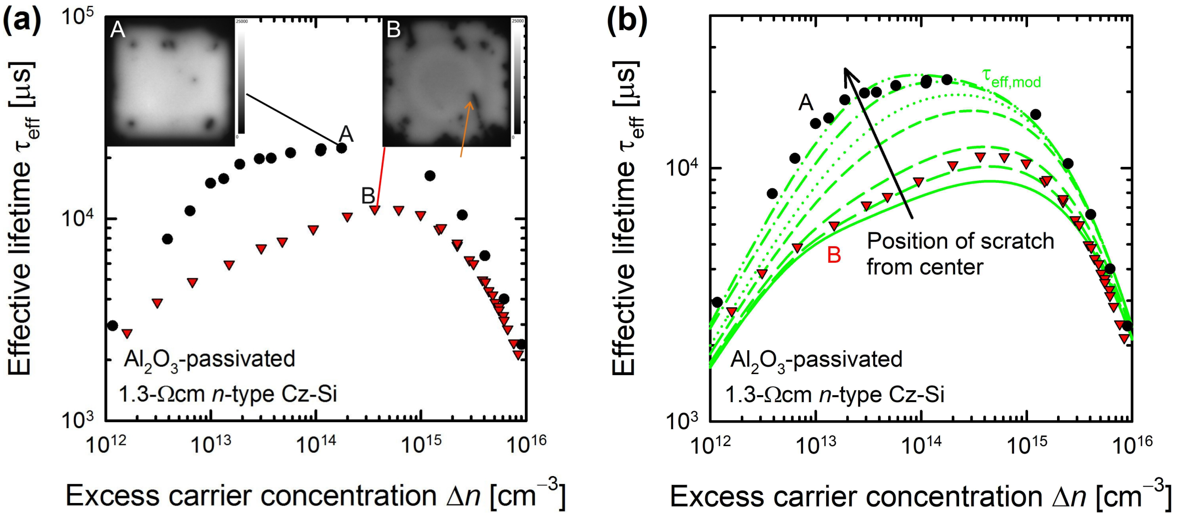

Figure 5.7: Effective lifetime τ_{eff} as a function of excess carrier concentration Δn for two 1.3-Ωcm n-type Cz-Si samples passivated with Al_2O_3, in (a) with an inset showing the PC-PL images for the highest lifetimes and in (b) showing also the simulated lifetimes using Sentaurus Device. For the simulation a 1 µm wide area of reduced passivation is included on the front side, with S_n = S_p = 10^5 cm/s and $Q_{\text{f}} = 0$. The position of this area is varied from the center to the edge.

In Fig. 5.7(b), the simulated lifetime for the variation of the position of the area of reduced lifetime between 4 mm away from the center to the edge is shown. It has to be noted that the model is a 2D model and this area of reduced passivation would be a circle in 3D. The position influences the injection dependence and the maximal lifetime. From this simulation it is obvious that in order to experimentally approach the intrinsic lifetime not only large samples have to be used but the surface passivation has to be extremely homogeneous over the entire sample area, especially close to the center.

The 1.3-Ωcm n-type Cz-Si sample discussed in Section 5.2 which was successively laser-cut into smaller samples also showed an area of reduced lifetime. In order to describe this sample with the model above, the position of the area with reduced lifetime is positioned 8 mm away from the center and $S_n = S_p = 2\times10^5$ cm/s. In Fig. 5.8, the injection-dependent lifetime is shown for different disk diameters.

5.3.4 Impact on limiting efficiency of n-type c-Si solar cells

The intrinsic recombination in the c-Si bulk is one of the limiting factors for the maximal achievable efficiency. Hence, a new parameterization of the intrinsic lifetime also changes the fundamental efficiency limit. Richter et al. [67] presented the most recent calculation of the efficiency limit of c-Si silicon solar cells. We use their approach in order to calculate the efficiency limit implied by our new parametrization $\tau_{\text{intr.n}}$. In

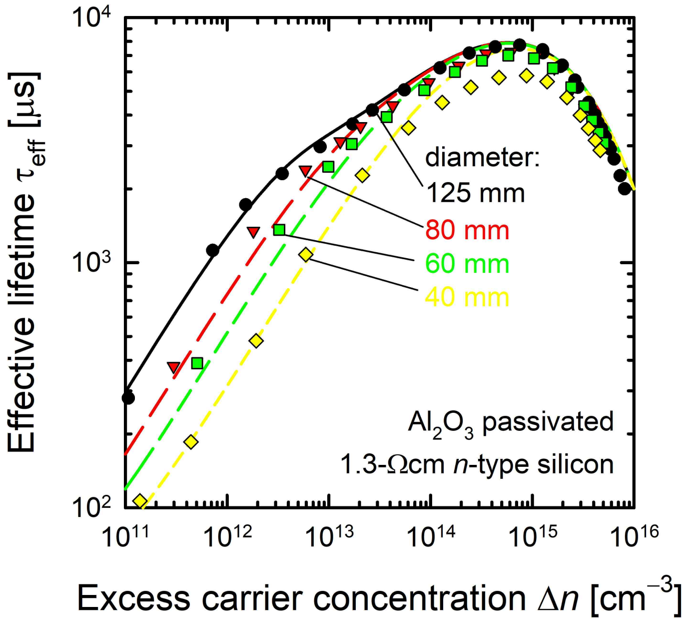

Figure 5.8: Area averaged effective lifetime τ_{eff} as a function of excess carrier concentration Δn measured using PC-PLI and simulated using the model described above. Shown are the results for a 1.3-Ωcm *n*-type Cz-Si sample that is successively laser cut into smaller disks. The lifetime is extracted in the center of the sample on a disk with a diameter of 2 cm. For the simulation an 1 µm wide area of reduced passivation is included on the front side, placed 8 mm away from the center with $S_n = S_p = 2\times10^5$ cm/s and $Q_{\text{f}} = 0$.

order to calculate the fundamental efficiency limit an ideal solar cell without surface and defect recombination, a perfect front-side antireflection coating, and a perfect rear side reflection is modeled [67]. For such an ideal solar cell the current–voltage $(J\text{–}V)$ characteristic is expressed by [67]

$$J = J_{\text{L}} - qWU_{\text{intr}}(V), \tag{5.6}$$

with J_{L} being the photo-generated current density and $U_{\text{intr}}(V)$ the intrinsic recombination. In order to calculate J_{L}, Eq. (3) of Ref. [67] and all the assumption described within are used. Hence, every absorbed photon creates only one electron-hole pair, Lambertian light-trapping together with an isotropic response of the cell is assumed, and free carrier absorption is taken into account.

For the calculation of the dependence of U_{intr} on V the assumption of ideal contacts and "narrow base" is made, and hence, Δn is related to V by [67, 68]

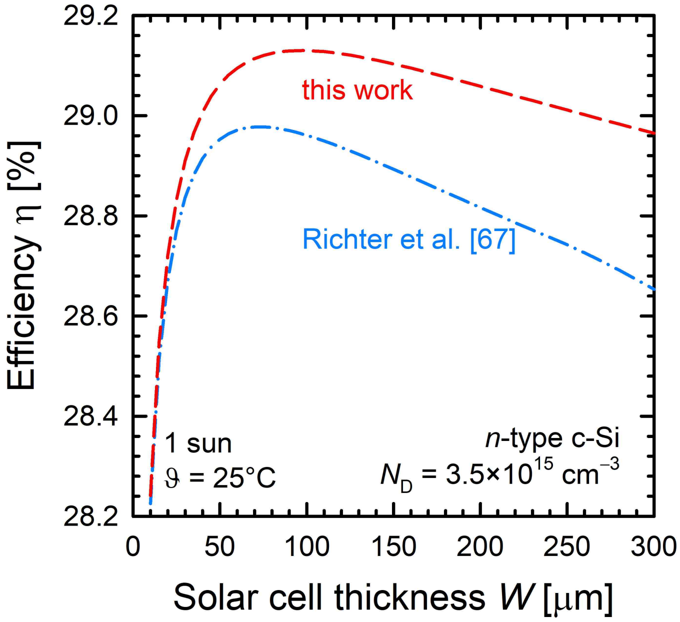

Figure 5.9: Efficiency η as a function of the solar cell thickness W for n-type silicon solar cells with $N_\mathrm{D} = 3.5{\times}10^{15}$ cm^{-3}. Shown is the efficiency calculated according to Richter et al. [67] using the intrinsic lifetime $\tau_\mathrm{intr.Richter}$ (Eq. (2.10)) [6] (dash-dotted line) and the new parameterization $\tau_\mathrm{intr.n}$ (Eq. (5.5)) (dashed line).

$$(n_0 + \Delta n)(p_0 + \Delta n) = n_\mathrm{i,eff}^2 \exp\left(\frac{qV}{kT}\right). \tag{5.7}$$

This equation can further be transformed into

$$\Delta n = -\frac{n_0 + p_0}{2} + \sqrt{n_\mathrm{i,eff}^2 \exp\left(\frac{qV}{kT}\right) + \left(\frac{n_0 + p_0}{2}\right)^2 - n_0 p_0}. \tag{5.8}$$

$n_\mathrm{i,eff}$ is calculated using Eq. (2.4) with the n_i value at 25 °C ($n_\mathrm{i} = 8.28{\times}10^9$ cm^{-3}) as used by Richter et al. [67].

The intrinsic recombination is calculated using Eq. (2.1) either with $\tau_\mathrm{intr.Richter}$ Eq. (2.10) or $\tau_\mathrm{intr.n}$ Eq. (5.5) for τ_i, including "photon recycling" as described by Richter et al. [67]. This is done by multiplying the coefficient of the radiative recombination B_low in Eq. (2.10) and Eq. (5.5) with $(1 - P_\mathrm{PR})$, with P_PR being the photon recycling probability calculated using Eq. (8) of Ref. [67].

Finally, the efficiency was calculated numerically by varying V with a step size of 0.1 mV and solving Eq. (5.6) iteratively. The open-circuit voltage V_oc was calculated by finding the minimum of $|J|$, the maximum power was calculated by finding the maximum value for $J{\cdot}V$. From the maximum power, V_oc, and J_sc the fill factor FF was calculated.

Figure 5.9 shows the efficiency limit of n-type silicon solar cells ($N_\mathrm{D} = 3.5\times10^{15}$ cm^{-3}) as a function of the solar cell thickness. The new parameterization $\tau_\mathrm{intr.n}$ (Eq. (5.5)), introduced in this thesis, results in a maximal efficiency of 29.13%, whereas the maximal efficiency of the Richter lifetime $\tau_\mathrm{intr.Richter}$ is 28.98%. Not only the maximal efficiency is increased, but also the optimal solar cell thickness, from 75 µm for $\tau_\mathrm{intr.Richter}$ to 95 µm for $\tau_\mathrm{intr.n}$. The main difference between the best solar cells is an increased FF for the solar cell calculated using $\tau_\mathrm{intr.n}$. The increased FF can be attributed to a higher lifetime at the injection density corresponding to the maximum power point, i.e., $\Delta n_\mathrm{mpp} \approx 5\times10^{15}$ cm^{-3}.

5.4 Chapter summary

Our experiments and simulations have shown, that for lower injection densities $\Delta n < 10^{15}$ cm^{-3} the effective surface recombination velocity $S_\mathrm{eff}(\Delta n)$ of n-type c-Si wafers, passivated using PA-ALD Al_2O_3, is influenced by the coupling of the measurement area to areas of high recombination. The main areas of high recombination are the edges, and hence, a sample size dependence of the measured effective surface recombination velocity $S_\mathrm{eff}(\Delta n)$ was observed. However, also areas of increased recombination located on the sample surfaces influence the injection dependence of $S_\mathrm{eff}(\Delta n)$. Our simulations showed that the areas of poor surface passivation increase the measured S_eff values not only at injection densities below 10^{15} cm^{-3} but also up to 10^{16} cm^{-3}. Therefore, we conducted an experiment avoiding almost all areas of poor surface passivation quality on the sample and using large-area wafers (12.5×12.5 cm^2). On this 1.2-1.4 Ωcm n-type Cz-Si samples, we measured effective lifetimes exceeding the current state-of-the-art parameterization of the intrinsic lifetime of c-Si. Hence, we performed a new parameterization of the intrinsic lifetime for n-type c-Si. Our new parameterization increases the fundamental efficiency limit for n-type c-Si solar cells. This was exemplarily shown for n-type silicon solar cells with $N_\mathrm{D} = 3.5\times10^{15}$ cm^{-3}, for which an increase from 28.98% using $\tau_\mathrm{intr.Richter}$ to 29.13% using our new $\tau_\mathrm{intr.n}$ was calculated.

Chapter 6

Solar cells with Al_2O_3 as rear-side passivation layer

An important application of the Al_2O_3 passivation of c-Si surfaces is the use as rear-side passivation layer in the so-called "Passivated Emitter and Rear Cell" (PERC) [5]. One research effort over the last years is to transfer the high efficiency potential of the PERC solar cells from laboratory scale into mass production [69]. An important step for this is the implementation of the screen-printing process for metalization. The screen-printing process used for the metalization of PERC solar cells, however, requires a high-temperature firing step for the contact formation. Therefore, one important prerequisite for the Al_2O_3 rear side passivation is a good surface passivation quality after a firing step. To some extend this has already been discussed in Chapter 4 and all investigated Al_2O_3 deposition methods provide Al_2O_3 layers with a good surface passivation after a firing step. In this Chapter, the firing stability is examined by implementing PA-ALD Al_2O_3 and ICP-AlO_x layer into actual PERC solar cells.

Besides the good passivation quality after firing, also the stability of the layer against the metalization paste, an aluminum paste in the case of PERC solar cells, during the firing is important. The Al_2O_3 itself is not stable against the aluminum paste and, therefore, a protection layer is required. The SiN_x routinely used, however, is usually deposited by PECVD, a technique that requires vacuum. In this Chapter, an alternative capping will be evaluated, namely liquid-phase-deposited (LPD) dielectric layers based on silicon oxide (SiO_x). This layers are deposited via spin-coating, but can also be deposited via spray-on techniques. The evaluated LPD dielectric layers are liquid siloxane-based solutions, fabricated by the company Optitune.

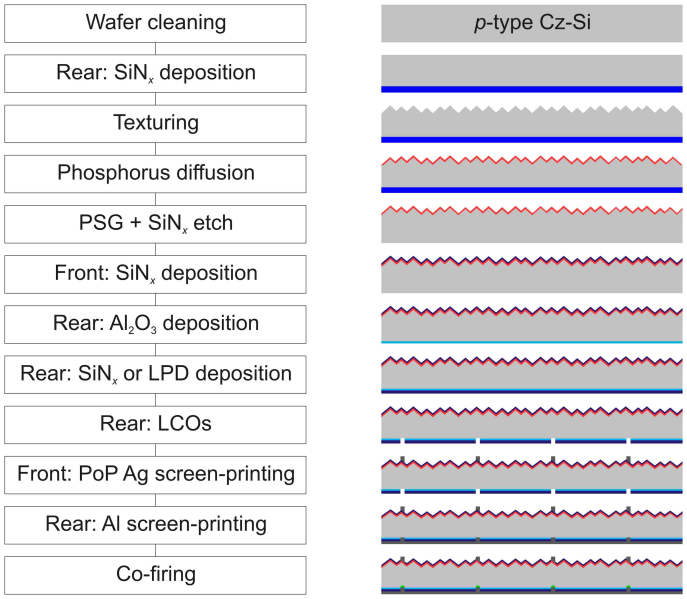

Figure 6.1: PERC process flow.

6.1 Process flow for industrial-type PERC solar cells

The PERC process flow applied in this thesis is basically the ISFH-developed process flow described in Ref. 69. In Fig. 6.1, the process flow is shown. As base material 15.6×15.6 cm^2 pseudo-square p-type boron-doped Cz-Si wafers with a resistivity between 2 and 3 Ωcm and an initial thickness of 200 µm are used. The wafers are cleaned using a Puratron clean, a KOH damage etch, and an RCA clean, successively. A SiN_x protection layer is deposited on the rear side and the front side is textured in an alkaline KOH/IPA-based chemical bath, resulting in about 3-5 µm large randomly distributed pyramids. The n^+-emitter is formed on the front surface by $POCl_3$ diffusion performed in a quartz-tube furnace, resulting in a sheet resistance R_{sheet} of about 60 Ω/sq. The phosphorus silicate glass and rear side protection layer is removed by etching in HF. On the front side, a single SiN_x anti-reflective layer with a refractive index of $n = 2.05$ and a thickness of 70 nm is deposited. On the rear side, a Al_2O_3/SiN_x or a Al_2O_3/LPD stack is deposited. The stack on the rear side is locally ablated by laser contact opening (LCO) in order to form local line openings [70]. On the front side, a silver (Ag) grid is deposited by a print-on-print (PoP) screen-printing process, resulting in a finger width of around 70 µm. The Al rear contact is formed by full-area Al screen printing applying a commercially available Al paste designed for local contacts. Finally, the solar cells are characterized using the LOANA I–V characterization tool (pvtools).

6.2 Implementation of ICP-AlO$_x$ into PERC solar cells

The PERC solar cells are fabricated using the process flow described above. In this Section, as rear-side passivation layer, ICP-AlO$_x$/SiN$_y$ stacks are used with 20 or 30 nm thick ICP-AlO$_x$ layers, respectively, and PA-ALD Al$_2$O$_3$/SiN$_y$ stacks with a 10 nm thick PA-ALD Al$_2$O$_3$ layer. The PECVD-SiN$_y$ capping layer thickness is 200 nm for all solar cells fabricated in this Section.

6.2.1 Solar cell results

Table 6.1 summarizes the measured I–V parameters of the average and the best solar cell of each split group. All Al$_2$O$_3$ layers applied provide a very good rear side passivation quality, resulting in independently confirmed maximal open-circuit voltages V_{oc} between 655 mV and 657 mV. This implies that the rear-side passivation quality for all stacks is very good and the slightly lower surface passivation quality of ICP-AlO$_x$/SiN$_y$ compared to PA-ALD Al$_2$O$_3$/SiN$_y$ stacks, shown in Section 4.3, is not limiting the V_{oc}. The short-circuit densities J_{sc} are also very similar with values between 39.0 mA/cm^2 and 39.2 mA/cm^2. The main difference between the three groups is the fill-factor FF, however, this is mainly due to an increased series resistance. This is a measure for the contact quality and not the passivation quality. The highest independently confirmed efficiency of 20.1% is provided by a PERC solar cell with a 30 nm thick ICP-AlO$_x$ layer, however, this is only due to the high FF. In conclusion, all investigated stacks are suitable for high efficiencies.

Table 6.1: I–V parameters measured under standard testing conditions (STC) of 15.6×15.6 cm^2 p-type Cz-Si PERC solar cells using ICP-AlO$_x$/SiN$_y$ and PA-ALD Al$_2$O$_3$/SiN$_y$ stacks as rear side passivation. Shown is the average measured at ISFH and in brackets the best cell independently confirmed at Fraunhofer ISE CalLab.

Rear side Al$_2$O$_3$	V_{oc} [mV]	J_{sc} [mA/cm^2]	FF [%]	η [%]
30 nm ICP-AlO$_x$, 3 cells	653±1 (655)	39.0±0.1 (39.0)	77.1±0.5 (78.8)	19.6±0.1 (20.1)
20 nm ICP-AlO$_x$, 4 cells	655±1 (657)	39.1±0.1 (39.1)	76.5±0.2 (77.8)	19.5±0.1 (20.0)
10 nm PA-ALD Al$_2$O$_3$, 2 cells	656±1 (656)	39.1±0.1 (39.2)	76.2±0.1 (76.9)	19.5±0.1 (19.8)

6.3 Alternative capping layer for Al_2O_3

In the previous Section PECVD-SiN_x was applied as capping layer for the Al_2O_3 passivation layer. In this Section, the applicability of LPD layers as capping layer will be evaluated. In order to evaluate the capping layers, three main attributes can be defined:

1. The capping layer does not reduce the surface passivation quality provided by the Al_2O_3 layer after firing.
2. The capping layer blocks the Al paste.
3. The capping layer enhances the rear side reflectance.

The focus of the following experiments is to investigate the first two points. The third point was already evaluated by Bullock et al. [71] using device simulations. They showed that the rear-side reflectance is increased due to the LPD layer, even in comparison to a SiN_x capping layer, resulting in a gain in J_{sc} of 0.025 $\mathrm{mA/cm^2}$ compared to SiN_x as capping layer.

6.3.1 Deposition of LPD layers

For the deposition of the LPD layers, three different liquid siloxane-based solutions are used. The different solutions contain either (i) only siloxane (resulting in layers of SiO_x), (ii) siloxane and AlO_y (SiO_xAlO_y), or (iii) siloxane and titanium oxide (SiO_xTiO_y). These solutions are deposited onto the silicon surfaces using a two-step spin-coating process, first a slow spinning with 300 rpm for 10 sec in order to distribute the solution equally on the surface and then a fast spinning with 1000 rpm for 50 sec or 900 rpm for 30 sec in order to define the thickness of the layer. The 900 rpm for 30 sec results in LPD layers with ~15% increase in layer thickness compared to the 1000 rpm for 50 sec. After the deposition a bake-out step in ambient environment is performed at 220 °C for 5 minutes. The thickness of the LPD layers is typically between 100 and 150 nm, therefore, in order to deposit thick layers, the spin-on and bake out process is repeated until the desired thickness is reached.

The homogeneity of the LPD layers is determined using RCA-cleaned large-area (15.6×15.6 $\mathrm{cm^2}$) p-type Cz-Si wafers polished on one side using the InPolish (RENA) system. On the polished side, the LPD layers are deposited using the spin-on process described above. In Fig. 6.2, photos of two exemplary samples after spin-on deposition are shown. The LPD-SiO_x and the LPD-SiO_xTiO_y layers, both show an average thickness

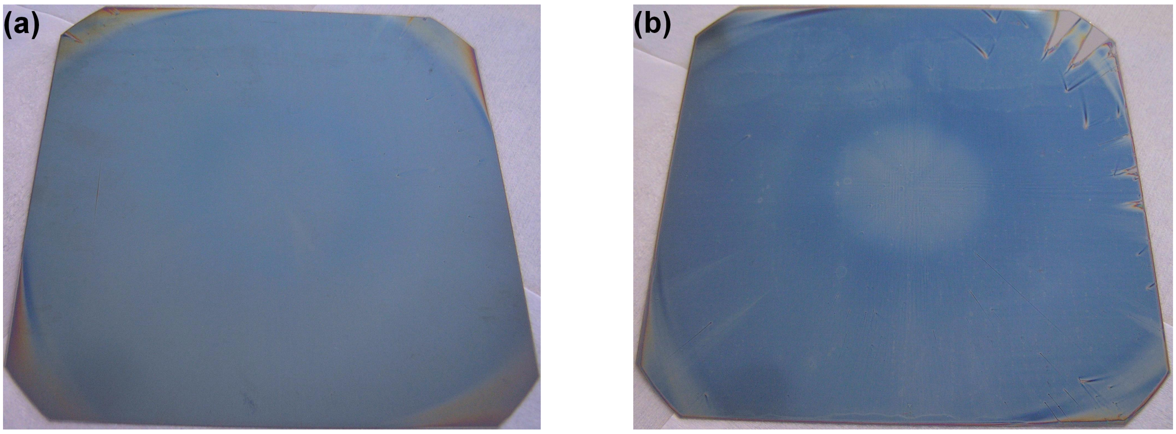

Figure 6.2: Pictures of the polished samples with one layer of (a) LPD-SiO_xTiO_y and (b) LPD-SiO_xAlO_y.

of 100 nm, whereas the LPD-SiO_xAlO_y layer shows an average thickness of 120 nm, as measured by ellipsometry. Due to the spin-coating process, all three layers show an increased thickness in the corners of the wafers, for the LPD-SiO_x and the LPD-SiO_xAlO_y an increased thickness can also be detected in the center of the samples, see Fig. 6.2 for a comparison between (a) the LPD-SiO_xTiO_y and (b) the LPD-SiO_xAlO_y layers. This increase in thickness can be up to 35% in the case of LPD-SiO_xAlO_y. Besides the corners and the center, all three solutions result in very homogeneous LPD layers over the large area and especially no areas of reduced thickness can be found. These results, however, can only be obtained on polished surfaces. Experiments conducted on KOH-etched surfaces show a stronger variation in layer thickness.

KOH-etched samples that are investigated using a scanning electron microscope (Hitachi S-4800, SEM) show on microscopic scale a film thickness between 0 nm and

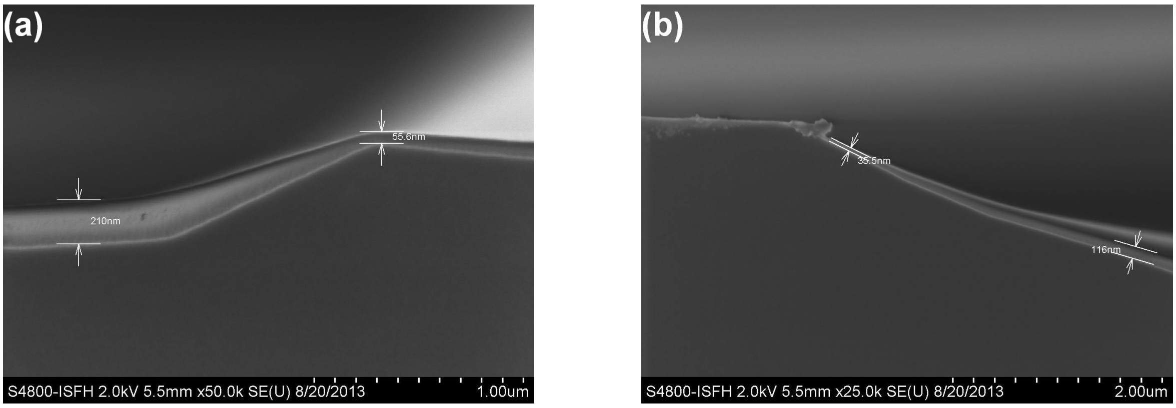

Figure 6.3: Cross-sectional SEM images of a KOH-etched Cz-Si wafer with one layer of LPD-SiO_x.

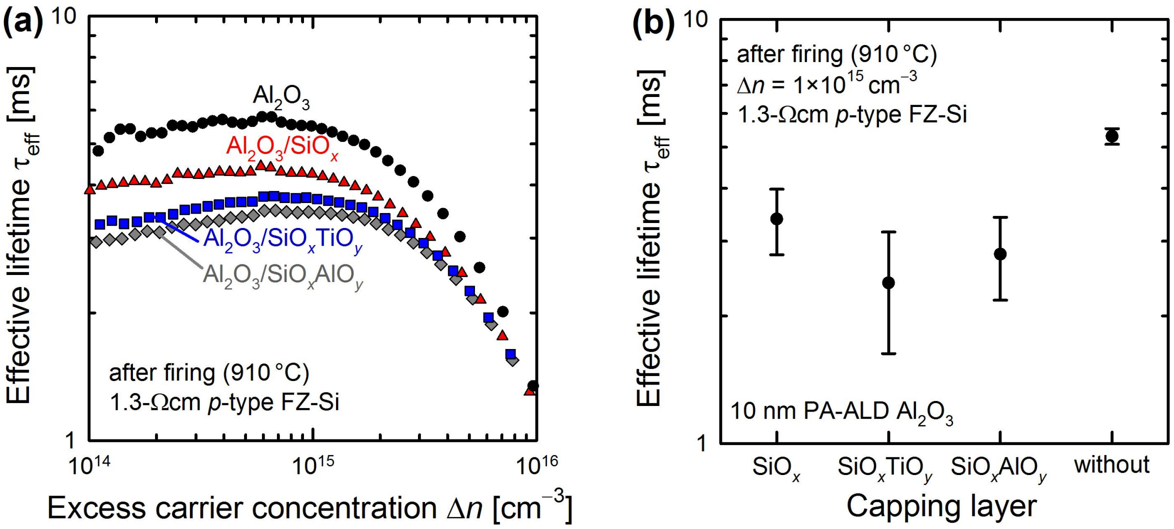

Figure 6.4: 1.3-Ωcm p-type FZ-Si samples passivated with PA-ALD Al_2O_3 with different LPD layers as capping after firing using the fast firing profile with a set-peak temperature of 910 °C. In (a) the highest measured effective lifetimes τ_{eff} are shown as a function of excess carrier concentration Δn and in (b) the average lifetimes and standard deviations of 9 measurements at different positions of the wafers are compiled.

~500 nm, depending on the surface topology. KOH-etched surfaces typically show etch pits with different depths. Inside of these pits, the film thickness is strongly increased and at the flanks and especially at the rim, the film thickness is decreased. Fig. 6.3 shows two SEM images of a sample that should have a LPD-SiO_x layer with a thickness of 100 nm. In Fig. 6.3(a), a shallow pit is shown and the LPD-SiO_x is within the pit 210 nm thick and at the rim only 55 nm. In Fig. 6.3(b), a deeper pit on this sample is shown and at the rim no LPD-SiO_x layer can be seen. Therefore, all results shown in the following are obtained on polished samples.

6.3.2 Firing of Al_2O_3/LPD stacks

The surface passivation quality provided by Al_2O_3/LPD stacks after firing is evaluated on 12.5×12.5 cm^2 p-type FZ-Si wafers with a resistivity of 1.3 Ωcm and a thickness of 300 µm. The wafers are shiny-etched by the supplier and receive an RCA clean prior to the surface passivation. On both sides, a 10 nm thick PA-ALD Al_2O_3 layer and an LPD layer are deposited, successively, in order to form Al_2O_3/LPD stacks. After the LPD deposition the samples are fired using the fast firing profile (see Section 4.2.1) with a set-peak temperature of 910 °C. After firing, the samples are measured using the PCD technique at 9 different positions.

Figure 6.4(a) shows the injection dependence of the highest effective lifetimes τ_{eff} measured for the three Al_2O_3/LPD stacks compared to a single Al_2O_3 layer. The measured effective lifetimes of all three types of Al_2O_3/LPD stacks are above 3 ms at an injection density of $\Delta n = 1 \times 10^{15}$ cm^{-3}, which corresponds to excellent S_{eff} values below 3 cm/s. The best surface passivation quality is provided by the single Al_2O_3 layer. The single Al_2O_3 layer also provides the highest average lifetime and the smallest standard deviation. This can be seen in Fig. 6.4(b), where the average lifetimes and standard deviations of 9 measurements at different positions of the wafers are shown. This is also verified by means of dynamic ILM measurement, where the deviations from the average lifetimes are only 0.4 ms over the entire wafer area for the single PA-ALD Al_2O_3 layer, whereas they are 0.8 ms for the LPD-SiO_x and the LPD-SiO_xTiO_y and 1 ms for the LPD-SiO_xAlO_y capping layers. Nevertheless, the surface recombination velocities are well below 10 cm/s for all investigated types of stacks over the entire wafer area. Hence, the Al_2O_3/LPD stacks provide an excellent surface passivation quality after firing, almost independent of the exact composition of the LPD precursor.

6.3.3 Stability against Al paste on 12.5×12.5 cm^2

The stability against the Al paste is evaluated using lifetime samples fabricated as described above. On these lifetime samples aluminum paste is screen-printed on the rear side over the full area. After the screen-printing process, the samples are fired with a firing profile that is used for the PERC contact formation. The samples are evaluated using dynamic ILM. The samples cannot be measured using the PCD since one side is metalized.

After the firing, the samples show, as expected, that the Al_2O_3 layer itself is not a sufficient barrier against the Al paste and the silicon is contacted by the Al paste over almost the entire area. However, only a thin Al-p^+ BSF is formed, providing a poor contact passivation quality, and consequently a poor surface passivation quality with $S_{\text{eff}} > 800$ cm/s. The stacks with one layer of LPD-SiO_x and one layer of LPD-SiO_xAlO_y show a similar behavior with the difference that the contacted area is smaller, but the surface passivation quality is quite poor ($S_{\text{eff}} > 300$ cm/s). Figure 6.5 shows an exemplary SEM image of a sample with an Al_2O_3/SiO_xAlO_y stack plus Al paste after firing. Only the sample with one layer of LPD-SiO_xTiO_y shows no penetration of the Al through the passivation stack, however, the stack does not provide a sufficient level

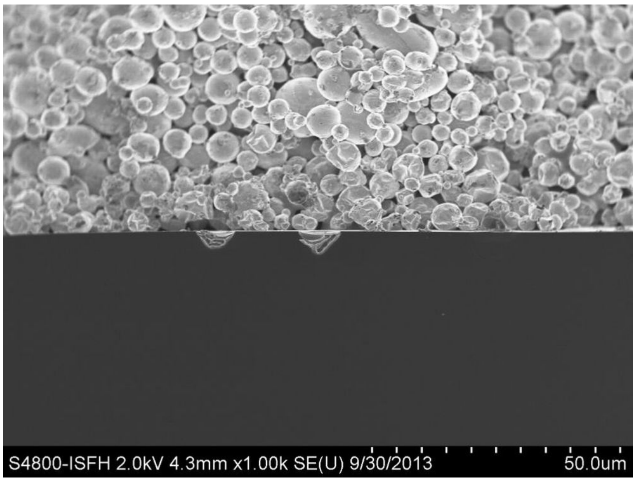

Figure 6.5: Cross-sectional SEM image of a sample with an Al_2O_3/SiO_xAlO_y stack and Al paste on top after firing. The LPD layer is ~110 nm thick and cannot be observed at this resolution.

of surface passivation, resulting in $S_{\text{eff}} > 500$ cm/s. Hence, the reduction in surface passivation quality is not only due to the local contacts of the Al with the Si, but also to some interaction of the Al paste, e.g., the solvent, with the Si interface.

Since the LPD-SiO_xTiO_y capping layer prevents the penetration of the aluminum paste, another set of samples was fabricated with the same sample structure as above, but with a LPD-SiO_xTiO_y layer on-top of the other LPD layer. The aluminum paste on this samples is screen printed on a 10×10 cm^2 area, marked with a red box in Fig. 6.6(a) and (b), whereas the silicon wafer have a size of 12.5×12.5 cm^2. All samples of this experiment show no penetration of the aluminum paste, but still a reduced lifetime in the area of the aluminum paste. The only exception is the sample with a LPD stack of a ~100 nm thick SiO_x and a ~100 nm thick SiO_xTiO_y on top of the Al_2O_3 layer with an average S_{eff} of 80 cm/s, the dynamic ILM image is shown in Fig. 6.6(a). The reference sample with PECVD-SiN_x as capping, however, has an average S_{eff} of only 5 cm/s, the dynamic ILM image is shown in Fig. 6.6(b). Hence, the interaction between the aluminum paste and the Si interface is still not totally suppressed.

In another experiment, the use of thick LPD-SiO_x and LPD-SiO_xAlO_y layers and the use of a thick LPD-SiO_xTiO_y layer on top of LPD-SiO_x were evaluated. For this experiment, the samples were passivated with an Al_2O_3/SiN_x stack on the front side and an Al_2O_3 layer with five different cappings on the rear side: (i) ~400 nm thick LPD-SiO_x, (ii) ~400 nm thick LPD-SiO_xAlO_y layer, (iii) a ~300 nm thick LPD-SiO_xTiO_y layer on top of a ~100 nm, (iv) a ~300 nm thick LPD-SiO_xTiO_y layer on top of a ~200 nm thick LPD-SiO_x layer, and (v) a 200 nm thick SiN_x layer. On the rear of

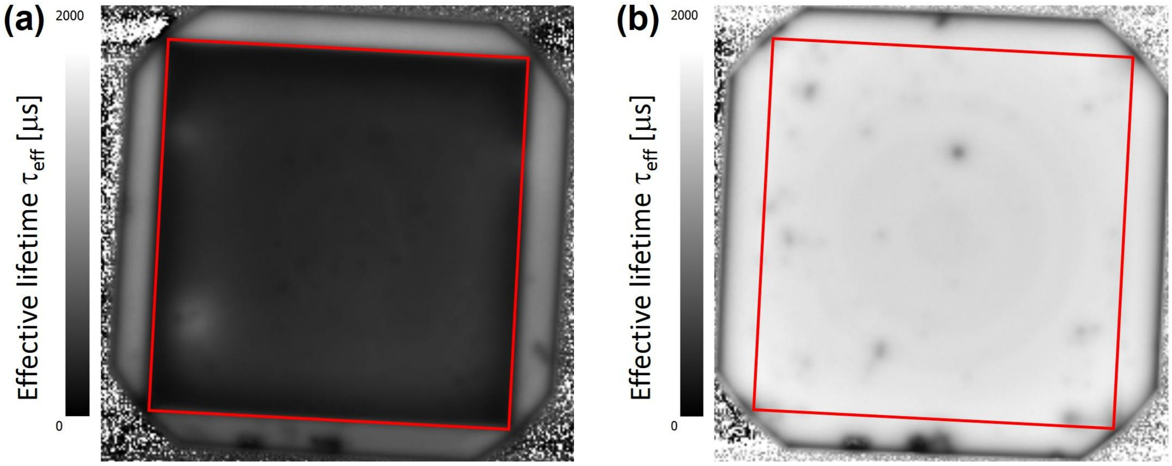

Figure 6.6: Dynamic ILM images of 12.5×12.5 cm^2 1.3-Ωcm *p*-type FZ-Si samples with (a) a Al_2O_3/SiO_x(100 nm)/SiO_xTiO_y(100 nm) stack and (b) a Al_2O_3/SiN_x(200 nm) stack, both with Al paste printed within the marked box (red) and subsequent firing.

all samples, the aluminum paste is screen-printed on a 10 × 10 cm^2 area. Non of the samples show a penetration of the aluminum paste and the surface passivation quality is only reduced for the sample with a thick LPD-SiO_xAlO_y, see Fig. 6.7(a). This reduced lifetime results in an area-averaged S_{eff} of 100 cm/s, see Fig. 6.8. All other capping layers provide area-averaged S_{eff} values below 10 cm/s. It is noteworthy that this capping layers show no difference in surface passivation quality between the metalized and the non metalized area, exemplary shown for the Al_2O_3/SiO_x(200 nm)/SiO_xTiO_y(300 nm) stack in Fig. 6.7(b).

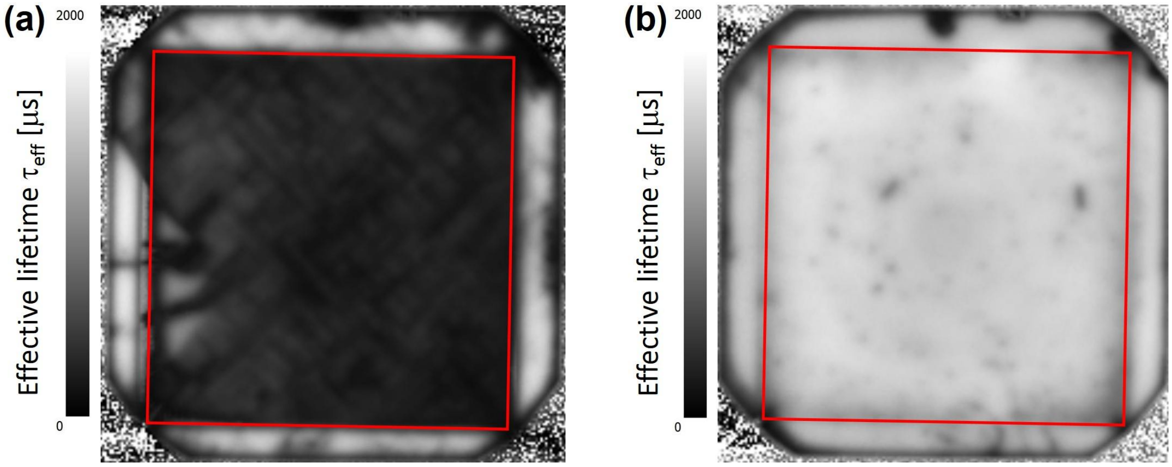

Figure 6.7: Dynamic ILM images of 12.5×12.5 cm^2 1.3-Ωcm *p*-type FZ-Si samples with (a) a Al_2O_3/SiO_xAlO_y(400 nm) stack and (b) a Al_2O_3/SiO_x(200 nm)/SiO_xTiO_y(300 nm) stack, both with Al paste printed within the marked box (red) and subsequent firing.

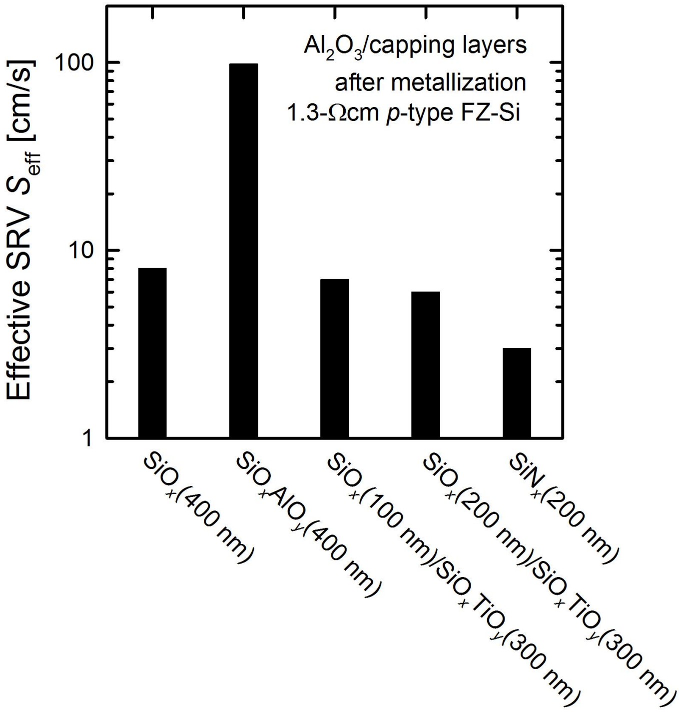

Figure 6.8: Area-averaged S_{eff} after firing for different capping layers. The S_{eff} values are extracted from dynamic ILM measurements.

6.3.4 Stability against Al paste on 15.6×15.6 cm^2

The previous results were achieved on 12.5×12.5 cm^2 shiny-etched FZ-Si wafer, however, the PERC process applied at ISFH is optimized for large (15.6×15.6 cm^2) Cz-Si wafers and, therefore, the stability of the capping layers on large area Cz-Si wafers has to be evaluated too. The investigation of the homogeneity already showed that a polished surface is crucial. The polished surface is reached by adapting the cleaning process. The Cz-Si wafers are cleaned using Puratron followed by an 1 min KOH-etch. Successively both sides of the wafer are polished in the InPolish process. On the front side, 10 µm of silicon are removed and on the rear 24 µm. After this polishing, the rear surface still shows an increased roughness compared to the shiny-etched FZ-Si samples. This can lead to an increased inhomogeneity of the LPD layers and, therefore, the thickness of the LPD-SiO_x and LPD-SiO_xTiO_y layers are increased for the evaluation of the Al_2O_3/LPD stacks on polished Cz-Si wafers.

The samples are fabricated using 15.6×15.6 cm^2 p-type Cz-Si wafer with a resistivity of ∼2 Ωcm that are cleaned and polished as described above. After RCA cleaning, on both wafer surfaces a 10 nm thick PA-ALD Al_2O_3 is deposited. On the front side, a 100 nm thick SiN_x is deposited and on the rear side thick LPD-SiO_x and LPD-

SiO_x/SiO_xTiO_y stacks with different thicknesses are deposited using spin-coating in ambient environment. As a reference, on one sample SiN_x is symmetrically deposited on both sides. Samples with LPD stacks consisting of a 300 nm thick LPD-SiO_x layer and 420 nm thick LPD-SiO_xTiO_y layer are annealed for 2 min at 400, 500, and 600 °C. On the rear side of all samples the aluminum is screen-printed on the entire area. After the screen-printing, the samples are fired using the same firing profile as used for the production of the PERC solar cells.

For all sample with only a thick layer of LPD-SiO_x as capping layer, a penetration of the aluminum through the capping layer is observed, resulting in lifetimes < 40 µs. This is in contrast to the experiment on FZ-Si. The reason might be the inhomogeneity of the LPD-SiO_x layer or a different sample temperature during the firing. This different temperature is due to a different sample thickness, the FZ-Si is 300 µm thick whereas the Cz-Si is only ~150 µm thick after the polishing. This leads to a higher temperature during the firing process for the Cz-Si samples. The SiO_x/SiO_xTiO_y stacks, however, are still stable against the aluminum paste, but all samples with the exception of the annealed samples show a low adhesion of the aluminum at the edges and for the sample with the thickest LPD stack the aluminum is detached almost over the entire area.

Table 6.2: Variation of LPD-SiO_x and LPD-SiO_xTiO_y layer thickness and resulting lifetimes. Shown are the area-averaged lifetimes over the total area and the lifetimes only averaged over the center region ($2{\times}2$ cm^2). Also included is the lifetime for a sample with a 200 nm thick SiN_x capping layer.

SiO_x thickness [nm]	SiO_xTiO_y thickness [nm]	Annealing temperature [°C]	Lifetime total area [µs]	Lifetime center (4 cm^2) [µs]	Detaching of Al
300	420	–	550	1020	some at edges
300	420	400	380	700	no detaching
300	420	500	300	600	no detaching
300	420	600	650	1110	no detaching
430	120	–	680	960	some at edges
430	280	–	650	930	some at edges
570	120	–	720	1170	some at edges
570	280	–	680	1030	a lot at edges
570	420	–	580	855	almost entirely
SiN_x reference		–	820	1400	no detaching

Group	SiN_x	440/320	600/140	600/280	600/280-anneal
1st capping layer	200 nm SiN_x	440 nm SiO_x	600 nm SiO_x	600 nm SiO_x	600 nm SiO_x
2nd capping layer		320 nm SiO_xTiO_y	140 nm SiO_xTiO_y	280 nm SiO_xTiO_y	280 nm SiO_xTiO_y
Annealing					2 min at 600 °C

Figure 6.9: PA-ALD Al_2O_3 capping layer and treatment of each group.

In Tab. 6.2, the lifetime results and detaching of aluminum is summarized for the SiO_x/SiO_xTiO_y stacks and SiN_x reference. The detaching of the aluminum can be correlated to an increased LPD layer thickness at the edges. For all non-annealed samples and the sample annealed at 600 °C, a high lifetime in the center is measured, however, the highest lifetime is measured for the SiN_x reference sample. The resulting S_{rear} values are 10 cm/s for the SiN_x reference sample and for all non-annealed samples below 25 cm/s.

From this experiment it can be concluded that only SiO_x/SiO_xTiO_y stacks are suitable for the use on 15.6×15.6 cm^2 Cz-Si samples. The thickness of both layer seems to be not a crucial parameter for the passivation quality, however, the use of thick (570 nm) LPD-SiO_x layer in conjunction with thick ($\geq$ 280 nm) LPD-SiO_xTiO_y leads to very low adhesion of the Al layer. The adhesion of the Al layer can be increased by an annealing step prior to the screen-printing process, hence, the most promising LPD stack is the 300 nm thick LPD-SiO_x layer in conjunction with a 420 nm thick LPD-SiO_xTiO_y layer and an annealing step at 600 °C for 2 min.

6.3.5 Solar cell results

We fabricated 5 groups of PERC solar cells using the process flow as described in Section 6.1, with the adaption of the cleaning step and the rear capping layer deposition. Instead of a 10 min KOH etch, the samples are etched for 1 min in KOH and successively polished on the front and rear. During the polishing 10 µm of silicon is etched on the front and 24 µm on the rear. Each group received a different type of capping layer, see Fig. 6.9. The samples of group 600/280-anneal received an annealing step at 600 °C for 2 min after the deposition of the capping layer.

The results for the solar cells are summarized in Tab. 6.3. The best results are achieved with the SiN_x capping layer (group SiN_x), with the best efficiency of 20.2% and an average efficiency of 19.8±0.2%. The PERC solar cells with the LPD capping layers show for all I–V parameters reduced values. The best results for the LPD capping layers are achieved for the annealed LPD stack (group 600/280-anneal), with an efficiency of 19.8% for the best solar cell. The solar cells of this group also did not show any detaching of the aluminum on the rear. For all groups with LPD capping layers without an annealing step a partial detaching of the aluminum on the rear is observed at the corners, with the most detaching for the solar cells with a LPD stack consisting of a 440 nm thick LPD-SiO_x layer and a 320 nm thick LPD-SiO_xTiO_y layer (group 440/320).

In order to understand the reason for the lower efficiency of the solar cells with a LPD capping layers, electroluminescence (EL) measurements were performed. The solar cells with the SiN_x capping layer (group SiN_x) and the best solar cell with the annealed LPD stack (group 600/280-anneal) show a very homogeneous luminescence, see Fig. 6.10(a), whereas all other cells show areas of reduced luminescence. Figure 6.10(a) shows the solar cell with the lowest efficiency, this solar cell is from group 440/320 and has an efficiency of only 17.8%. The detaching of the Al can be seen in the EL-image as areas with no luminescence. Most of the detaching can be seen on the right side of the EL-image. On the left side of the EL-image small areas of reduced luminescence can be seen. This areas of reduced luminescence are due to inhomogeneities of the LPD layers due to the spin-coating process used, and hence, a reduced rear surface passivation quality after the firing step. For other solar cells even larger areas of reduced luminescence are

Table 6.3: *I–V* parameters measured under standard testing conditions (STC) of 15.6×15.6 cm^2 *p*-type Cz-Si PERC solar cells using PA-ALD Al_2O_3/SiN_y and PA-ALD Al_2O_3 with different capping layers as rear side passivation. Shown is the best solar cell and in brackets the average, all measured at ISFH.

Group	V_{oc} [mV]	J_{sc} [mA/cm^2]	FF [%]	η [%]
SiN_x (4 cells)	655 (650±3)	38.7 (38.3±0.2)	79.6 (79.5±0.3)	20.2 (19.8±0.2)
440/320 (4 cells)	642 (638±2)	37.2 (36.9±0.2)	77.2 (77.2±0.2)	18.4 (18.2±0.2)
600/140 (3 cells)	642 (637±3)	37.8 (37.5±0.2)	78.9 (78.0±0.6)	19.2 (18.7±0.3)
600/280 (3 cells)	645 (643±2)	37.1 (37.3±0.3)	79.1 (78.2±0.6)	19.0 (18.8±0.2)
600/280-anneal (2 cells)	651 (651±1)	38.3 (38.1±0.2)	79.3 (79.0±0.3)	19.8 (19.6±0.2)

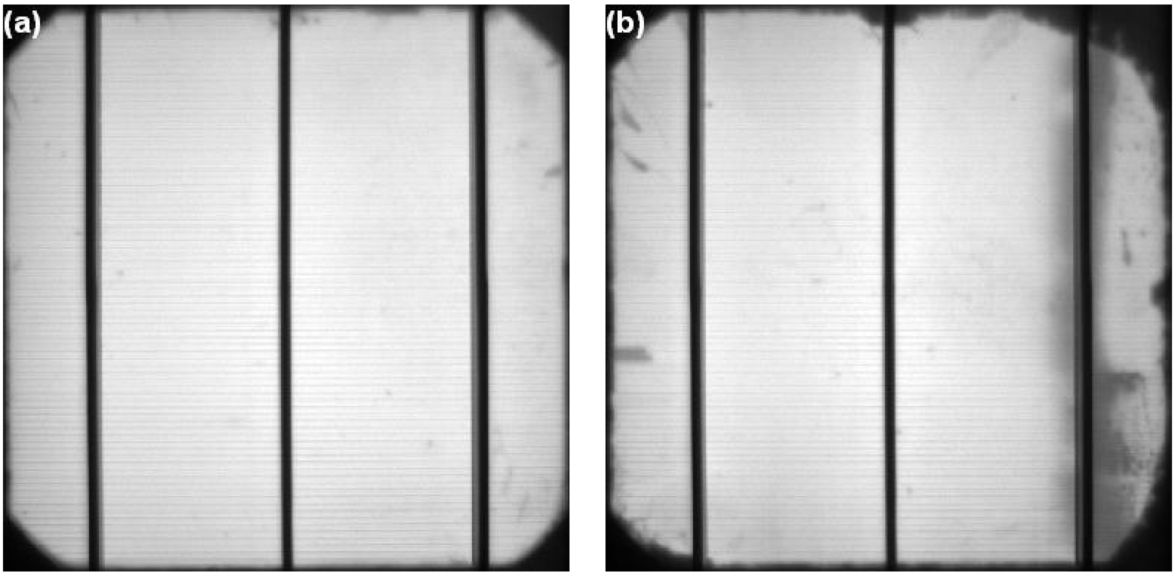

Figure 6.10: EL-images of (a) the best solar cell with a LPD stack consisting of a 600 nm thick SiO_x layer and a 280 nm thick SiO_xTiO_y layer (group 600/280-anneal), the stack was annealed at 600 °C for 2 min, and (b) the solar cell with the lowest efficiency of 17.8% with a LPD stack consisting of a 440 nm thick SiO_x layer and a 320 nm thick SiO_xTiO_y layer (group 440/320).

observed, however, this areas are always close to the edges of the solar cells. All solar cells show a very homogeneous luminescence in the center area with a size of at least 55 cm^2.

For the analysis of the quantum efficiency (QE) data, the in-house solar cell analysis software SCAN was used. SCAN applies the QE model introduced by Brendel et al. [72], which is extended to account for free carrier absorption. The QE and reflectance measurements are done on a 2×2 cm^2 spot close to the center of the solar cells.

Figure 6.11(a) shows the measured spectrally resolved internal quantum efficiency (IQE) and the reflectance of the best solar cells of each group. The solar cells mainly show a difference in IQE in the long-wavelength range ($\lambda \geq 900$ nm), see Fig. 6.11(b). The increased IQE for the solar cell with the annealed LPD stack (group 600/280-anneal) for a wavelength below 400 nm is due to a measurement artifact, however, the IQE in this wavelength regime only contains information about the front side of the solar cell and is, therefore, not of interest for the evaluation of the rear side passivation quality.

By analytical modeling of the IQE and reflectance curves using the software SCAN, the effective rear surface recombination velocity S_{rear} and the internal rear reflectance R_{b} were deduced. All solar cells show a similar R_{b} of 0.91 ± 0.2. Thus for all investigated LPD capping layers, the rear reflectance can be considered as very good and on a par

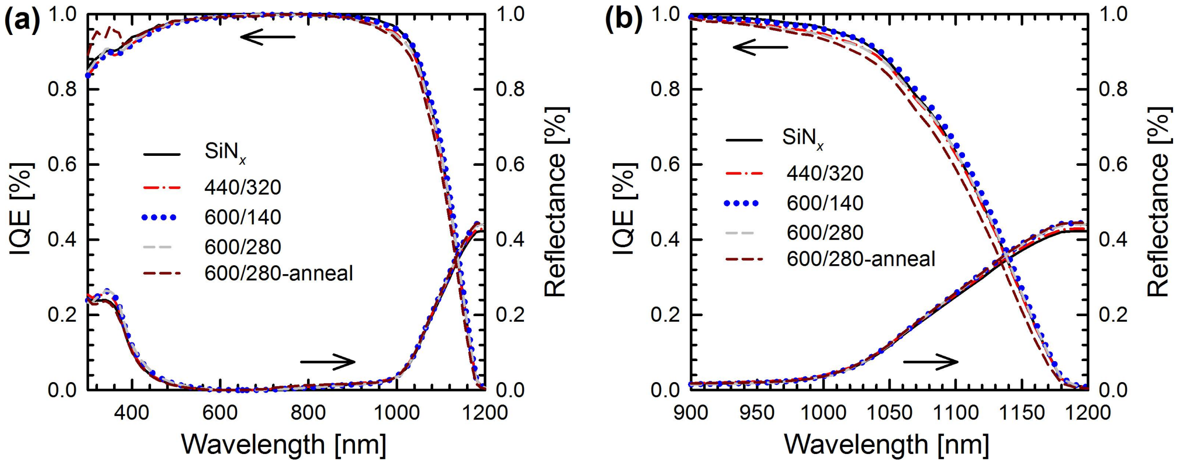

Figure 6.11: IQE and reflectance as a function of wavelength for the best PERC solar cells of each group. In (a) for a wavelength λ between 350 nm and 1200 nm and in (b) from 900 nm to 1200 nm. The measurement area is 2×2 cm^2 close to the center of the solar cells.

with the rear reflectance of the SiN$_x$ capping layer. The rear surface passivation quality is for all solar cells with an LPD capping layer reduced in comparison to the solar cells with SiN$_x$ capping. The SiN$_x$ capping results in an S_{rear} of (60 ± 20) cm/s. For the LPD capping layer the best rear surface passivation quality is provided by the LPD stack consisting of a 600 nm thick SiO$_x$ layer and a 140 nm thick SiO$_x$TiO$_y$ layer (group 600/140) with an S_{rear} of (100 ± 20) cm/s. For group 440/320 and 600/280 a S_{rear} of (180 ± 30) cm/s and (200 ± 30) cm/s is deduced, respectively. Interestingly, the highest S_{rear} is deduced for the solar cell with the highest efficiency (group 600/280-anneal) with an value of (230 ± 30) cm/s. For the SiN$_x$ capping and the LPD capping of group 600/140 the S_{rear} values are in good agreement with the lifetime samples, for the other three groups the S_{rear} values deduced from the IQE are higher than expected.

The EL-images and the IQE analysis show that the main reason for the lower efficiencies of the solar cells with LPD capping is not due to a generally poor rear surface passivation quality but due to inhomogeneities of the passivation and detaching of the Al on the rear. Both are probably mainly due to the spin-coating process used.

Since most of the problems due to the spin-coating are located at the edges, small (5×5 cm^2) solar cells are laser-cut out of the center region of the large-area solar cells, used are the solar cells with the lowest S_{rear} values for each group, except for group 600/280-anneal, since the cell with the lowest S$_{\mathrm{rear}}$ was not available during time of investigation. After the laser cutting, the edges are abraded and the solar cells are subsequently annealed for 10 min at 200 °C, in order to reduce the damage induced by

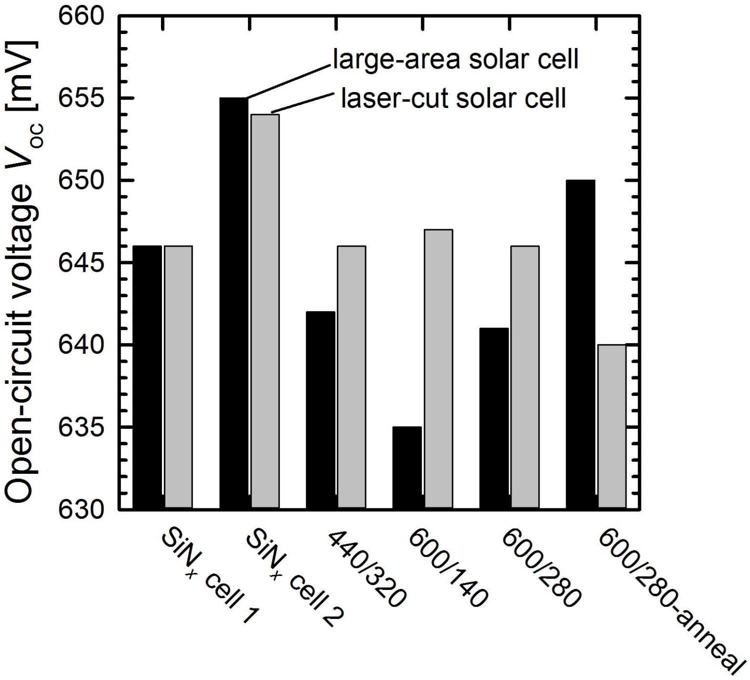

Figure 6.12: Open-circuit voltage V_{oc} of the large (15.6×15.6 cm^2) before and small (2.5×2.5 cm^2) PERC solar cells after laser cutting.

the laser cutting process.

For group SiN_x two solar cells are used, the solar cell with the lowest efficiency (SiN_x cell 1) and the solar cell with the highest efficiency (SiN_x cell 2), both show almost no change in V_{oc} due to the laser cutting, as can be seen in Fig. 6.12. The solar cells of Group 440/320, 600/140 and 600/280 show a strong increase in V_{oc} up to a value of 647 mV (group 600/140). The solar cell of group 600/28-anneal, however, shows a

Table 6.4: *I–V* parameters measured under standard testing conditions (STC) of the laser-cut 5×5 cm^2 *p*-type Cz-Si PERC solar cells using PA-ALD Al_2O_3/SiN_y and PA-ALD Al_2O_3 with different capping layers as rear side passivation, measured at ISFH. In brackets are the results for the large-area cells before the laser cutting.

Group	V_{oc} [mV]	J_{sc} [mA/cm^2]	FF [%]	η [%]
SiN_x cell 1	646 (646)	37.8 (38.2)	78.1 (79.1)	19.1 (19.5)
SiN_x cell 2	654 (655)	38.3 (38.7)	78.0 (79.6)	19.5 (20.2)
440/320	646 (642)	37.8 (37.2)	78.5 (77.2)	19.2 (18.4)
600/140	647 (635)	37.8 (37.3)	78.1 (77.7)	19.1 (18.4)
600/280	646 (641)	37.6 (37.0)	77.9 (77.7)	18.9 (18.4)
600/280-anneal	640 (650)	37.3 (38.0)	76.4 (78.6)	18.3 (19.4)

decrease in V_{oc}, which might be due to a damage during the handling or abrading or a low rear surface passivation quality in the center. The IQE of this solar cell shows an S_{rear} value of only (500±40) cm/s. The FF and J_{sc} are lower for all solar cells, since the grid design is not optimized for the small area, see Tab. 6.4. As a result, the efficiency is below 20% for the cells of all groups. These results show that the low efficiencies of the large-area solar cells can be mainly attributed to inhomogeneities during the spin-coating process.

6.4 Chapter summary

ICP-$\mathrm{AlO}_x/\mathrm{SiN}_y$ stacks and PA-ALD $\mathrm{Al_2O_3/SiN}_y$ stacks as rear surface passivation in PERC solar cells resulted in an average efficiency of (19.5±0.2)%, with the highest independently confirmed efficiency of 20.1% provided by an ICP-$\mathrm{AlO}_x/\mathrm{SiN}_y$ stack. Hence, ICP-AlO_x and PA-ALD $\mathrm{Al_2O_3}$ are both suitable for high efficiency solar cells.

Optimized PA-ALD $\mathrm{Al_2O_3}$/LPD stacks are capable of providing a rear surface passivation that is practically on a par with that of fully vacuum-processed PA-ALD $\mathrm{Al_2O_3/SiN}_x$ stacks. The best results for PERC solar cells with a PA-ALD $\mathrm{Al_2O_3}$/LPD stack are achieved for a LPD stack consisting of a 600 nm thick SiO_x layer in conjunction with a 280 nm thick $\mathrm{SiO}_x\mathrm{TiO}_y$ layer and an annealing step at 600 °C for 2 min, resulting in an efficiency of 19.8% for the best solar cell. In comparison, the best PERC solar cell with a PA-ALD/$\mathrm{Al_2O_3}$ stack processed in the same run achieved an efficiency of 20.2%. The difference in efficiency is mainly a result of the deposition process used that leads to an inhomogeneity of the passivation and partly detachment of the Al on the rear side. Hence, it can be expected that LPD capping layers, if deposited using a homogeneous deposition technique such as spray coating, would be a realistic option to replace vacuum-deposited SiN_x capping layers without significantly reducing the cell efficiency in next-generation industrial solar cells. However, more experimental optimization work is needed to implement LPD layers in a solar cell production process.

Chapter 7

Stability of the Al_2O_3 passivation under illumination

The stability of the front surface passivation under UV illumination is crucial for the long-term stability of solar modules. In the past, Lauinger et al. [73] reported that the SiN_x surface passivation degrades under direct UV exposure. In a photovoltaic (PV) module, the ethylene vinyl acetate (EVA) encapsulation and glass block the main part of the UV irradiance that could lead to a degradation of the passivation provided by the SiN_x. However, improved front emitters result in an increased blue response of the solar cell and, therefore, the application of EVAs with enhanced UV transmittance has gained interest in recent years [74, 75]. Consequently, a UV-stable passivation layer is crucial for high long-term stable module performance. Since the SiN_x passivation shows a pronounced degradation under UV illumination, alternative surface passivation schemes have to be evaluated, one is Al_2O_3. For PA-ALD Al_2O_3, excellent UV stability [76] and even an improvement of the passivation quality due to UV illumination have been reported [77]. This improvement is attributed to an improvement of the Q_f as Hezel et al. already reported for pyrolysis-grown Al_2O_3 exposed to UV illumination [2].

In this Chapter, we focus on the stability of silicon surface passivation schemes based on S-ALD Al_2O_3 in comparison to the standard PECVD-SiN_x passivation using lifetime measurements and Corona-lifetime analysis. Special attention is paid to the impact of the thermal pre-treatments of the passivation layers, including a fast-firing step.

	A: Single Al_2O_3		B: Al_2O_3/SiN_x		C: Single SiN_x
1st layer	Al_2O_3		Al_2O_3		SiN_x
2nd layer			SiN_x		
activation	(i) annealing	(ii) firing	none	(ii) firing	(ii) firing

Figure 7.1: Surface passivation and activation procedures applied for the three different dielectric passivation layers.

7.1 Experimental details

7.1.1 Sample preparation

We use Ga-doped p-type Cz-Si wafers with a resistivity of 0.9 Ωcm. This material shows no light-induced degradation of the bulk lifetime [78]. For the phosphorus-diffused n^+-emitter samples, boron-doped p-type FZ-Si wafers with a resistivity of 200 Ωcm are used and for the boron-diffused p^+-emitter samples, phosphorus-doped n-type Cz-Si wafers with a resistivity of 5 Ωcm are used. All Cz-Si samples are KOH-etched in order to remove the saw damage and subsequently all samples are RCA-cleaned. The n^+-emitters and the p^+-emitters are both formed in a quartz-tube furnace and a final sheet resistance of (90±8) Ω/sq is measured for both diffusions.

The Ga-doped Cz-Si lifetime samples have a final thickness of (165±5) µm and are subdivided into three groups, see Fig. 7.1. The following passivation layers were deposited on both wafer surfaces: for group (A) a single S-ALD Al_2O_3 layer, 5 nm thick if not otherwise stated, for group (B) a 5 nm thick S-ALD Al_2O_3 layer as bottom layer and a 100 nm thick SiN_x layer on top, and for group (C) a 100 nm thick single SiN_x layer. The SiN_x layers have a refractive index of $n = 2.05$ (at $\lambda = 633$ nm) and are deposited by PECVD using a SiNA system (Meyer Burger).

The surface passivation is activated either by (i) a fast-firing step or (ii) a low-temperature annealing step. The fast firing step (i) is performed using a belt speed of 6.8 m/min and a set-peak temperature of 850 °C. For the annealing step (ii) different annealing temperatures ranging from 350 to 550 °C were used.

In case of group (A), the passivation was activated during the fast firing step (i) or the low-temperature annealing step (ii). For the samples of group (B), the fast firing step (i) or no extra activation step were performed. The samples of group (C) received only the fast-firing step (i). Subsequently, the wafers were laser-cut into 3.9×3.9 cm^2 samples to diminish the impact of the edges.

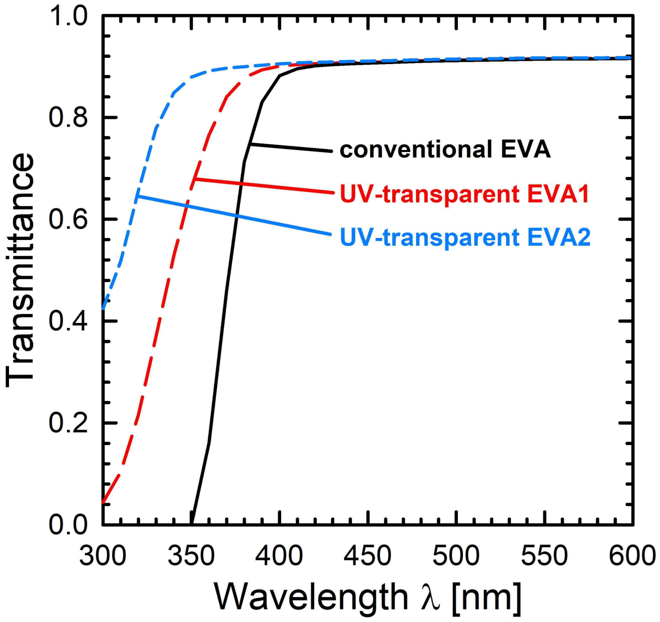

Figure 7.2: Transmittance vs wavelength for three different EVAs under the same low-iron float glass.

Previous experiments with low-temperature-annealed PA-ALD Al_2O_3 had shown that the passivation quality can be enhanced by UV irradiation [77]. However, (i) the optimal annealing temperature is different for PA-ALD Al_2O_3 and S-ALD Al_2O_3, typically 425 °C for PA-ALD Al_2O_3 and only 350 °C for S-ALD Al_2O_3 and (ii) the optimal annealing time is longer at the same annealing temperature for the PA-ALD Al_2O_3 layers (typically 15 min at 425 °C compared to 2 min for S-ALD Al_2O_3 layers, see Chapter 4). Therefore, another experiment is conducted with 15 nm thick S-ALD Al_2O_3 layers and a variation of the annealing temperature between 350 and 550 °C with the annealing time chosen to be optimal for each temperature.

The boron-diffused p^+-emitter samples are passivated using the same passivation schemes as in group (A) (Al_2O_3 single layers) with activation steps (i) and (ii) and group (B) (Al_2O_3/SiN_x stacks) applying activation step (i). These samples are labeled n/p^+ in the following. The phosphorus-diffused n^+-emitter samples are passivated using the same SiN_x as used in group (C) and the activation step (i). These samples are labeled p/n^+.

The samples are placed inside a UV chamber either without any cover or with a cover consisting of an EVA foil laminated on top of a low-iron float glass. Two EVA foils (EVASKY, Bridgestone S87) with different short-wavelengths cut-off are used, called EVA1 and EVA2, respectively. The calculated transmittance of the stack consisting of each foil on top of the low-iron float glass in comparison to a conventional EVA foil on top of the same glass are shown in Fig. 7.2. The transmittance is calculated using the ray-tracing software Daidalos [79] with refractive index data for EVA [75] and low-iron float glass [80]. For the undiffused samples EVA1 and for the diffused samples EVA2 is used.

In order to differentiate between the impact of UV photons and visible/infrared photons, some samples are not illuminated using the UV lamp but a conventional halogen lamp. The samples are illuminated with an intensity equivalent to (1±0.1) sun and are kept at (75±10) °C during the illumination. For a comparison of the spectrum of the UV lamp and the halogen lamp see Fig. 3.10. Most of the emitted power of the halogen lamp is in the visible or infrared, however, still 0.14% of the emitted power is in the UV range.

7.1.2 Sample characterization

The effective surface recombination velocity S_{eff} deduced from lifetime measurements can be separated into the contributions of the front (S_{front}) and the rear side (S_{rear}) according to $S_{\text{eff}} = (S_{\text{front}} + S_{\text{rear}})/2$. Since the rear side is not illuminated with UV photons, it can be assumed that S_{rear} is not changed during the experiment and, therefore, S_{rear} can be identified with the initially extracted S_{eff} value. This increases the uncertainty in the extracted S_{front}, as the rear passivation might slightly change over the long time span of the experiment. This uncertainty, however, is quite small compared to the changes induced by the UV illumination at the front, since samples that are kept in the dark over the entire duration of the experiments show only a variation inside the uncertainty range of ±10%. Only the samples with the low-temperature annealed Al_2O_3 layers show a slight degradation from $S_{\text{eff}} = 13$ cm/s to $S_{\text{eff}} = 16$ cm/s after 2184 hours storage in the dark. For large S_{front} values (> 1000 cm/s), Eq. (2.31) is not valid and it would be more accurate to make the assumption that S_{rear} equals 0, which would require to replace W in Eq. (2.31) by $2W$ [41]. For large $S_{\text{eff}} > 1000$ cm/s, the assumption $S_{\text{rear}} = 0$ is, therefore, used and W in Eq. (2.31) is replaced by $2W$ in order to calculate the S_{front} values. The emitter saturation current density ($J_{0\text{E}}$) is extracted from injection-dependent lifetime measurements using the method of Kane and Swanson [81] with the recent adaption by Blum et al. [82].

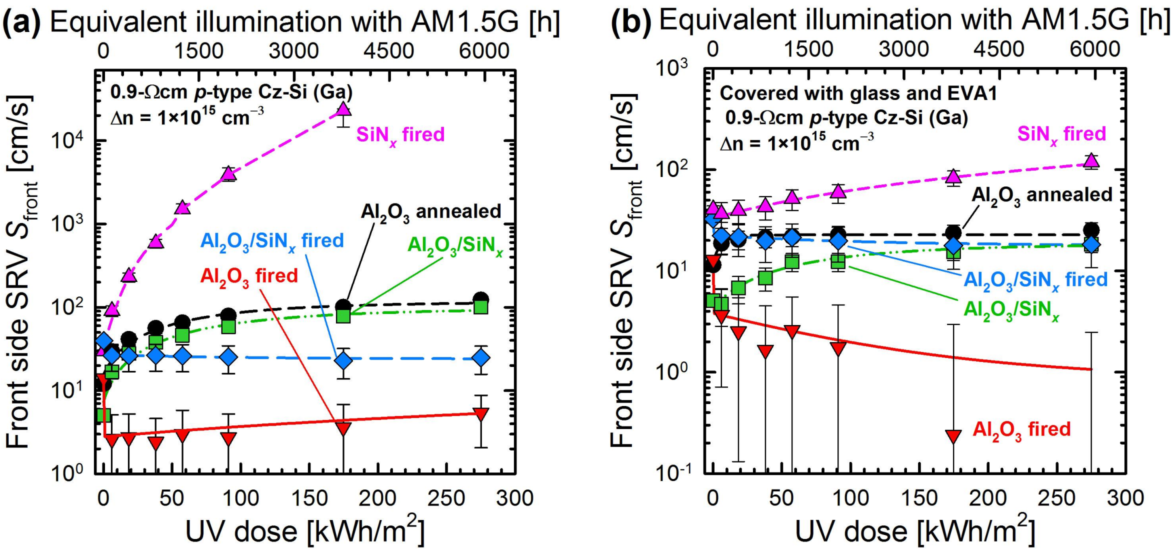

Figure 7.3: Front side SRV S_{front} vs UV dose for undiffused samples (a) not covered and (b) covered with glass and EVA1 during UV illumination. Also shown is the equivalent illumination duration with the AM1.5G spectrum. The lines are guides to the eyes.

7.2 Results and discussion

7.2.1 UV illumination of undiffused samples

Figure 7.3(a) shows the evolution of S_{front} for UV-illuminated samples that are not covered. The samples in Fig. 7.3(a) show three different trends: First, the sample with only SiN_x shows a strong degradation in S_{front} from a value of 30 cm/s to 23000 cm/s after receiving a UV dose of 175 kWh/m^2 (corresponding to approximately 5 months of continuous equivalent AM1.5G illumination). This increase in the S_{front} of SiN_x-passivated silicon surfaces under UV illumination is in good agreement with reports in the literature [73]. The second group of samples consisting of the low-temperature-annealed (350 °C) $\mathrm{Al_2O_3}$ single-layer and the non-fired $\mathrm{Al_2O_3/SiN}_x$ stack show a moderate degradation in S_{front}, starting at 12 cm/s and 5 cm/s, respectively, and resulting in stabilized S_{front} values of 122 cm/s and 100 cm/s, respectively, after a UV dose of 275 kWh/m^2 (corresponding to ~8 months of continuous AM1.5G illumination). The third group consisting of the fired $\mathrm{Al_2O_3}$ single-layer and the fired $\mathrm{Al_2O_3/SiN}_x$ stack show an enhancement of the surface passivation quality during UV illumination. The S_{front} value of the fired $\mathrm{Al_2O_3/SiN}_x$ stack improves during UV illumination from 40 cm/s directly after firing to 25 cm/s after receiving a UV dose of 275 kWh/m^2. The surface passivation quality of the fired $\mathrm{Al_2O_3}$ layer is also initially enhanced, however, after receiving a UV dose of 91 kWh/m^2 S_{front} increases again, resulting in an S_{front} of 6 cm/s after receiving the maximum UV dose in this experiment of 275 kWh/m^2.

Figure 7.3(b) shows the results for the undiffused samples covered with glass and the UV-transparent EVA1, which acts as a UV filter (see Fig. 7.2). All samples show qualitatively the same behavior as the samples without a glass and EVA cover. However, the degradation in S_{front} is less pronounced. The sample with the SiN_x layer shows an increase of S_{front} from initially 41 cm/s to 119 cm/s after receiving the maximum UV dose of 275 kWh/m^2. The samples with the low-temperature-annealed (350 °C) Al_2O_3 single-layer and the non-fired Al_2O_3/SiN_x stack also show an increase in the S_{front} values from initially 11 cm/s and 5 cm/s, respectively, towards maximal values of 25 cm/s for the annealed Al_2O_3 single-layer and 18 cm/s for the Al_2O_3/SiN_x stack. The samples passivated with Al_2O_3 that have been fired in the belt-furnace show again an improvement in surface passivation quality due to the UV illumination. For the fired Al_2O_3 single-layer this results in a reduction of the S_{front} value from 13 cm/s to a value below 1 cm/s and for the fired Al_2O_3/SiN_x stack from 33 cm/s to a value of 18 cm/s. In contrast to the sample that is not covered with glass and EVA (see Fig. 7.3(a)), the fired Al_2O_3 single-layer sample does not show any significant decrease in the passivation quality during UV illumination. This suggests that the short-wavelengths UV ($\lambda <$ 350 nm), which is partly blocked by the glass and EVA1, is responsible for the weak degradation observed in the sample without cover and the long-wavelengths UV (λ between 350 and 400 nm) improves the passivation quality of the fired Al_2O_3.

7.2.2 Impact of annealing temperature and Al_2O_3 layer thickness

Figure 7.4(a) shows the evolution of S_{front} of the samples that were not covered during UV illumination. For a low UV dose of 7 kWh/m^2 the passivation quality improves for the samples annealed at 550 °C, however, still all samples show a degradation in the surface passivation quality on the long term. After receiving the maximum UV dose of 688 kWh/m^2, the sample annealed at 550 °C shows the lowest S_{front} of 24 cm/s and the other samples, annealed at lower temperatures, show S_{front} values between 35 and 40 cm/s.

Experiments conducted with samples annealed for a longer period (the annealing times applied were three times longer than the optimal period) show that the degradation under UV is less pronounced. However, a longer annealing step has only a small

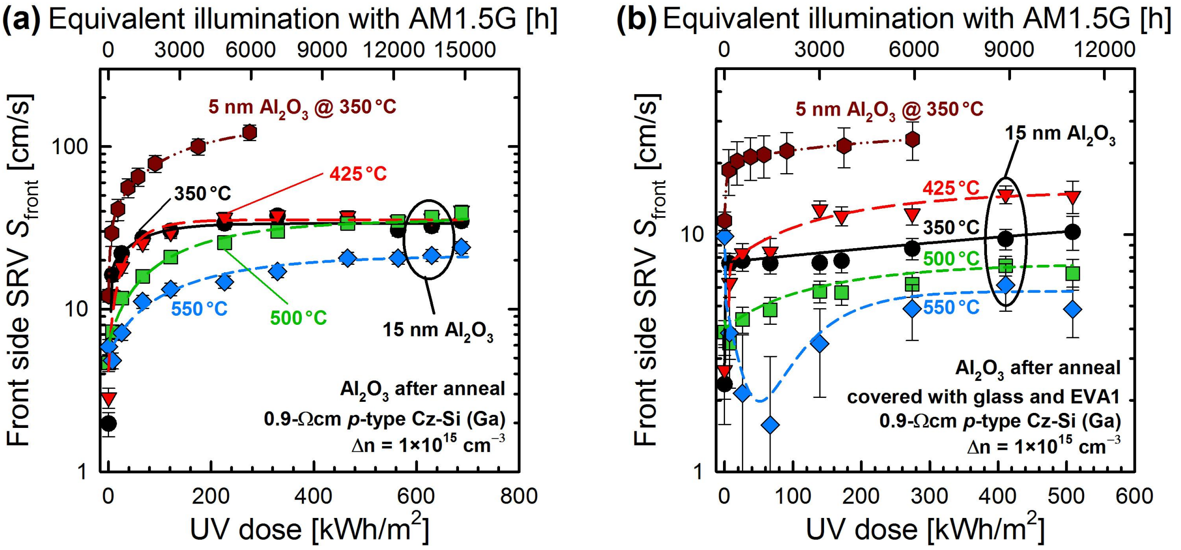

Figure 7.4: Front side SRV S_{front} vs UV dose for undiffused samples passivated with a 15 nm S-ALD Al_2O_3 layers that received an annealing step on a hotplate at different temperatures. (a) Not covered and (b) covered with glass and EVA1 during UV illumination. Also shown is the equivalent illumination duration with the AM1.5G spectrum. The lines are guides to the eyes.

impact, resulting in S_{front} values for all annealing temperatures below 33 cm/s, which are, therefore, lower than the S_{front} values from the samples in Fig. 7.4(a).

All measured S_{front} values on the samples with a 15 nm thick Al_2O_3 layer are significantly lower than the S_{front} value of 120 cm/s of the sample with a 5 nm thick Al_2O_3 layer after receiving a UV dose of 275 kWh/m^2. This result shows that thicker Al_2O_3 layers and higher annealing temperatures improve the UV stability significantly. Still, the surface passivation of annealed S-ALD Al_2O_3 slightly degrades on the long term. To further enhance the UV stability, annealing at even higher temperatures has to be evaluated, since the 5 nm thick fired Al_2O_3 single-layers show only a negligible degradation. The impact of a SiN_x capping layer has also to be evaluated, as for the application to solar cells, Al_2O_3/SiN_x stacks are most relevant.

Figure 7.4(b) shows the results for undiffused samples with 5 and 15 nm thick Al_2O_3 layers and various annealing temperatures. All samples are covered with glass and EVA1. The surface passivation of all samples shows a very weak long-term degradation due to the UV exposure. However, the S_{front} values of all samples with a 15 nm thick Al_2O_3 layer saturate below 15 cm/s after receiving a UV dose of 509 kWh/m^2. The sample annealed at 550 °C even shows initially a strong decrease in S_{front} from 10 to 2 cm/s. This is a similar behavior as has been observed on the fired single Al_2O_3 layers. With further increasing UV dose, the S_{front} increases again, however, it saturates at a

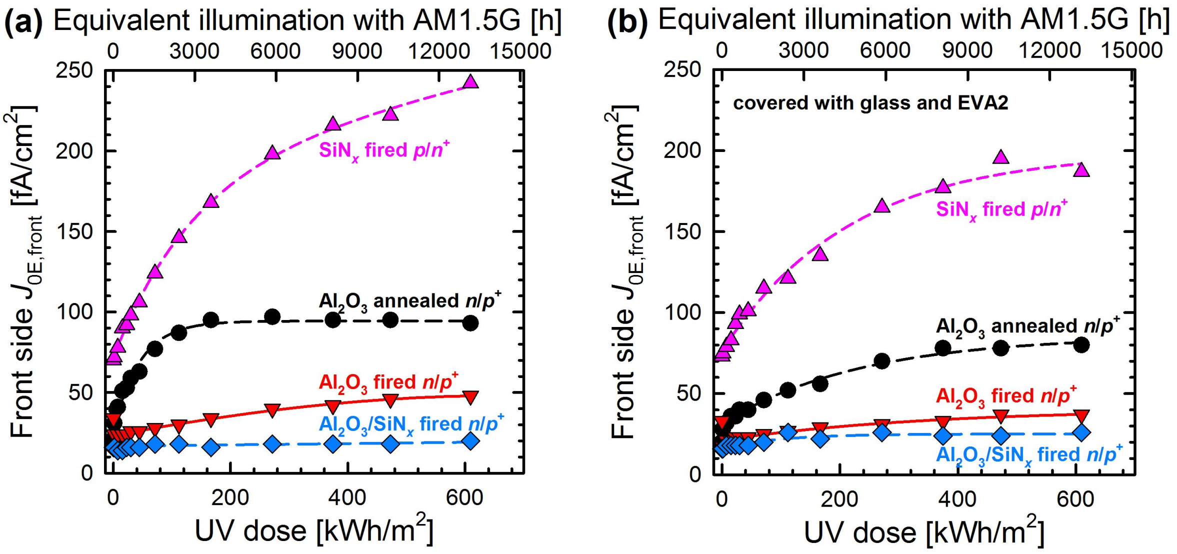

Figure 7.5: Front side emitter saturation current density $J_{0E,\text{front}}$ vs UV dose for diffused samples that are (a) not covered and (b) covered with glass and EVA2 during UV illumination. Also shown is the equivalent illumination duration with the AM1.5G spectrum. The lines are guides to the eyes.

very low S_{front} value below 7 cm/s.

7.2.3 UV illumination of diffused samples

Figure 7.5(a) shows the results of diffused n^+ and p^+-samples that were not covered during UV exposure. The SiN$_x$-passivated p/n^+ sample shows a pronounced increase in $J_{0E,\text{front}}$ up to a value of 242 fA/cm^2 after a UV dose of 609 kWh/m^2. The n/p^+ sample sample with a 5 nm thick low-temperature (350 °C) annealed Al_2O_3 single-layer also shows a degradation to a stable $J_{0E,\text{front}}$ value of 95 fA/cm^2. For the fired Al_2O_3 single-layer, first the $J_{0E,\text{front}}$ decreases after a UV dose of 1.3 kWh/cm^2 from initially 34 fA/cm^2 to 24 fA/cm^2 and then shows an increase in $J_{0E,\text{front}}$ to a value of 48 fA/cm^2. The $J_{0E,\text{front}}$ value provided by the fired Al_2O_3/SiN$_x$ stack only varies around 18 fA/cm^2 in the uncertainty range of the PCD measurement and can, hence, be regarded as perfectly UV stable.

The diffused samples covered with EVA2 and glass during UV exposure do not show any significant difference to the samples without cover, see Fig. 7.5(b). This is partly due to the fact that most of the UV light is transmitted through the EVA2.

This experimental results clearly demonstrate that the Al_2O_3 passivation and in particular the Al_2O_3/SiN$_x$ stacks are excellently suited for the front-side passivation of the p^+ emitter of a screen-printed solar cell, were a firing step is required.

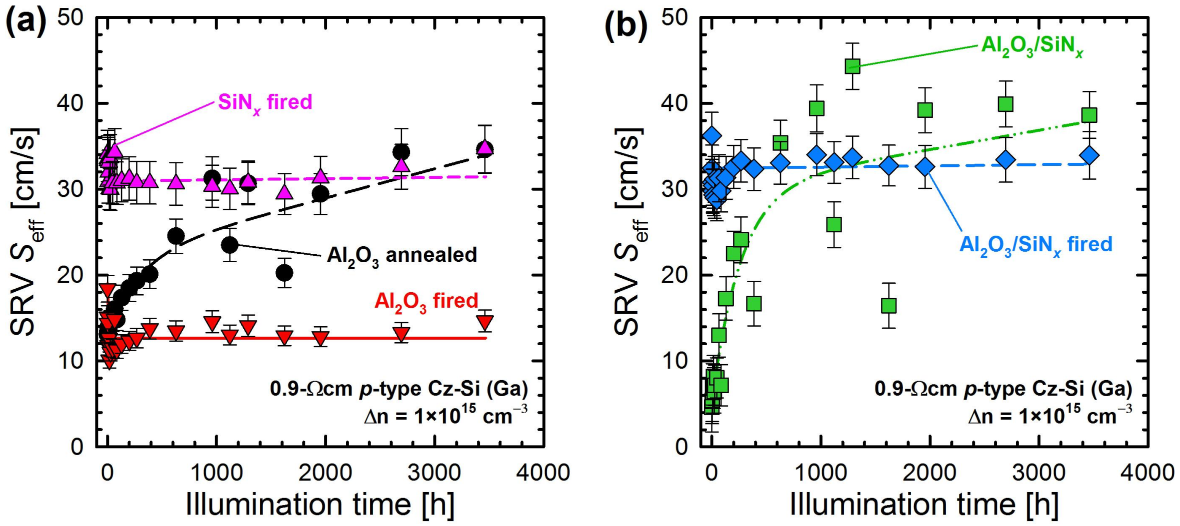

Figure 7.6: SRV S_{eff} vs illumination time with halogen lamps for undiffused samples. The samples in (a) are passivated with annealed or fired Al_2O_3 single layers or with a fired SiN_x single layer. The samples in (b) are passivated with an Al_2O_3/SiN_x stack and received a firing step or no extra activation step. All samples are illuminated with a power of (1±0.1) sun at (75±10) °C. The lines are guides to the eyes.

7.2.4 Impact of halogen-lamp illumination

Figure 7.6 shows the S_{eff} results for the undiffused samples that are illuminated using a halogen lamp. The samples with the annealed Al_2O_3 layer, shown in Fig. 7.6(a), and the non-fired Al_2O_3/SiN_x stack, shown in Fig 7.6(b), show a degradation of the passivation quality. This degradation is even more pronounced than observed for samples that are covered with glass and EVA1 during UV illumination, see Fig. 7.3(b). However, the S_{front} values also show a strong scattering. The sample with the fired Al_2O_3 layer shows an improvement due to the illumination in the first 7 hours from an initial S_{eff} value of 18 cm/s to a stabilized value of 12 cm/s. This improved surface passivation is stable over time. For the samples with the fired Al_2O_3/SiN_x stack and the fired SiN_x layer, the measured lifetimes only change within the uncertainty ranges.

This result suggests that the observed degradation of the annealed Al_2O_3 layer and the non-fired Al_2O_3/SiN_x stack under UV illumination is partly induced by light with an energy below 3.4 eV ($\lambda > 365$ nm), whereas the fired Al_2O_3 and fired SiN_x is only affected by light with a higher energy.

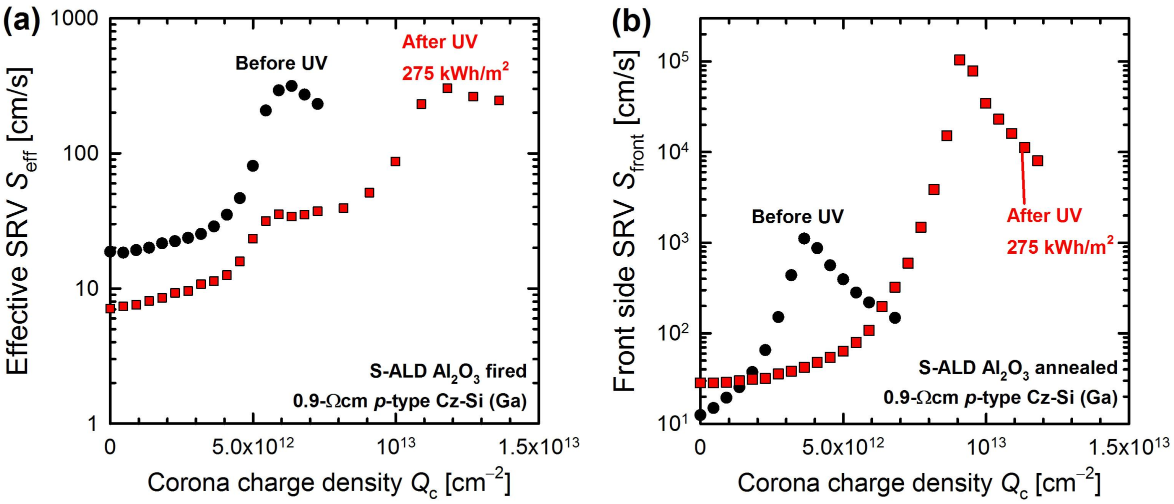

Figure 7.7: (a) Effective SRV S_{eff} vs Corona charge density Q_c for undiffused samples passivated with fired S-ALD Al_2O_3 single layer, before illumination (black circles) and after receiving a UV dose of 275 kWh/m^2 (red squares). (b) Front side SRV S_{front} vs Corona charge density Q_c for undiffused samples passivated with annealed Al_2O_3 single layer, before illumination (black circles) and after receiving a UV dose of 275 kWh/m^2 (red squares). All UV samples are covered with glass and EVA1 during UV illumination.

7.2.5 Fixed charge density within the Al_2O_3 layer

For the Corona-lifetime measurement only Al_2O_3 layer with a thickness of 5 nm are used. It has to be noted that the samples illuminated for 3460 h using the halogen lamp are not measured directly after illumination but after 418 days of storage in the dark.

The samples characterized using the Corona-lifetime measurement are, due to the illumination of the front side, not symmetrically passivated any more. This has an impact on the Corona-lifetime measurement as can be seen in Fig. 7.7(a). For the Corona-lifetime measurements shown in Fig. 7.7(a) the Corona charge is deposited on both sample surfaces. The symmetrical deposition of Corona charges results in a single peak of the S_{eff} values for the fired Al_2O_3 single layer before UV illumination at $Q_c = 6.4{\times}10^{12}$ cm^{-2}. For the fired Al_2O_3 single layer after UV illumination, in contrast, two peaks are observed, a small peak at $Q_c = 5.9{\times}10^{12}$ cm^{-2} resulting from the rear side fixed charge density and a second peak at $Q_c = 1.2{\times}10^{13}$ cm^{-2} resulting from the front side fixed charge density. For this sample the extraction of the Q_f values for both sides is possible, however, in order to extract the S_0 value of the UV-illuminated side a reference measurement is necessary. Hence, for all other illuminated samples the Corona charges are only deposited on the front side. Figure 7.7(b) shows Corona-lifetime measurements

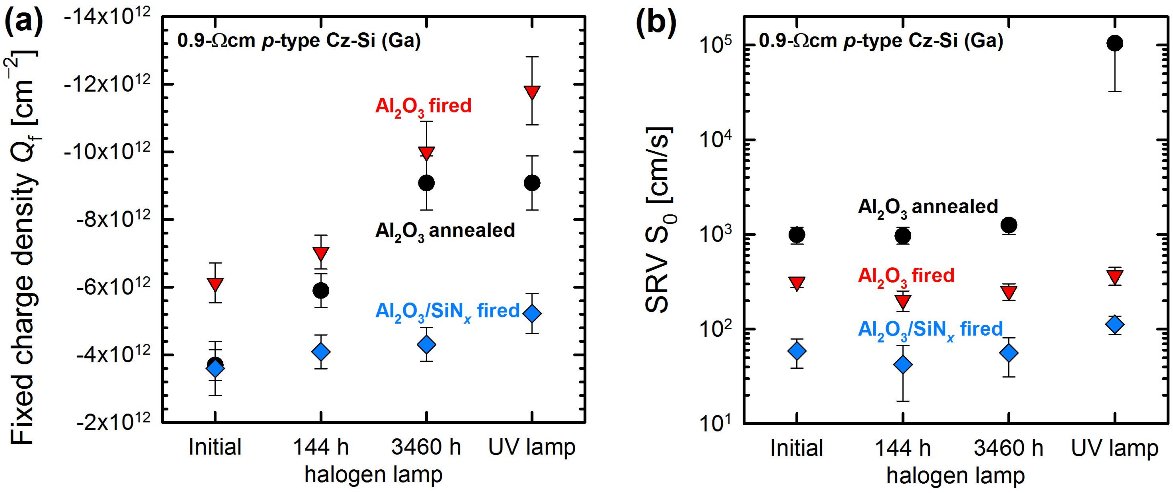

Figure 7.8: (a) Fixed charge density Q_f and (b) SRV S_0, both deduced from Corona-lifetime measurement for S-ALD Al_2O_3-passivated undiffused samples before illumination, after 144 h and after 3460 h halogen-lamp illumination ((1±0.1) sun at (75±10) °C) and after receiving a UV dose of 275 kWh/m^2. The UV samples are covered with glass and EVA1 during UV illumination.

of annealed S-ALD Al_2O_3 single layer before and after UV illumination. Both samples show a single peak in S_front, that is shifted to a larger Q_c value for the UV illuminated sample. The extracted Q_f values from all Corona-lifetime measurement can be seen in Fig. 7.8(a). The corresponding S_0 values can be seen in Fig. 7.8(b).

For the samples passivated with a fired Al_2O_3/SiN_x stack, Q_f shows no variation during halogen-lamp illumination within the measurement uncertainty range. For the UV-illuminated fired Al_2O_3/SiN_x sample, an increase in the negative Q_f from $-(3.6\pm0.8)\times10^{12}$ cm^{-2} to $-(5.2\pm0.6)\times10^{12}$ cm^{-2} is observed. All examined samples with an Al_2O_3 single-layer show a more pronounced increase of the negative Q_f due to illumination, as shown in Fig. 7.8(a). The illumination with the halogen lamp leads to an increase in the negative Q_f from $-(3.7\pm0.5)\times10^{12}$ cm^{-2} to $-(9.1\pm0.8)\times10^{12}$ cm^{-2} for the annealed Al_2O_3, while for the fired Al_2O_3 single-layers the negative Q_f increases from $-(6.1\pm0.6)\times10^{12}$ cm^{-2} to $-(10\pm0.9)\times10^{12}$ cm^{-2}. After a UV dose of 275 kWh/m^2, the increase is similar for the annealed Al_2O_3 single-layer and more pronounced for the fired Al_2O_3 single-layer, resulting in a Q_f of $-(11.8\pm1)\times10^{12}$ cm^{-2} for the fired Al_2O_3 layers. This increase is already triggered by only a small UV dose since the full increase in Q_f can be measured already after a dose of 50 kWh/m^2 and for the annealed Al_2O_3 already after a UV dose of 1kWh/m^2, as can be seen in Fig. 7.9. For the fired Al_2O_3 layer this small dose results in a Q_f of $-(9.5\pm0.8)\times10^{12}$ cm^{-2}. This suggests that the increase in Q_f is slower for the fired Al_2O_3 as can also be seen for the samples illumi-

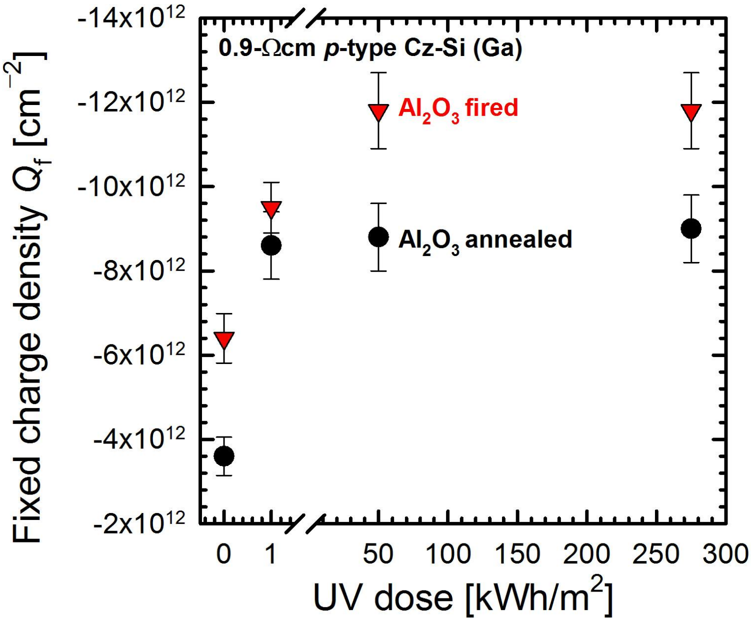

Figure 7.9: Fixed charge density Q_f vs UV dose for undiffused samples covered with glass and EVA1 during UV illumination.

nated with a halogen lamp. Hence, a UV dose of ~5 kWh/m^2 should be sufficient for the full increase if the increase in Q_f follows an exponential rise to the maximum. The increase in Q_f is very stable over time. Samples measured after 332 days storage in the dark show the same high Q_f as samples measured directly after UV illumination. For the samples illuminated with a halogen lamp the stability was not investigated.

An increase in $|Q_f|$ due to illumination has been reported before [33, 83]. Gielis et al. [33] showed that for PA-ALD Al_2O_3 the irradiation with a laser increases $|Q_f|$ and extracted a photon energy of 3.12 eV ($\lambda = 400$ nm) as threshold for the injection of charge. Gielis et al. [33] suggested a direct transition of charge carriers from the silicon valence band into the Al_2O_3 conduction band. The electrons in the Al_2O_3 conduction band diffuse into traps inside the Al_2O_3 layer [33]. Liao et al. [83] observed that also a de-trapping occurs after the illumination is switched of. In our experiment we observe no de-trapping of the charges and the increase in $|Q_f|$ of our samples is stable over time. However, our experimental findings are in good agreement with the threshold photon energy of 3.12 eV and can explain the long halogen-lamp illumination time needed in order to measure Q_f values that are similar to the Q_f values measured after UV illumination. From the measured spectral irradiance of the halogen lamp, see Fig. 3.10, we deduce that 3460 hours of illumination with a halogen lamp is equivalent to a UV dose of almost 4 kWh/m^2. For the UV illuminated samples we measure already after a

UV dose of 1 kWh/m^2 similar Q_f values as after the halogen-lamp illumination.

The increase in $|Q_\mathrm{f}|$ explains the increase in the passivation quality for our fired Al_2O_3-passivated samples. However, the samples passivated with a low-temperature annealed Al_2O_3 single-layer show a decrease in the passivation quality. We attribute this reduction to a reduced chemical passivation, as can be seen by an increase of the S_0 values, see Fig. 7.8(b). Our fired samples showed no significant increase in S_0. The annealed samples that were illuminated for 3460 h using the halogen lamp showed only a small increase in S_0 by a factor of 1.3 ± 0.2. For sufficiently high negative Q_f values, the equation $S_\mathrm{eff} \sim S_0/Q_\mathrm{f}^2$ is valid [84]. Since the $|Q_\mathrm{f}|$ increases, the increase in S_0 cannot explain the degradation in S_eff for the samples illuminated with the halogen lamp. Under UV illumination with a dose of 275 kWh/m^2, however, our samples showed an increase in S_0 by a factor of more than 30 and in $|Q_\mathrm{f}|$ by a factor of 3, which would explain the increase in surface recombination velocity by a factor of more than 3. The measured increase is a factor of 2.5 ± 0.9 and, therefore, less pronounced than expected from the S_0 and Q_f measurements. The discrepancy between these two values could be explained by two reasons: (i) as bulk lifetime only the intrinsic lifetime was taken into account, a lower bulk lifetime would lead to a higher increase in S_eff, (ii) the minimal measured τ_eff value of 3.41 µs is close to the lower (diffusion-limited) lifetime limit of 3.26 µs, therefore, a small uncertainty in the measurement leads to a large change of the deduced S_0. Nevertheless, our results unambiguously show that the interface between Al_2O_3 and crystalline silicon degrades during UV exposure and the strong increase in $|Q_\mathrm{f}|$ partly compensates the degradation.

7.3 Chapter summary

Undiffused c-Si samples passivated with S-ALD Al_2O_3 showed a much better UV stability compared to PECVD-SiN_x. We were able to identify three different typical behaviors for Al_2O_3-passivated *p*-type silicon samples. The samples treated with a low-temperature annealing step showed continuous degradation until saturation, whereas the samples that received a firing step degraded only after exposure to a very high UV dose. For the annealed Al_2O_3, higher annealing temperatures and Al_2O_3 thicknesses improved the UV stability, starting with S_front values of 6 cm/s and saturating at 24 cm/s after complete UV degradation without any glass and EVA cover.

In the case of the fired Al_2O_3/SiN_x stacks, no degradation was observed under UV exposure. This behavior was also observed on p^+ diffused samples, were the fired

Al_2O_3/SiN_x stacks showed a highly UV-stable passivation with saturation current densities J_{0E} of 18 fA/cm^2.

Under illumination with a halogen lamp, only the samples passivated with low-temperature annealed Al_2O_3 single-layers and non-fired Al_2O_3/SiN_x stacks showed a degradation. Thus, it can be concluded that for the SiN_x and the fired Al_2O_3 single-layer, photons with an energy above 3.4 eV are required to reduce the passivation quality.

Corona-lifetime analyses, conducted with UV- and halogen-lamp-illuminated samples revealed the reasons for an enhancement or degradation of the surface passivation quality, respectively. It was observed that the negative fixed charge density Q_f within the fired S-ALD Al_2O_3 single layer was enhanced to values larger than -1×10^{13} cm^{-2} after a short UV exposure, explaining the improvement in passivation quality. In contrast, for the low-temperature-annealed S-ALD Al_2O_3, we measured an increase in $|Q_\mathrm{f}|$ to a value of $-(9.1\pm0.8)\times10^{12}$ cm^{-2} but also a strong increase in S_0, which explains the degradation over time.

Samples illuminated with a halogen lamp with only a small UV fraction in the spectrum, also showed a strong increase in $|Q_\mathrm{f}|$ with only small changes in S_0. The increase in S_0, however, is on a long timescale, which suggests that UV-induced interface states are created, which continuously increase S_0.

In conclusion, our results suggest that the use of Al_2O_3, e.g., on p^+ front emitters of n-type silicon solar cells, and in particular Al_2O_3/SiN_x stacks lead to a significant improvement in the long-term stability of PV modules due to the excellent UV stability of the Al_2O_3/SiN_x passivation in contrast to the relatively unstable SiN_x passivation as used on n^+ emitters in the majority of today's industrial solar cells. Application of UV light could also be used in the future to further improve the passivation quality of Al_2O_3 due to the increase in $|Q_\mathrm{f}|$.

Chapter 8

Conclusions and outlook

In this thesis, different aspects of the silicon surface passivation provided by Al_2O_3 were investigated, from the fundamental understanding of the surface passivation, especially on n-type silicon wafers, to the implementation into PERC solar cells.

For the deposition of Al_2O_3, three different deposition techniques were evaluated, (i) PA-ALD, (ii) S-ALD, and (iii), for the first time, ICP-PECVD. It was shown that low-temperature-annealed Al_2O_3 can provide an excellent level of surface passivation with S_{eff} values below 2 cm/s for PA-ALD and S-ALD Al_2O_3 and below 6 cm/s for ICP-AlO_x on 1.4-Ωcm p-type FZ-Si. The interface state density D_{it} was found to be larger for the ICP-AlO_x layer, explaining the slightly higher S_{eff} values, whereas the negative fixed charge density Q_{f} is for all applied deposition techniques in the range of $-(4\pm1)\times10^{12}$ cm^{-2}.

The surface passivation quality provided by Al_2O_3 layers subject to a high-temperature fast-firing step, as applied in the metal contact formation in industrial solar cell production, was investigated. The best results were achieved using a SiN_x layer as capping layer for the Al_2O_3 layers. For PA-ALD Al_2O_3/SiN_x stacks, an excellent surface passivation with S_{eff} values of 1 cm/s were achieved on 1.4-Ωcm p-type FZ-Si and on 3-Ωcm n-type Cz-Si, whereas S-ALD Al_2O_3/SiN_x stacks provided a slightly lower surface passivation quality with S_{eff} values between 2 and 3 cm/s on 3-Ωcm n-type Cz-Si and the ICP-AlO_x/SiN_y stacks below 7 cm/s on 1.4-Ωcm p-type FZ-Si. For the standard firing conditions, it was shown that the passivation quality is only slightly improved by the addition of SiN_x as capping layer for the Al_2O_3. However, for very thin PA-ALD Al_2O_3 layers ($\leq$ 10 nm) and a harsher firing, it was shown that the PA-ALD Al_2O_3/SiN_x stacks still provide an excellent passivation quality, whereas the single PA-ALD Al_2O_3 layers show a reduced passivation quality. Further experiments showed that this reduced passivation quality can be partly recovered applying a post-firing anneal (425 °C for 15 min) or by illumination. The illumination-induced recovery of the passivation quality was found to be dependent on intensity and temperature.

The impact of the SiN_x capping layer on the surface passivation provided by $\mathrm{Al_2O_3}$ was also investigated for the case of low-temperature-annealed S-ALD $\mathrm{Al_2O_3}$. This layer stack was evaluated on textured undiffused 3-Ωcm n-type Cz-Si samples and it was shown that the annealing prior to the SiN_x deposition is beneficial for the surface passivation, leading to S_{eff} values as low as 5 cm/s for 5 nm thick $\mathrm{Al_2O_3}$ layers annealed at 500 °C. However, a post-deposition anneal at 500 °C improves the surface passivation to S_{eff} values below 3 cm/s, almost independently of the annealing step prior to the SiN_x deposition. Hence, a supplementary annealing after SiN_x deposition is advantageous to achieve an optimal surface passivation quality.

The cause for the injection dependence of the effective surface recombination velocity $S_{\mathrm{eff}}(\Delta n)$ of n-type c-Si wafers passivated using PA-ALD $\mathrm{Al_2O_3}$ below an injection density of 10^{15} cm^{-3} was deduced. The injection dependence was shown to be caused by the conductance of the holes through the inversion layer, induced by the negative fixed charge density within the $\mathrm{Al_2O_3}$ layer, and simultaneously of the electrons through the base, from the measurement area to areas of high recombination. The main areas of high recombination were shown to be the wafer edges, however, we additionally found that also areas of high recombination on the sample surfaces have a strong impact on the injection dependence of $S_{\mathrm{eff}}(\Delta n)$. This effect, especially the areas of poor passivation, were further found to not only influence the S_{eff} at injection densities below 10^{15} cm^{-3} but also up to 10^{16} cm^{-3}.

By avoiding areas of poor surface passivation quality on the sample and using large-area wafers (12.5×12.5 cm^2), it was shown for the first time that the bulk lifetime of the examined 1.2-1.4 Ωcm n-type Cz-Si is significantly higher than the current state-of-the-art parameterization of the intrinsic lifetime of c-Si. Therefore, a new parameterization of the intrinsic lifetime for n-type c-Si was performed. Using this new parameterization, all experimental findings were verified by two-dimensional simulations using Sentaurus Device. Importantly, the new parameterization also changes the fundamental efficiency limit, as shown for n-type silicon solar cells with $N_{\mathrm{D}} = 3.5\times10^{15}$ cm^{-3}, from previously reported 28.98% to 29.13%. However, this new parameterization can only be viewed as preliminary. In order to improve the quality of our new parameterization, n-type c-Si wafers with a broader variety of resistivities have to be examined.

The excellent surface passivation of the $\mathrm{Al_2O_3}$ layers was demonstrated using large-area (15.6×15.6 cm^2) PERC solar cells with PA-ALD $\mathrm{Al_2O_3}$ and, for the first time, ICP-AlO_x as rear side passivation layer in combination with a PECVD-SiN_x capping layer. Both $\mathrm{Al_2O_3}$ passivation layers provided comparable efficiencies of 19.8% and 20.1%, respectively, with excellent V_{oc} values of 656 mV in the case of PA-ALD $\mathrm{Al_2O_3}$ and 655 mV for ICP-AlO_x.

For the first time, we demonstrated the applicability of an alternative type of low-cost capping layer replacing the PECVD-SiN_x. These alternative capping layers were all based on liquid siloxane solutions deposited by liquid phase deposition (LPD) at ambient environment using spin-coating. It was shown that $\mathrm{Al_2O_3}$/LPD stacks provide a good surface passivation after firing only if no metal paste is present during the firing step. Thin LPD layers (< 130 nm) were no effective barriers against the Al paste. Only LPD-$\mathrm{SiO}_x\mathrm{TiO}_y$ layers prevented the penetration of aluminum, however, the passivation was poor. As a solution, the use of thick layers and stacks of LPD layers were proposed and it was shown that a stack consisting of a PA-ALD $\mathrm{Al_2O_3}$, a LPD-SiO_x and a LPD-$\mathrm{SiO}_x\mathrm{TiO}_y$ layer provided a good surface passivation even after Al-paste printing and firing. This was additionally demonstrated by large-area (15.6×15.6 cm^2) PERC solar cells with efficiencies up to 19.8%. Nevertheless, this efficiency was slightly lower than the 20.2% of the reference PERC solar cell with SiN_x as capping layer. The inhomogeneity of the LPD capping layer thickness due to the applied spin coating process was identified as the main reason for the slightly reduced efficiencies. This was verified by EQE analysis in the center of the wafer, where for the solar cell with SiN_x capping an S_{rear} of (60±20) cm/s was deduced and for the solar cells with LPD capping the best S_{rear} of (100±20) cm/s was deduced for a solar cell with a 600 nm thick LPD-SiO_x layer capped with a 140 nm thick LPD-$\mathrm{SiO}_x\mathrm{TiO}_y$ layer. Hence, the surface passivation quality provided by $\mathrm{Al_2O_3}$/LPD stacks can be on a par with the surface passivation quality provided by $\mathrm{Al_2O_3}/\mathrm{SiN}_x$ stacks. Therefore, in order to improve the efficiency, two possible measures can be taken: (i) improvement of the smoothness of the rear side (on shiny etched FZ-Si wafers no homogeneity problems were observed) and (ii) the evaluation of other deposition techniques, such as spray-coating, in order to improve the homogeneity of the deposited layers.

Besides the use of $\mathrm{Al_2O_3}$ as rear side passivation on undiffused c-Si surfaces, the use of $\mathrm{Al_2O_3}$ as front side passivation especially on p^+-diffused c-Si surfaces was also evaluated. For the front-side passivation, the stability of the surface passivation under illumination, especially UV, is of utmost importance. For the first time, we demonstrated that fired S-ALD $\mathrm{Al_2O_3}$ layers are very stable under UV illumination, regardless if used as single layer or in Al_2O_3/SiN_x stacks. Especially the Al_2O_3/SiN_x stack showed a stable p^+-emitter passivation with a J_{0E} value of 18 fA/cm^2. For fired single S-ALD Al_2O_3 layers, a strong increase of the negative fixed charge density Q_f, up to a value of $-(11.8\pm1)\times10^{12}$ cm^{-2}, was observed. The surface passivation provided by low-temperature-annealed S-ALD Al_2O_3 layers, however, was found to degrade under UV illumination down to S_{front} values of 122 cm/s on undiffused p-type Cz-Si and J_{0E} values of 95 fA/cm^2 on p^+-diffused silicon surfaces.

It was shown that the reason for the degradation of the thin S-ALD Al_2O_3 layers is a pronounced decrease of the chemical surface passivation. This decrease of the chemical surface passivation is partly compensated by a strong increase in $|Q_f|$ up to a value of $Q_f = -(9.1\pm0.8)\times10^{12}$ cm^{-2}. By applying a higher annealing temperature (550 °C) and using a thicker Al_2O_3 layer (15 nm instead of 5 nm), we achieved an improved stability with only a slight degradation to an S_{front} value of 24 cm/s for samples without any coverage and below 7 cm/s for samples covered under glass and EVA during UV illumination. Further investigations of the UV-induced increase of $|Q_f|$ revealed that already a UV dose of only 1 kWh/m^2 is sufficient for the full $|Q_f|$ increase in the case of annealed Al_2O_3 and for fired Al_2O_3 a slightly higher dose ($\sim$5 kWh/m^2) was shown to be necessary.

The stability of the surface passivation was also examined on samples illuminated using a halogen lamp. These samples showed also an increase in $|Q_f|$ that was correlated with the low fraction of UV photons emitted by the halogen lamp. Besides the increase in $|Q_f|$ it was shown that the fired Al_2O_3 layers are stable, but the low-temperature-annealed Al_2O_3 layers showed a deterioration in surface passivation quality. Hence, for the application in solar cells that receive a firing step, S-ALD Al_2O_3 layers are very well suited for the use as surface passivation layers. However, for the use in solar cells where only low-temperature steps are applied, further effort has to be undertaken to improve the long-term stability of low-temperature-annealed S-ALD Al_2O_3 layers. One promising approach would be to evaluate the use of 15 nm thick S-ALD Al_2O_3 layers in conjunction with a SiN_x capping layer and an annealing step at elevated temperatures (> 500 °C).

References

[1] A. Blakers, A. Wand, A. Milne, J. Zhao, and M. Green, “22.8% efficient silicon solar cell,” *Applied Physics Letters*, vol. 55, no. 13, pp. 1363–1365, 1989.

[2] R. Hezel and K. Jäger, “Low-temperature surface passivation of silicon for solar cells,” *Journal of The Electrochemical Society*, vol. 136, no. 2, pp. 518–523, 1989.

[3] G. Agostinelli, A. Delabie, P. Vitanov, Z. Alexieva, H. Dekkers, S. De Wolf, and G. Beaucarne, “Very low surface recombination velocities on *p*-type silicon wafers passivated with a dielectric with fixed negative charge,” *Solar Energy Materials and Solar Cells*, vol. 90, no. 18-19, pp. 3438–3443, 2006.

[4] B. Hoex, S. B. S. Heil, E. Langereis, M. C. M. van de Sanden, and W. M. M. Kessels, “Ultralow surface recombination of c-Si substrates passivated by plasma-assisted atomic layer deposited Al_2O_3,” *Applied Physics Letters*, vol. 89, no. 4, pp. 042112–1–3, 2006.

[5] J. Schmidt, A. Merkle, R. Brendel, B. Hoex, M. C. M. van de Sanden, and W. M. M. Kessels, “Surface passivation of high-efficiency silicon solar cells by atomic-layer-deposited Al_2O_3,” *Progress in Photovoltaics: Research and Applications*, vol. 16, no. 6, pp. 461–466, 2008.

[6] A. Richter, S. W. Glunz, F. Werner, J. Schmidt, and A. Cuevas, “Improved quantitative description of Auger recombination in crystalline silicon,” *Physical Review B*, vol. 86, no. 16, pp. 165202–1–14, 2012.

[7] B. Hoex, J. Schmidt, P. Pohl, M. C. M. van de Sanden, and W. M. M. Kessels, “Silicon surface passivation by atomic layer deposited Al_2O_3,” *Journal of Applied Physics*, vol. 104, no. 4, pp. 044903–1–12, 2008.

[8] B. Veith, T. Ohrdes, F. Werner, R. Brendel, P. P. Altermatt, N.-P. Harder, and J. Schmidt, “Injection dependence of the effective lifetime of *n*-type Si passivated

by Al_2O_3: An edge effect?," *Solar Energy Materials and Solar Cells*, vol. 120, Part A, pp. 436–440, 2014.

[9] P. Poodt, A. Lankhorst, F. Roozeboom, K. Spee, D. Maas, and A. Vermeer, "High-speed spatial atomic-layer deposition of aluminum oxide layers for solar cell passivation," *Advanced Materials*, vol. 22, no. 32, pp. 3564–3567, 2010.

[10] I. Cesar, E. Granneman, P. Vermont, E. Tois, P. Manshanden, L. Geerligs, E. E. Bende, A. Burgers, A. Mewe, Y. Komatsu, and A. Weeber, "Excellent rear side passivation on multi-crystalline silicon solar cells with 20 nm uncapped Al_2O_3 layer: Industrialization of ALD for solar cell applications," in *Proceedings of the 35th IEEE Photovoltaic Specialists Conference*, pp. 44–49, 2010.

[11] P. Saint-Cast, D. Kania, M. Hofmann, J. Benick, J. Rentsch, and R. Preu, "Very low surface recombination velocity on p-type c-Si by high-rate plasma-deposited aluminum oxide," *Applied Physics Letters*, vol. 95, no. 15, pp. 151502–1–3, 2009.

[12] L. E. Black, K. M. Provancha, and K. R. McIntosh, "Surface passivation of crystalline silicon by APCVD aluminium oxide," in *Proceedings of the 26th EU Photovoltaic Solar Energy Conference*, pp. 1120–1124, 2011.

[13] P. P. Altermatt, T. Trupke, and A. Neisser, "Injection dependence of spontaneous radiative recombination in c-Si: experiment, theoretical analysis, and simulation," in *Proceedings of the 5th International Conference on Numerical Simulation of Optoelectronic Devices*, pp. 47–48, 2005.

[14] P. P. Altermatt, A. Schenk, F. Geelhaar, and G. Heiser, "Reassessment of the intrinsic carrier density in crystalline silicon in view of band-gap narrowing," *Journal of Applied Physics*, vol. 93, no. 3, p. 1598, 2003.

[15] T. Trupke, M. A. Green, P. Würfel, P. P. Altermatt, A. Wang, J. Zhao, and R. Corkish, "Temperature dependence of the radiative recombination coefficient of intrinsic crystalline silicon," *Journal of Applied Physics*, vol. 94, no. 8, pp. 4930–4937, 2003.

[16] K. Misiakos and D. Tsamakis, "Accurate measurements of the silicon intrinsic carrier density from 78 to 340 k," *Journal of Applied Physics*, vol. 74, no. 5, pp. 3293–3297, 1993.

[17] A. Schenk, “Finite-temperature full random-phase approximation model of band gap narrowing for silicon device simulation,” *Journal of Applied Physics*, vol. 84, no. 7, pp. 3684–3695, 1998.

[18] J. Dziewior and W. Schmid, “Auger coefficients for highly doped and highly excited silicon,” *Applied Physics Letters*, vol. 31, no. 5, pp. 346–348, 1977.

[19] R. A. Sinton and R. M. Swanson, “Recombination in highly injected silicon,” *IEEE Transactions on Electron Devices*, vol. 34, no. 6, pp. 1380–1389, 1987.

[20] A. Hangleiter and R. Häcker, “Enhancement of band-to-band auger recombination by electron-hole correlations,” *Physical Review Letters*, vol. 65, no. 2, pp. 215–218, 1990.

[21] D. B. Laks, G. F. Neumark, and S. T. Pantelides, “Accurate interband-Auger-recombination rates in silicon,” *Physical Review B*, vol. 42, no. 8, pp. 5176–5185, 1990.

[22] M. Govoni, I. Marri, and S. Ossicini, “Auger recombination in Si and GaAs semiconductors: Ab initio results,” *Physical Review B*, vol. 84, no. 7, pp. 075215–1–11, 2011.

[23] P. T. Landsberg, “Trap-Auger recombination in silicon of low carrier densities,” *Applied Physics Letters*, vol. 50, no. 12, pp. 745–747, 1987.

[24] M. J. Kerr and A. Cuevas, “General parameterization of Auger recombination in crystalline silicon,” *Journal of Applied Physics*, vol. 91, no. 4, pp. 2473–2480, 2002.

[25] W. Shockley and W. Read, “Statistics of the recombinations of holes and electrons,” *Physical Review Letters*, vol. 87, no. 5, pp. 835–842, 1952.

[26] R. Hall, “Electron-hole recombination in germanium,” *Physical Review*, vol. 87, no. 2, p. 387, 1952.

[27] J. Schmidt, *Untersuchung zur Ladungsträgerrekombination an der Oberfläche und im Volumen von kristallinen Silicium-Solarzellen.* PhD thesis, Universität Hannover, 1998.

[28] S. Dauwe, *Low-Temperature Surface Passivation os Crystalline Silicon and its Application to the Rear Side of Solar Cells.* PhD thesis, Universität Hannover, 2004.

[29] R. Girisch, R. Mertens, and R. de Keersmaecker, “Determination of Si-SiO$_2$ interface recombination parameters using a gate-controlled pointjunction diode under illumination,” *IEEE Transactions on Electron Devices*, vol. 35, no. 2, pp. 203–222, 1988.

[30] A. S. Grove and D. J. Fitzgerald, “Surface effects on $p-n$ junctions: Characteristics of surface space-charge regions under non-equilibrium conditions,” *Solid-State Electronics*, vol. 9, no. 8, pp. 783–806, 1966.

[31] F. Werner, B. Veith, D. Zielke, L. Kühnemund, C. Tegenkamp, M. Seibt, R. Brendel, and J. Schmidt, “Electronic and chemical properties of the c-Si/Al$_2$O$_3$ interface,” *Journal of Applied Physics*, vol. 109, no. 11, pp. 113701–1–6, 2011.

[32] F. Werner, *Atomic layer deposition of aluminum oxide on crystalline silicon: Fundamental interface properties and application to solar cells.* PhD thesis, Leibniz Universität Hannover, 2014.

[33] J. J. H. Gielis, B. Hoex, M. C. M. van de Sanden, and W. M. M. Kessels, “Negative charge and charging dynamics in Al$_2$O$_3$ films on Si characterized by second-harmonic generation,” *Journal of Applied Physics*, vol. 104, no. 7, pp. 073701–1–5, 2008.

[34] B. Hoex, J. J. H. Gielis, M. C. M. van de Sanden, and W. M. M. Kessels, “On the c-Si surface passivation mechanism by the negative-charge-dielectric Al$_2$O$_3$,” *Journal of Applied Physics*, vol. 104, no. 11, pp. 113703–1–7, 2008.

[35] S. Steingrube, *Recombination Models for Defects in Silicon Solar Cells*. PhD thesis, Universität Hannover, 2011.

[36] F.-J. Ma, G. G. Samudra, M. Peters, A. G. Aberle, F. Werner, J. Schmidt, and B. Hoex, “Advanced modeling of the effective minority carrier lifetime of passivated crystalline silicon wafers,” *Journal of Applied Physics*, vol. 112, no. 5, pp. 054508–1–8, 2012.

[37] M. Kessler, T. Ohrdes, P. P. Altermatt, and R. Brendel, “The effect of sample edge recombination on the averaged injection-dependent carrier lifetime in silicon,” *Journal of Applied Physics*, vol. 111, no. 5, pp. 054508–1–12, 2012.

[38] *Sentaurus Device User Guide, Version C-2009.06*. Synopsys, Inc., Mountain View, CA.

[39] L. E. Black, *New Perspectives on Surface Passivation: Understanding the Si-Al_2O_3 Interface.* PhD thesis, Australian National University, 2015.

[40] A. B. Sproul, "Dimensionless solution of the equation describing the effect of surface recombination on carrier decay in semiconductors," *Journal of Applied Physics*, vol. 76, no. 5, pp. 2851–2854, 1994.

[41] M. J. Stocks, *High efficiency multicrystalline silicon solar cells.* PhD thesis, Australian National University, 1998.

[42] F. Werner, A. Cosceev, and J. Schmidt, "Interface recombination parameters of atomic-layer-deposited Al_2O_3 on crystalline silicon," *Journal of Applied Physics*, vol. 111, no. 7, pp. 073710–1–6, 2012.

[43] L. E. Black and K. R. McIntosh, "Surface passivation of c-Si by atmospheric pressure chemical vapor deposition of Al_2O_3," *Applied Physics Letters*, vol. 100, no. 20, pp. 202107–1–5, 2012.

[44] T.-T. A. Li and A. Cuevas, "Effective surface passivation of crystalline silicon by rf sputtered aluminum oxide," *physica status solidi - Rapid Research Letters*, vol. 3, no. 5, pp. 160–162, 2009.

[45] S. George, A. Ott, and J. Klaus, "Surface chemistry for atomic layer growth," *The Journal of Physical Chemistry*, vol. 100, no. 31, pp. 13121–13131, 1996.

[46] W. Kern, "The evolution of silicon wafer cleaning technology," *Journal of The Electrochemical Society*, vol. 137, no. 6, pp. 1887–1892, 1990.

[47] D. K. Schroder, *Semiconductor material and device characterization.* John Wiley & Sons Inc., Hoboken, New Jersey, 2006.

[48] D. Klaassen, "A unified mobility model for device simulation – I. model equations and concentration dependence," *Solid-State Electronics*, vol. 35, no. 7, pp. 953 – 959, 1992.

[49] E. Yablonovitch and T. Gmitter, "Auger recombination in silicon at low carrier densities," *Applied Physics Letters*, vol. 49, no. 10, pp. 587–589, 1986.

[50] H. Nagel, C. Berge, and A. G. Aberle, "Generalized analysis of quasi-steady-state and quasi-transient measurements of carrier lifetimes in semiconductors," *Journal of Applied Physics*, vol. 86, no. 11, pp. 6218–6221, 1999.

[51] R. A. Sinton and A. Cuevas, “Contactless determination of current–voltage characteristics and minority-carrier lifetimes in semiconductors from quasi-steady-state photoconductance data,” *Applied Physics Letters*, vol. 69, no. 17, pp. 2510–2512, 1996.

[52] S. Herlufsen, J. Schmidt, D. Hinken, K. Bothe, and R. Brendel, “Photoconductance-calibrated photoluminescence lifetime imaging of crystalline silicon,” *physica status solidi - Rapid Research Letters*, vol. 2, no. 6, pp. 245–247, 2008.

[53] P. J. Cousins, D. H. Neuhaus, and J. E. Cotter, “Experimental verification of the effect of depletion-region modulation on photoconductance lifetime measurements,” *Journal of Applied Physics*, vol. 95, no. 4, pp. 1854–1858, 2004.

[54] D. Macdonald and A. Cuevas, “Trapping of minority carriers in multicrystalline silicon,” *Applied Physics Letters*, vol. 74, no. 12, pp. 1710–1712, 1999.

[55] K. Ramspeck, S. Reissenweber, J. Schmidt, K. Bothe, and R. Brendel, “Dynamic carrier lifetime imaging of silicon wafers using an infraredcamera-based approach,” *Applied Physics Letters*, vol. 93, no. 10, pp. 102104–1–3, 2008.

[56] S. Dauwe, J. Schmidt, A. Metz, and R. Hezel, “Fixed charge density in silicon nitride films on crystalline silicon surfaces under illumination,” in *Proceedings of the 29th IEEE Photovoltaic Specialists Conference*, pp. 162–165, 2002.

[57] L. Kelvin, “Contact electricity of metals,” *Philosophical Magazine*, vol. 46, pp. 82–120, 1898.

[58] E. H. Nicollian and J. R. Brews, *MOS (Metal Oxide Semiconductor) Physics and Technology.* New York: John Wiley & Sons, 1982.

[59] T. Lüder, B. Raabe, and B. Terheiden, “Annaeling behavior of Al_2O_3 thin films grown on crystalline silicon by atomic layer deposition,” in *Proceedings of the 25th EU Photovoltaic Solar Energy Conference*, pp. 2138 – 2140, 2010.

[60] X. Gay, F. Souren, B. Dielissen, M. Bijker, R. Gortzen, D. Pysch, K. Weise, B. Sander, and R. Sastrawan, “Post-deposition thermal treatment of ultrafast spatial ALD Al_2O_3 for the rear side passivation of p-type PERC solar cells,” in *Proceedings of the 28th EU Photovoltaic Solar Energy Conference*, pp. 1220–1224, 2013.

[61] P. Altermatt, “Models for numerical device simulations of crystalline silicon solar cells - a review,” *Journal of Computational Electronics*, vol. 10, pp. 314–330, 2011.

[62] T. Ohrdes, *Charakterisierungsmethoden und simulationsgestützte Analysen von Silizium Solarzellen.* PhD thesis, Universität Hannover, 2014.

[63] Y. Wan, K. R. McIntosh, A. F. Thomson, and A. Cuevas, “Low surface recombination velocity by low-absorption silicon nitride on c-si,” in *Proceedings of the 38th IEEE Photovoltaic Specialists Conference Part 2*, pp. 1–7, June 2012.

[64] T. Niewelt, W. Kwapil, M. Selinger, A. Richter, and M. C. Schubert, “Long-term stability of aluminum oxide based surface passivation schemes under illumination at elevated temperatures,” *IEEE Journal of Photovoltaics*, vol. 7, no. 5, pp. 1197–1202, 2017.

[65] R. Häcker and A. Hangleiter, “Intrinsic upper limits of the carrier lifetime in silicon,” *Journal of Applied Physics*, vol. 75, no. 11, pp. 7570–7572, 1994.

[66] J. del Alamo, S. Swirhun, and R. M. Swanson, “Simultaneous measurement of hole lifetime, hole mobility and bandgap narrowing in heavily doped n-type silicon,” in *Proceedings of the International Electron Devices Meeting*, vol. 31, pp. 290–293, 1985.

[67] A. Richter, M. Hermle, and S. W. Glunz, “Reassessment of the limiting efficiency for crystalline silicon solar cells,” *IEEE Journal of Photovoltaics*, vol. 3, no. 4, pp. 1184–1191, 2013.

[68] M. A. Green, “Limits on the open-circuit voltage and efficiency of silicon solar cells imposed by intrinsic auger processes,” *IEEE Transactions on Electron Devices*, vol. 31, no. 5, pp. 671–678, 1984.

[69] T. Dullweber, S. Gatz, H. Hannebauer, T. Falcon, R. Hesse, J. Schmidt, and R. Brendel, “Towards 20silicon solar cells,” *Progress in Photovoltaics: Research and Applications*, vol. 20, no. 6, pp. 630–638, 2012.

[70] S. Gatz, H. Hannebauer, R. Hesse, F. Werner, A. Schmidt, T. Dullweber, J. Schmidt, K. Bothe, and R. Brendel, “19.4screen-printed silicon solar cells,” *physica status solidi - Rapid Research Letters*, vol. 5, no. 4, pp. 147–149, 2011.

[71] J. Bullock, A. Thomson, A. Cuevas, B. Veith, J. Schmidt, and A. Karkkainen, "Enhanced rear-side reflection and firing-stable surface passivation of silicon solar cells with capping polymer films," *physica status solidi - Rapid Research Letters*, vol. 7, no. 8, pp. 530–533, 2013.

[72] R. Brendel, M. Hirsch, R. Plieninger, and J. H. Werner, "Quantum efficiency analysis of thin-layer silicon solar cells with back surface fields and optical confinement," *IEEE Transactions on Electron Devices*, vol. 43, no. 7, pp. 1104–1113, 1996.

[73] T. Lauinger, J. Moschner, A. G. Aberle, and R. Hezel, "Optimization and characterization of remote plasma-enhanced chemical vapor deposition silicon nitride for the passivation of p-type crystalline silicon surfaces," *Journal of Vacuum Science and Technology A: Vacuum, Surfaces, and Films*, vol. 16, no. 2, pp. 530–543, 1998.

[74] C. Schmid, J. Chapon, G. Kinsey, J. Bokria, and J. Woods, "Impact of high light transmission EVA-based encapsulant on the performance of PV modules," in *Proceedings of the 27th EU Photovoltaic Solar Energy Conference*, pp. 3494–3498, 2012.

[75] M. R. Vogt, H. Holst, H. Schulte-Huxel, S. Blankemeyer, R. Witteck, D. Hinken, M. Winter, B. Min, C. Schinke, I. Ahrens, M. Köntges, K. Bothe, and R. Brendel, "Optical constants of UV transparent EVA and the impact on the PV module output power under realistic irradiation," *Energy Procedia*, vol. 92, pp. 523–530, 2016.

[76] J. Schmidt, A. Merkle, R. Bock, P. P. Altermatt, A. Cuevas, N. P. Harder, B. Hoex, M. C. M. van de Sanden, W. M. M. Kessels, and R. Brendel, "Progress in the surface passivation of silicon solar cells," in *Proceedings of the 23rd EU Photovoltaic Solar Energy Conference*, pp. 974–981, 2008.

[77] G. Dingemans, P. Engelhart, R. Seguin, F. Einsele, B. Hoex, M. C. M. van de Sanden, and W. M. M. Kessels, "Stability of Al_2O_3 and Al_2O_3/a-SiN_x:H stacks for surface passivation of crystalline silicon," *Journal of Applied Physics*, vol. 106, no. 11, pp. 114907–1–4, 2009.

[78] J. Schmidt, A. G. Aberle, and R. Hezel, "Investigation of carrier lifetime instabilities in Cz-grown silicon," in *Proceedings of the 26th IEEE Photovoltaic Specialists Conference*, pp. 13–18, 1997.

[79] H. Holst, M. Winter, M. R. Vogt, K. Bothe, M. Köntges, R. Brendel, and P. P. Altermatt, “Application of a new ray tracing framework to the analysis of extended regions in Si solar cell modules,” *Energy Procedia*, vol. 38, pp. 86–93, 2013.

[80] M. R. Vogt, H. Hahn, H. Holst, M. Winter, C. Schinke, M. Köntges, R. Brendel, and P. P. Altermatt, “Measurement of the optical constants of soda-lime glasses in dependence of iron content, and modeling of iron-related power losses in crystalline Si solar cell modules,” *IEEE Journal of Photovoltaics*, vol. 6, no. 1, pp. 111–118, 2016.

[81] D. Kane and R. Swanson, “Measurement of the emitter saturation current by a contactless photoconductivity decay method,” in *Proceedings of the 18th IEEE Photovoltaic Specialists Conference*, pp. 578–583, 1985.

[82] A. L. Blum, J. S. Swirhun, R. A. Sinton, and A. Kimmerle, “An updated analysis to the WCT-120 QSSPC measurement system using advanced device physics,” in *Proceedings of the 28th EU Photovoltaic Solar Energy Conference*, pp. 1521–1523, 2013.

[83] B. Liao, R. Stangl, T. Mueller, F. Lin, C. S. Bhatia, and B. Hoex, “The effect of light soaking on crystalline silicon surface passivation by atomic layer deposited Al_2O_3,” *Journal of Applied Physics*, vol. 113, no. 2, pp. 024509–1–6, 2013.

[84] B. Kuhlman, *Charakterisierung und mehrdimensionale Simulation von MIS-Inversionschichtsolarzellen.* PhD thesis, University of Hannover, 1998.

Publications

Parts of this thesis have previously been published in several of the following publications:

Publications in refereed journals:

- B. Veith, T. Ohrdes, F. Werner, R. Brendel, P.P. Altermatt, N.-P. Harder, and J. Schmidt, "Injection dependence of the effective lifetime of n-type Si passivated by Al_2O_3: an edge effect?" *Solar Energy Materials and Solar Cells*, vol. 120, pp. 436–440, 2014.

  SiliconPV Award 2013

- B. Veith-Wolf, J. Wang, M. Hannu-Kuure, N. Chen, A. Hadzic, P. Williams, J. Leivo, A. Karkkainen, and J. Schmidt, "Liquid-phase-deposited siloxane-based capping layers for silicon solar cells," *Applied Physics Letters*, vol. 106, pp. 52104-1–4, 2015.

- B. Veith-Wolf, and J. Schmidt, "Unexpectedly high minority-carrier lifetimes exceeding 20 ms measured on 1.4-Ωcm n-type silicon wafers," *Physica Status Solidi RRL*, vol. 11, pp. 1700235-1–3, 2017.

- B. Veith-Wolf, R. Witteck, A. Morlier, H. Schulte-Huxel, M. R. Vogt, and J. Schmidt, "Spectra-dependent stability of the passivation quality of Al_2O_3/c-Si interfaces," *IEEE Journal of Photovoltaics*, vol. 8, pp. 96–102, 2018.

- J. Schmidt, B. Veith, and R. Brendel, "Effective surface passivation of crystalline silicon using ultrathin Al_2O_3 films and Al_2O_3/SiN_x stacks," *Physica Status Solidi RRL*, vol. 3, pp. 287–289, 2009.

- F. Werner, B. Veith, V. Tiba, P. Poodt, F. Roozeboom, R. Brendel, and J. Schmidt, "Very low surface recombination velocities on p- and n-type c-Si by ultrafast spatial atomic layer deposition of aluminum oxide," *Applied Physics Letters*, vol. 97, pp. 162103-1–3, 2010.

- F. Werner, B. Veith, D. Zielke, L. Kühnemund, C. Tegenkamp, M. Seibt, R. Brendel, and J. Schmidt, "Electronic and chemical properties of the c-Si/Al_2O_3 interface," *Journal of Applied Physics*, vol. 109, pp. 113701-1–6, 2011.

- D. Zielke, J.H. Petermann, F. Werner, B. Veith, R. Brendel, and J. Schmidt, "Contact passivation in silicon solar cells using atomic-layer-deposited aluminum oxide layers," *Physica Status Solidi RRL*, vol. 5, pp. 298–300, 2011.

- T. Dullweber, C. Kranz, B. Beier, B. Veith, J. Schmidt, B.F.P. Roos, O. Hohn, T. Dippell, and R. Brendel, "Inductively coupled plasma chemical vapour deposited AlO_x/SiN_y layer stacks for applications in high-efficiency industrial-type silicon solar cells," *Solar Energy Materials and Solar Cells*, vol. 112, pp. 196–201, 2013.

- J. Bullock, A. Thomson, A. Cuevas, B. Veith, J. Schmidt, and A. Karkkainen, "Enhanced rear-side reflection and firing-stable surface passivation of silicon solar cells with capping polymer films," *Physica Status Solidi RRL*, vol. 7, pp. 530–533, 2013.

- L.E. Black, T. Allen, A. Cuevas, K.R. McIntosh, B. Veith, and J. Schmidt, "Thermal stability of silicon surface passivation by APCVD Al_2O_3," *Solar Energy Materials and Solar Cells*, vol. 120, pp. 339–345, 2014.

  SiliconPV Award 2013

- R. Witteck, B. Veith-Wolf, H. Schulte-Huxel, A. Morlier, M. R. Vogt, M. Köntges, and R. Brendel, "UV-induced degradation of PERC solar modules with UV-transparent encapsulation materials," *Progress in Photovoltaics: Research and Applications*, vol. 25, pp. 409–416, 2017.

- R. Witteck, B. Min, H. Schulte-Huxel, H. Holst, B. Veith-Wolf, F. Kiefer, M. R. Vogt, M. Köntges, R. Peibst, and R. Brendel, "UV radiation hardness of photovoltaic modules featuring crystalline Si solar cells with AlO_x/p^+-type Si and SiN_y/n^+-type Si interfaces," *Physica Status Solidi RRL*, vol. 11, pp. 1700178-1–

6, 2017.

Publications in conference proceedings

- B. Veith, F. Werner, D. Zielke, R. Brendel, and J. Schmidt, "Comparison of the thermal stability of single Al_2O_3 layers and Al_2O_3/SiN_x stacks for the surface passiviation of silicon". in *Energy Procedia*, vol. 8, pp. 307–312, 2011.
- B. Veith, T. Dullweber, M. Siebert, C. Kranz, F. Werner, N.-P. Harder, J. Schmidt, B.F.P. Roos, T. Dippell, and R. Brendel, "Comparison of ICP-AlO_x and ALD-Al_2O_3 layers for the rear surface passivation of c-Si Solar cells," in *Energy Procedia*, vol. 27, pp. 379–384, 2012.
- B. Veith-Wolf, J. Wang, M. Hannu-Kuure, N. Chen, A. Hadzic, P. Williams, J. Leivo, A. Karkkainen, and J. Schmidt, "Siloxane-based capping layers for Al_2O_3 as silicon nitride replacement in industrial-type PERC solar cells," in *Proceedings of the 29th European Photovoltaic Solar Energy Conference*, pp. 600–602, 2014.
- B. Veith-Wolf, R. Witteck, A. Morlier, H. Schulte-Huxel, and J. Schmidt, "Effect of UV Illumination on the passivation quality of AlO_x/c-Si interfaces," in *Proceedings of the 43rd IEEE Photovoltaic Specialist Conference*, pp. 1173–1178, 2016.

- P.P. Altermatt, S. Steingrube, Y. Yang, C. Sprodowski, T. Dezhdar, S. Koc, B. Veith, S. Hermann, R. Bock, K. Bothe, J. Schmidt, and R. Brendel, "Highly predictive modelling of entire Si solar cells for industrial applications," in *Proceedings of the 24th European Photovoltaic Solar Energy Conference*, pp. 901–906, 2009.
- F. Werner, B. Veith, D. Zielke, L. Kühnemund, C. Tegenkamp, M. Seibt, J. Schmidt, and R. Brendel, "Improved understanding of recombination at the Si/Al_2O_3 interface," in *Proceedings of the 25th European Photovoltaic Solar Energy Conference*, pp. 1121–1124, 2010.
- J. Schmidt, F. Werner, B. Veith, D. Zielke, R. Bock, V. Tiba, P. Poodt, F. Roozeboom, A. Li, A. Cuevas, and R. Brendel, "Industrially relevant Al_2O_3 deposition techniques for the surface passivation of Si solar cells," in *Proceedings of the 25th European Photovoltaic Solar Energy Conference*, pp. 1130–1133, 2010.

- J. Schmidt, B. Veith, F. Werner, D. Zielke, and R. Brendel, "Silicon surface passivation by ultrathin Al_2O_3 films and Al_2O_3/SiN_x stacks," in *Proceedings of the 35th IEEE Photovoltaic Specialist Conference*, pp. 885–890, 2010.
- F. Werner, W. Stals, R. Görtzen, B. Veith, R. Brendel, and J. Schmidt, "High-rate atomic layer deposition of Al_2O_3 for the surface passivation of Si solar cells," in *Energy Procedia*, vol. 8, pp. 301–306, 2011.
- D. Zielke, J.H. Petermann, F. Werner, B. Veith, R. Brendel, and J. Schmidt, "21.7% efficient PERC solar cells with AlO_x tunneling layer," in *Proceedings of the 26th European Photovoltaic Solar Energy Conference*, pp. 1115–1119, 2011.
- J. Schmidt, F. Werner, B. Veith, D. Zielke, S. Steingrube, P.P. Altermatt, S. Gatz, T. Dullweber, and R. Brendel, "Advances in the surface passivation of silicon solar cells," in *Energy Procedia*, vol. 15, pp. 30–39, 2012.
- T. Dullweber, M. Siebert, B. Veith, C. Kranz, J. Schmidt, R. Brendel, B.F.P. Roos, T. Dippell, A. Schwabedissen, and S. Peters, "High-efficiency industrial-type PERC solar cells applying ICP AlO_x as rear passivation layer," in *Proceedings of the 27th European Photovoltaic Solar Energy Conference*, pp. 672–675, 2012.
- B.F.P. Roos, T. Dippell, O. Hohn, P. Wohlfart, B. Beier, B. Veith, M. Siebert, and T. Dullweber, "ICP-PECVD production tool for industrial AlO_x and Si-based passivation layers," in *Proceedings of the 27th European Photovoltaic Solar Energy Conference*, pp. 1684–1687, 2012.

Other Publications

- J. Schmidt, F. Werner, B. Veith, D. Zielke, R. Bock, R. Brendel, V. Tiba, P. Poodt, F. Roozeboom, A. Li, and A. Cuevas, "Surface passivation of silicon solar cells using industrially relevant Al_2O_3 deposition techniques," *Photovoltaics International*, vol. 10, 2010.
- F. Werner, B. Veith, and J. Schmidt, "Homogeneous surface: Recombination at the c-Si/Al_2O_3 interface," *Photovoltaic Production*, vol. 4, 2011.
- S. Gatz, J. Schmidt, B. Veith, T. Dullweber, and R. Brendel, "Firing stability of SiN_y/SiN_x and Al_2O_3/SiN_x stacks for the rearsurface passivation of industrial-type crystalline silicon solar cells," *PV International*, vol. 15, 2012.

- T. Dullweber, C. Kranz, B. Beier, B. Veith, J. Schmidt, B.F.P. Roos, and T. Dippell, "20.1%-efficient industrial type PERC solar cells applying ICP AlO_x as rear passivation layer, " *PV International*, vol. 17, 2012.

Danksagung

Zum Schluss möchte ich mich bei all denen bedanken, die mich immer wieder während meiner Doktorarbeit unterstützt haben. Besonders möchte ich mich bei meinen Kolleginnen und Kollegen am ISFH für die ständige Unterstützung und die tolle Arbeitsatmosphäre bedanken. Den folgenden Personen gilt darüber hinaus mein besonderer Dank:

Prof. Jan Schmidt für das Vertrauen, das er in mich gesetzt hat. Ich möchte mich auch für seine Unterstützung und seinen Rat bedanken. Besonderer Dank gilt ihm auch dafür, dass er mir die Freiheiten in der Forschung gewährt hat.

Prof. Christoph Tegenkamp für die bereitwillige Übernahme des Korreferates.

Prof. Holger Frahm für die Übernahmme des Prüfungskommissionsvorsitz.

Florian für seine Anleitung hin zum wissenschaftlichen Arbeiten, für seine klugen Kommentare und Hinweise sowie all die gute Zeit im "ALD-Team". Danke auch für die Kommentare zu meiner Doktorarbeit.

Dimitri für all die Zeit, die er mein Schreibtischnachbar war und mir immer wieder die Zunahme der Entropie anhand der Diffusion seiner Unterlagen auf meinen Schreibtisch erklärt hat. Für das Näherbringen der "russischen" Kultur, insbesondere des riesigen Fundus an "russischen" Sprichwörtern, sowie die vielen spannenden Diskussionen fachlicher und auch gesellschaftlicher Themen und für das unermüdliche Korrekturlesen.

All meinen Bürokollegen und -kolleginnen, **Dimitri, Alexandra, Jörg, Arne, Jonas, Tim, Michael, Sören, Valeriya, Lasse** für die schöne Atmosphäre und den Spaß, den wir zusammen hatten.

Henning dafür, dass er immer da ist, wenn man ihn braucht, er mir beständig Tipps und Tricks im "Wissenschaftsbetrieb" gegeben hat, für die hilfreichen Kommentare zu meiner Doktorarbeit und für die vielen schönen Zeiten auch außerhalb der Arbeit.

Robert für die gute Zusammenarbeit zum Thema UV Degradation.

Nils für die zahlreichen Diskussionen über C–V und Q–V Messungen sowie die wertvollen Kommentare zu meiner Doktorarbeit.

Michael Siebert ohne dessen Vorarbeit ich niemals so gute Ergebnisse mit dem ICP-AlO_x erzielt hätte.
Michael Kessler für das Anstoßen der Arbeit zum Randeffekt der Al_2O_3 Passivierung auf *n*-Typ Silizium.
Tobias für die gute Zusammenarbeit bei der Erforschung des Randeffektes der Al_2O_3 Passivierung auf *n*-Typ Silizium sowie insbesondere für die Erstellung der Simulationen und der GUI, die es mir ermöglicht hat noch weiter den Randeffekt zu untersuchen.
Sören für die Bereitstellung seiner Matlab Dateien, ohne die ich den maximalen Wirkungsgrad nicht so schnell berechnet hätte.
Conny für die zahlreichen Reinigungen meiner Silizium-Proben sowie die Unterstützung in der Nasschemie.
Thorsten Dullweber sowie seiner Arbeitsgruppe, insbesondere **Ulrike Baumann**, für die Unterstützung bei der Herstellung der PERC Solarzellen.
All the collegues at **ANU** I worked with or met for the collaboration and for showing me that my work does has an impact.
Pepijn Sutmuller from SoLayTec for always supporting me in case of problems with the S-ALD.
Roland Fleischer von Oxford Instruments, der mir immer telefonisch geholfen hat, wenn an der FlexAL etwas nicht funktioniert hat.
Meinen Eltern **Kurt** und **Erika** dafür, dass sie mich immer unterstützt haben.
Meinen Geschwistern **Sonja** und **Gregor**, die immer für mich da sind und insbesondere bei **Sonja** für das Korrekturlesen der finalen Fassung.
Der größte Dank gilt aber meiner tollen Frau **Katharina**, die mich immer unterstützt hat, die mir geholfen hat meinen Weg zu gehen und insbesondere die schwere Zeit nach dem viel zu frühen Tod unserer Tochter **Svenja Marie** zu überstehen. Meiner Tochter **Svenja Marie**, die ich leider nie lebend kennenlernen durfte, die mich aber dazu gebracht hat die Promotion voran zu treiben, du bist immer in meinem Herzen. Meinem Sohn **Jonas Finn**, der wieder den Sonnenschein zurück in unser Leben gebracht hat und mich darin lehrt Geduld zu haben und die Dinge nicht immer so ernst zu nehmen. Meiner Tochter **Carlotta Mia**, die mir die Kraft und den Ansporn gegeben hat die letzten Meter zum Ende der Promotion zu gehen.

Curriculum Vitae

Personal details

Name: Boris Adrian Veith-Wolf (née Veith)
Date of Birth: 08.12.1983
Place of birth: Hannover, Germany
Family status: married to Katharina Wolf, son Jonas Finn Wolf and daughter Carlotta Mia Wolf

Academic education

10.2004 – 02.2010	Leibniz Universität Hannover, Hannover, Germany Diploma studies in physics Degree: Diplom Physik

Working Experience

since 01.2010	Research fellow at Institute for Solar Energy Research Hamelin (ISFH), Emmerthal, Germany
10.2007 – 12.2009	BAföG- und Sozialberatung des AStAs der Leibniz Universität Hannover, Hannover, Germany

School education and civilian service

09.2003 – 06.2004	Civilian service as ambulance man, Deutsches Rotes Kreuz, Laatzen, Germany
08.2001 – 06.2003	IGS Roderbruch, Hannover, Germany Degree: Abitur (Allgemeine Hochschulreife)
09.2000 – 06.2001	Nevada High School, Nevada, MO, USA Degree: High School Diploma
08.1990 – 06.2000	IGS Roderbruch, Hannover, Germany